PHYSICS OF TEXTURED SURFACES WITH SELECTIVE WETTABILITY AND PHOTOCATALYTIC ACTIVITY FOR MULTIFUNCTIONAL APPLICATIONS

BY

TALAL FARHAN AHMED QAHTAN

A Dissertation Presented to the
DEANSHIP OF GRADUATE STUDIES

KING FAHD UNIVERSITY OF PETROLEUM & MINERALS
DHAHRAN, SAUDI ARABIA

In Partial Fulfillment of the
Requirements for the Degree of

DOCTOR OF PHILOSOPHY

In

PHYSICS

December, 2017

KING FAHD UNIVERSITY OF PETROLEUM & MINERALS

DHAHRAN- 31261, SAUDI ARABIA

DEANSHIP OF GRADUATE STUDIES

This thesis, written by **TALAL FARHAN AHMED QAHTAN** under the direction of his thesis advisor and approved by his thesis committee, has been presented and accepted by the Dean of Graduate Studies, in partial fulfillment of the requirements for the degree of **DOCTOR OF PHILOSOPHY IN PHYSICS.**

Dr. Abdullah A. Al-Sunaidi
Department Chairman

Dr. Salam A. Zummo
Dean of Graduate Studies

28/1/18
Date

M. a. Gondal
Dr. Mohammad A. Gondal
(Advisor)

Dr. Syed M. Zubair
(Member)

Shawabkeh
16/1/18
Dr. Reyad A. Shawabkeh
(Member)

Dr. Zain H. Yamani
(Member)

Dr. Saleem Rao
(Member)

Dedication

To my mother and deceased father who inspire me to think, dream and plan for a bright future

To my beloved wife and my lovely sons who are the secrets of my happiness

ACKNOWLEDGMENTS

First of all, I would like to express my deep thanks to my advisor, Prof. Mohammad A. Gondal for his attention, patience, constructive suggestions and continuous support. He taught me how I should solve a research problem and encouraged me to be an independent researcher.

I am also pleased to express my deep thanks for my thesis committee members: Prof. Syed M. Zubair, Prof. Reyad A. Shawabkeh, Dr. Zain H. Yamani and Dr. Saleem Rao for their attention and constructive feedback.

I would like to thank Prof. Gareth McKinley and Prof. Kripa Varanasi who invited me to work in their labs and collaborate with their research groups at MIT in summer 2014, 2016 and 2017 under KFUPM-MIT collaboration program. In particular, I would like to thank Dr. Gibum Kwon, Divya Panchanathan, and Leonardo David Banchik for their valuable feedback throughout the process. Dr. Gibum Kwon and Divya Panchanathan helped to overcome obstacles in experiments. Leonardo David Banchik contributed on the third section of this work by collaborating on the novel feed-side membrane coating and performing modeling.

I would like to acknowledge Center of Excellence in Nanotechnology at KFUPM for supporting and providing the facilities to carry out this work.

I would like to extend my thanks to the Physics Department at KFUPM, and the chairman Dr. Abdullah A. Al-Sunaidi in particular for his assistance and continuous support to complete this work successfully.

TABLE OF CONTENTS

ACKNOWLEDGMENTS V

TABLE OF CONTENTS VI

LIST OF TABLES VIII

LIST OF FIGURES IX

LIST OF ABBREVIATIONS XV

ABSTRACT XVII

ملخص الرسالة XIX

1 CHAPTER INTRODUCTION 1

1.1 Objectives 2

1.2 Wettability 3

1.2.1 Wettability of Ideal Solid Surfaces 3

1.2.2 Wettability of Textured Solid Surfaces 5

1.2.3 Membrane-based Oil-water Separation 9

1.3 Photocatalytic Semiconductors 10

2 CHAPTER LITERATURE REVIEW 14

2.1 Oil-passing Multifunctional Membranes 14

2.2 Water-passing Multifunctional Membranes 26

3 CHAPTER EXPERIMENTAL SETUP DETAILS 33

3.1 Fabrication of Water Jet Resistant Textured Surfaces 33

3.2 Fabrication of Oxide-modified Metallic Textured Surfaces 35

3.3 Fabrication of Janus Membrane 35

3.4 Preparation of Oil-water Mixtures 38

3.5 Preparation of Organic Pollutants 38

3.6 Visible and Ultraviolet Light Illumination 38

3.7 Microscopy 39

3.8 Contact Angle and Sliding Angle Measurements 39

3.9 Oil-water Separation and Organic Pollutant Degradation Efficiency 39

4 CHAPTER RESULT AND DISCUSSION 40

4.1 Water Jet Resistant Textured Surfaces 40

4.1.1 Characterization of Candle Soot Dispersion 41

4.1.2 Spray-based Textured Surfaces 45

4.2 Oxide-modified Metallic Texture Surfaces 50

4.3 The Janus Membranes 69

5 CHAPTER CONCLUSION 105

APPENDIX 108

A. 1 Organics photo-degradation model 108

A. 2 Data from organics degradation experiment 111

REFERENCES 114

VITAE 124

LIST OF TABLES

Table A. 1 Effect of fixed UV intensity and varying passes on degradation efficiency. 112
Table A. 2 Effect of varying UV intensity and fixed passes on degradation efficiency. 112

LIST OF FIGURES

Figure 1- 1 Young’s model: a liquid droplet on an ideal solid surface. 4
Figure 1- 2 A schematic illustration of Wenzel’s regime. 7
Figure 1- 3 A schematic illustration of Cassie-Baxter regime. 8
Figure 1- 4 Wetting behavior of solid surfaces by modifying surface energy [32]. 10
Figure 1- 5 The possible pathways of the photogenerated electron-hole pair [44]. 12
Figure 1- 6 Time scale of the possible path ways for photo-generated electron-hole pair and photocatalytic reactions in TiO_2 [45]. The examples of the photo-induced interfacial reactions are methanol oxidation, thiocyanate (SCN-) oxidation, transfer of electron to the platinum (Pt), reduction of the adsorbed oxygen ($O^{\cdot}_2$) . 13
Figure 2- 1 A schematic illustration of a double-layer TiO_2-based mesh membrane developed by Feng and coworkers for oil-water separation and water-soluble organic pollutants photo-degradation. 16
Figure 2- 2 Photograph of the experimental setup and process used by Feng and coworkers for oil-water separation and photo-degradation of MB dye in water. (a) Oil-water mixture above the membrane before separation. (b) MB dye-contaminated water stays on the membrane after the separation process. (c) The experimental setup was fixed vertically before the photo-degradation process under UV illumination. (d) After 2 hours of UV illumination, MB dye in water was degraded and MB dye-free water was collected at the bottom due to the simultaneous photo degradation of the superhydrophobic coating on the feed side mesh. 17
Figure 2- 3 The wettability of the prepared TiO_2-based mesh and ODP coated TiO_2-based mesh by Feng and coworkers. (a) TiO_2-based mesh is superhydrophilic (water contact angle is 0). (b) OPD coated TiO_2-based mesh is superhydrophobic (water contact angle is greater than 150 degree). (c) The wettability of OPD coated TiO_2-based mesh by oil. (d) The evaluation of water contact angle on OPD coated TiO_2-based mesh as a function of time. 18
Figure 2- 4 A schematic illustration of DL-PET membrane developed by Zhang and coworkers and its application for the oily wastewater treatment. 20
Figure 2- 5 Oil-water separation and photodegradation of rhodamine b (1 ppm) in water under visible light irradiation using the DL-PET Membrane. (b) Absorbance spectra of rhodamine b-contaminated water before and after the experiment. 21
Figure 2- 6 SEM images of (a) bare stainless steel mesh and the inset is a photograph the shows the flexibility of the mesh. (b), (c) and (d) SEM images at different magnifications for ZnO nanowires coated membranes prepared by Ho and coworkers. 23

Figure 2- 7 SEM and TEM images of Pt (a and b), Ag (c and d) and CuO (e and f) loaded ZnO nanowire coated membrane prepared by Ho and coworkers. 24

Figure 2- 8 (a) and (b) Methylene orange photodegradation and its first order kinetics which was done by Ho and coworkers using ZnO coated membrane and CuO loaded ZnO coated membrane. (c) Oil-water separation using the prepared oil-passing membrane. 25

Figure 2- 9 The wettability of water-passing multifunctional membrane developed by Zhai and coworkers. (a) and (b) are water and underwater oil contact angles (CA=0 and OCA=156.7 degree) on the surface of the prepared membrane with pore size of 260 mm. (c) The effect of the pore size of the prepared membrane on water and underwater oil contact angles. 27

Figure 2- 10 The oil-water separation process done by Zhai and coworkers using the prepared membrane with pore size of 260 µm. (a) Oil-water mixture (ether-MB dye-contaminated water) above the membrane. (b) and (c) Oil is retained by the membrane and MB dye-contaminated water permeates through the membrane. 28

Figure 2- 11 The photocatalytic activity of the water-passing multifunctional membrane prepared by Zhai and coworkers. (a) A schematic illustration of the photocatalytic reactor used to degrade MB dye from water under UV illumination. The multifunctional membrane was sandwiched between two glass vessels as indicated. (b) The photocatalytic activity of the multifunctional membrane to degrade MB dye in water with three pore sizes as indicated. Cycle refers to the number of times water is added to the photodegradation system. 29

Figure 2- 12 A schematic illustration of the β-FeOOH coated nylon mesh as water-passing membrane prepared by Feng and coworkers for oil-water separation and simultaneous photodegradation of MB dye in water. 30

Figure 2- 13 Water-oil separation and in situ photodegradation of MB dye in water reported by Feng and coworkers. (a) Oil (toluene) is retained and colorless water (droplet per 2 seconds) is collected at the bottom. (b) The absorbance spectra of MB dye-contaminated water before and after the experiment. The photographs of the samples are presented in the inset. 32

Figure 3 - 1 Preparation of candle soot dispersions. (a) Candle soot collection: A 250 ml glass beaker is inverted on 5 candle flames such that the zone of incomplete combustion strikes the walls of the beaker for 5 minutes (~250 mg of soot). (b) Sonication of collected candle soot in different solvents. The highly stable, homogeneous dispersion of the candle soot in different solvents were prepared by simply mixing the candle soot coated on the beaker with the solvents (250 mg soot dispersed in 250 ml of each solvent), and sonicating it for 5 minutes

(c) Photograph of prepared candle soot nanoparticles in different solvent as indicated (ethanol, isopropanol and acetone). 34
Figure 3 - 2 Fabrication procedure of the Janus membrane. 37
Figure 4 - 1 Characterization of the prepared Candle soot. (a) TEM images with higher magnification (inset). The candle soot dispersion consists of a large number of nanospheres in the size range of 20 to 50 nm (b) High resolution TEM image of the candle soot and its SAED pattern (inset). It indicates the presence of few pieces of crystalline carbon nanospheres in candle soot along with amorphous carbon, which is further confirmed by Selected Area Electron (c) XPS spectrum. It indicates that the candle soot consists mostly of carbon nanoparticles. The inset in the figure shows the deconvolution of C1s peak (d) Raman shift of the candle soot. The peak at 1350 cm-1 (D bands) accounts for the amorphous carbon and the one at 1580 cm^{-1} (G bands) corresponds to E2g mode of graphite due to the vibration of sp2-bonded carbon atoms in a 2D hexagonal lattice (e) Surface Area analysis of the candle soot. It is mesoporous material with an average pore size of 7 nm and a BET surface area of 366 m2g-1. (f) Thermogravimetric analysis of the candle soot. The weight loss of the candle soot is less than 3.5 % up to the temperature of 450 °C. 44
Figure 4 - 2 Fabrication of superhydrophobic surfaces using candle soot dispersions. (a) Direct candle flame soot deposition. (a-1 and 2) FE-SEM images of the surfaces prepared by direct candle flame soot deposition with different magnifications, (a-3) Cross sectional view of the surfaces prepared by direct candle flame soot deposition. (b) Spray coating method. (b-1 and 2) FE-SEM images of spray based coatings with different magnifications and (b-3) cross sectional view of spray based coatings. It shows the compact nature of this coating. (c) Robustness test of both surfaces. (d) Thermal stability test of spray-based coating. Both surfaces (candle-based coating and spray-based coating) are superhydrophobic with high static water contact of 163o ± 2 and very low sliding contact angle less than 2o. The surfaces fabricated by the candle-based coating loses its superhydrophobicity by the impact of water droplets, whereas the spray-based surface is very robust under the same test. 47
Figure 4 - 3 A schematic illustration of fabrication procedure and application of the annealed membranes. 53
Figure 4 - 4 FE-SEM images of the pristine membrane (PM) and the membranes annealed at 800 °C and at 1000 °C as indicated. 55
Figure 4 - 5 FE-SEM images at higher magnification of the pristine membrane (PM) and the membranes annealed at 800 °C and at 1000 °C as indicated. 56
Figure 4 - 6 FE-SEM images at higher magnification of the pristine membrane (PM) and the membranes annealed at 800 °C and at 1000 °C as indicated. 57

Figure 4 - 7 FE-SEM images at higher magnification of the pristine membrane (PM) and the membranes annealed at 800 °C and at 1000 °C as indicated. 58
Figure 4 - 8 FE-SEM images at higher magnification of the pristine membrane (PM) and the membranes annealed at 800 °C and at 1000 °C as indicated. 59
Figure 4 - 9 FE-SEM images at higher magnification of the pristine membrane (PM) and the membranes annealed at 800 °C and at 1000 °C as indicated. 60
Figure 4 - 10 FE-SEM images at higher magnification of the pristine membrane (PM) and the membranes annealed at 800 °C and at 1000 °C as indicated. 61
Figure 4 - 11 XPS spectra of the pristine and annealed membranes as indicated. Inset is a photograph to show the color of the pristine and annealed membrane. 62
Figure 4 - 12 (a) Wettability, (b) Oil-water separation, and (c) flux and water retention of the pristine and annealed membranes as indicated. 64
Figure 4 - 13 (a) A schematic diagram of the photocatalytic reactor. (b) and (c) The absorption spectra of MB dye at regular time interval using stainless steel mesh annealed at 800 °C and 1000 °C respectively. (d) The photodegradation efficiency of the annealed membranes at 800 °C and 1000 °C as indicated. 68
Figure 4 - 14 A schematic illustration of fabrication procedure and wettability. (a) Spray-coating based fabrication, wettability and morphology of the Janus membrane: SiO_2/SF-100 dispersion and FS-50 solution are sequentially sprayed onto the feed side of the membrane (side facing the water to be treated) while a TiO_2 dispersion is sprayed onto the permeate side of the membrane (side facing the treated water). Then, the Janus membrane was annealed at 80 ^oC for 10 minutes. Inset photos show water and hexadecane droplets on both sides of the Janus membrane and SSF coated glass to show the transparency of SSF coating. 73
Figure 4 - 15 FE-SEM images of the uncoated membrane, feed-side and the permeate-side coatings at different magnifications as indicated. 75
Figure 4 - 16 The advancing contact angles of uncoated, FS-50 coated, SiO_2 coated, and SiO_2/SF-100/FS-50 (SSF) coated glass by water and hexadecane. 77
Figure 4 - 17 The improvement of the feed-side coating due to using SF-100. 78
Figure 4 - 18 Advancing contact angles for hexadecane on the feed-side of the Janus membrane and water flux as a function of the number of passes. 80
Figure 4 - 19 The photocatalytic degradation efficiency for five separate feed samples with the same initial concentration of MB dye and volume after 10 passes for each sample using the same membrane at a constant UV intensity. 81
Figure 4 - 20 Concentration and degradation efficiency per two passes of organic pollutants (Methylene Blue dye) using TiO_2 coated membranes as a function of number of passes at constant UV light intensity. 82

Figure 4 - 21 The calibration curve of the photo-degradation efficiency of MB dye on TiO_2 coated membrane versus the area under the MB absorbance curve (area under the curve, A). 83
Figure 4 - 22 A schematic illustration of the Janus membrane that can separate oil-water mixtures without water pre-wetting by gravity and photo-degrade organic pollutants from the water phase upon UV light illumination. 85
Figure 4 - 23 Absorbance spectra of the organic MB dye after consecutive passes at UV intensity of 1050 mW/cm^2. Inset photos show water-contaminated MB dye before and MB dye-free water after 10 passes. 86
Figure 4 - 24 The physical adsorption of MB dye on TiO_2 coated membrane compared with initial concentration of MB dye and the photolysis of MB dye by UV light on uncoated membrane at the lowest and highest intensities used in this study (372 and 1050 mWcm^{-2}). 87
Figure 4 - 25 A schematic illustration of organics degradation system and relevant parameters for photo-degradation model 89
Figure 4 - 26 Degradation efficiency of TiO_2 coated membrane as a function of number of water passes at constant UV light intensity. 92
Figure 4 - 27 Photo-degradation efficiency of TiO_2 coated membrane as a function of UV light intensity at constant number of passes. 93
Figure 4 - 28 Photo-degradation efficiency as a function of **X**. Symbols correspond to empirical data while the dashed line corresponds to the photo-degradation model. 94
Figure 4 - 29 A schematic illustration of the separation and photo-degradation apparatus used in our experiments.. 96
Figure 4 - 30 (a) A photograph of the apparatus with free 1:1 hexadecane-water mixture above the Janus membrane. (b) and (C) Hexadecane is retained whereas MB dye-free water is collected after 10 passes. 97
Figure 4 - 31 Thermogravimetric analysis (TGA) data of water, hexadecane, and feed solution permeate after 10 passes with high oil rejection. 98
Figure 4 - 32 (a) A photograph of the apparatus with 1:1 emulsified hexadecane-in-water mixture above the Janus membrane. (b) Oil is retained whereas MB dye-free water is collected after 1 pass upon UV light with intensity ≥ 548 mW/cm^2 when the flux is 128 L/m^2-hr. 100
Figure 4 - 33 Thermogravimetric analysis (TGA) data of water, hexadecane, and feed solution permeate after one pass with high oil rejection. 101
Figure 4 - 34 Photo-degradation efficiency of the Janus membrane as a function of UV light intensity at one pass of 1:1 oil-in-water emulsion. 102
Figure 4 - 35 (a), (c) and (e) show the optical microscopy images of 1:4, 1:1, and 4:1 (hexadecane:water by volume) emulsions, respectively. (b), (d) and (f) show droplet size distributions of 1:4, 1:1, and 4:1 emulsions, respectively. (g), (h)

and (I) show the optical microscopy images of 1:4, 1:1, and 4:1 permeates, respectively. 104

Figure A. 1 (a) SEM image of twill Dutch weave mesh, (b) Digital visualization of twill Dutch weave mesh [132]. http://www.spoerl.de/en/wp-content/uploads/sites/2/2014/08/0008_big-458x300.jpg 110

LIST OF ABBREVIATIONS

θ : Contact Angle

θy : Young's Contact Angle

θ_{wv} : Contact Angle of Water in Air

θ_{ov} : Contact Angle of Oil in Air

θ_{ow} : Contact Angle of Oil in Water

θ_{wo} : Contact Angle of Water in Oil

H : Contact Angle Hysteresis

θ_a : Advancing Contact Angle

θr : Receding Contact Angle

θw : Wenzel's Contact Angle

θ_{CB} : Cassie-Baxter’s Contact Angle

γ_{sl} : Interfacial Tension of Solid-Liquid

γ_{sv} : Solid Surface Energy

γ_{lv} : Liquid Surface Tension

r : Surface Roughness

f_s : Fraction of Solid in Contact with Liquid Droplet

f_v : Fraction of Vapor in Contact with Liquid Droplet

e^- : Electron

h^+ : Hole

CB : Conduction Band

VB : Valance Band

e_{tr} : Trapped Electron

h_{tr} : Trapped Hole

$\cdot OH$: Oxidizing Hydroxyl Radical

$O^{\cdot}_2$: Superoxide Radical

UV : Ultraviolet

MB : Methylene Blue

PM : Pristine Membrane

CNP : Carbon Nanoparticle

SSF : SiO_2/SF-100/FS-50

SSF-TiO_2 : SiO_2/SF-100/FS-50-TiO_2

ABSTRACT

Full Name : [Talal Farhan Ahmed Qahtan]

Thesis Title : [Physics of Textured Surfaces with Selective Wettability and Photocatalytic Activity for Multifunctional Applications]

Major Field : [Physics]

Date of Degree : [December, 2017]

Combination of oil-water separation and water-soluble organic pollutants removal in a single unit operation is highly desirable for oily wastewater remediation (i.e. separation of water-insoluble oils and degradation of water-soluble pollutants). In this study, we fabricated textured surfaces with selective wettability and photocatalytic activity (i.e. multifunctional textured surfaces) for oily wastewater treatment in a single unit operation.

For developing of specific materials which act as superhydrophobic (water contact angle > 150^o and sliding angle < 10^o) and superoleophilic (oil contact angle ~ 0^o), a facile synthesis method for highly stable carbon nanoparticle (CNP) dispersion through the incomplete combustion of paraffin candle flame is presented. The synthesized CNP dispersion is the mixture of graphitic and amorphous carbon nanoparticles size in 20-50 nm range and manifested the mesoporosity with an average pore size of 7 nm and a BET surface area of 366 m^2g^{-1}. As an application of this material, the carbon nanoparticle dispersion was spray coated (spray-based coating) on a glass substrate to fabricate water jet resistance superhydrophobic surfaces.

Also, we developed a universal, scalable, solvent-free, one-step methodology based on thermal annealing of stainless steel meshes to create appropriate surface texture and simultaneously modify its surface energy (i.e, chemical composition, Fe_2O_3 and/or Fe_2O_3-

based composites). These annealed stainless steel meshes are mechanically robust and exhibit under-water selective wettability of water over oil for gravity driven oil-water separation and visible light responsive photocatalytic activity for water-soluble organic pollutants degradation under visible light irradiation. We believe that our approach will enable the fabrication of robust multifunction membranes for large-scale applications in oily wastewater treatment.

Furthermore, for the first time, a simple and facile spray coating method was successfully used to fabricated a novel Janus membrane that possess superhydrophilic-superoleophboic surface on the feed side and photocatalytic surface on the permeate side. We developed a mathematical model that describe the photocatalytic degradation of organics upon UV illumination and showed that our model match very well with the experimental result. Our Janus membrane exhibits high separation efficiency of free/emulsified oil-water mixtures and high in-situ photo-degradation efficiency of organic pollutants in the water-rich permeate upon UV light illumination. We believe that our Janus membrane has a great potential for large-scale treatment of oily wastewater.

ملخص الرسالة

الاسم الكامل: طلال فرحان احمد قحطان

عنوان الرسالة: فيزياء السطوح `ذات خاصية البلل الانتقائي والتحفيز الضوئي للتطبيق متعدد الوظائف

التخصص: فيزياء

تاريخ الدرجة العلمية: ديسمبر 2017

انتاج سطوح تمتلك خاصيتي البلل الانتقائي والتحفيز الضوئي(متعددة الوظائف) امر مرغوب فيه لتقليل الكلفة التشغيلية لوحدات معالجة مياه الصرف الصحي الزيتية. هدفت هذه الدراسة الى انتاج سطوح متعددة الوظائف لفصل الزيت من الماء بواسطة خاصية البلل الانتقائي وتنقية الماء من الملوثات العضوية المذابة بواسطة التحفيز الضوئي.

تتكون هذه الدراسة من ثلاثة اجزاء رئيسية: الجزء الاول يتناول تكوين جسيمات الكربون النانوية من سخام الشموع ومن ثم تطبيقها لانتاج سطوح ذات بلل انتقائي (طاردة للماء وقابلة للبلل بالزيت). بينما الجزء الثاني يتناول انتاج غشاء متعدد الوظائف (طارد للزيت تحت الماء وتنقية الماء تحت تاثير الضوء المرئي) عن طريق تسخين غشاء فولاذي غير قابل للصدأ عند درجات حرارة مختلفة. الجزء الثالث من هذه الدراسة يتناول انتاج غشاء متعدد الوظائف المزدوج عن طريق طلاء السطح الامامي للغشاء بمادة طاردة للزيت وقابلة للبلل بالماء وطلاء السطح الخلفي بثاني اوكسيد التيتانيوم النانوي لتنقية المياه تحت تاثير الضوء البنفسجي.

CHAPTER

INTRODUCTION

Rapid industrial development has led to serious environmental problems including release of unwanted oily wastewater into fresh and marine waters [1, 2]. Oily wastewater contains water-insoluble oily compounds and water-soluble toxic organic molecules which damage the ecosystem and threaten human health [3, 4]. Thus, environmental awareness and stringent regulations have been arisen and led many industries in general and oil and gas industries in particular, to invest in developing technologies for effective remediation of oily wastewater before discharge to the environment [5- 9]. Remediation of oily wastewater requires two separate steps (i) the separation of water-insoluble oil and (ii) the removal of the water-soluble pollutants [10-14]. Membrane technologies have proven to be very efficient for separating oil-water mixtures as they are relatively energy-efficient, cost-effective and applicable for a variety of industrial oily wastewater [15]. Furthermore, they require less chemicals as compared to the established conventional techniques such as flocculation, hydrocyclones, and dissolved air flotation [15]. The large-scale application of membranes is limited by membrane fouling due to the adsorption of unwanted components from the feed stream or pore plugging by oil droplets which in turns decline the flux through the membrane. Membranes with selective wettability of water over oil (or vice versa) are of particular interest due to their antifouling property and high oil-water separation efficiency [16,17]. However, these membranes are not capable to remove water-soluble organic pollutants in-situ. The integration of oil-water separation and water-soluble organic pollutants removal in a single unit operation helps to reduce the complexity and the cost of operation in the oily wastewater treatment plants.

1.1 Objectives

The main objective of this study is to develop textured surfaces with selective wettability and photocatalytic activity for oil-water separation and simultaneous organic pollutants degradation under light illumination. The specific objectives of this work are:

1. To study the physics of textured surfaces with selective wettability for oil-water separation.
2. To study the parameters that effect the efficiency of photocatalytic textured surfaces for water-soluble pollutants degradation upon light illumination.
3. To develop experimental skills to fabricate multifunctional textured surfaces for oil-water separation and photo-degradation of water-soluble pollutants.
4. To fabricate in-air and underwater superhydrophilic-superoleophobic textured surfaces on stainless steel mesh by modifying its surface energy.
5. To fabricate superhydrophilic-photocatalytic textured surfaces on stainless steel meshes by modifying its surface energy.
6. To characterize and study the selective wettability and photocatalytic activity of the fabricated surfaces.
7. To apply the multifunctional membranes for gravity-driven oil-water separation and simultaneous water-soluble organic pollutants degradation.

1.2 Wettability

Wetting of solid surfaces by liquids is an interfacial phenomenon that depends on the interfacial energies of solid, liquid and air (or vapor). This wetting behavior can be measured by monitoring the contact angle. The contact angle of a liquid on a solid surface is the angle between the solid surface and the tangent line at the liquid droplet surface. Based on the contact angle value of a water/oil droplet (θ_{wv}/θ_{ov}) on a solid surface in air, solid surfaces can be classified into four regimes: superhydrophobic/superoleophobic ($\theta_{wv}/\theta_{ov} > 150°$), hydrophobic/oleophobic ($\theta_{wv}/\theta_{ov} > 90°$), hydrophilic/oleophilic ($\theta_{wv}/\theta_{ov} < 90°$) and superhydrophilic/superoleophilic ($\theta_{wv}/\theta_{ov} \sim 0°$). Same classification can be applied in different environments like water in oil environment θ_{wo} or oil in water environment θ_{ow}. The real understanding of this phenomenon becomes very much a fertile ground and inspiring source for scientists and engineers to design textured surfaces with selective wettability towards one liquid phase for different applications such as anti-fouling, frost-resisting, anti-fogging and oil-water separation applications[18- 29]. Two fundamental aspects are responsible for selective wettability surfaces. The first aspect is related to the surface energy of the surface [17, 25]. The second aspect is related to the surface texture (nano- and micro roughness)[25].

1.2.1 Wettability of Ideal Solid Surfaces

The contact angle in the case of an ideal (very smooth) surface can be calculated using Young's equation [30]:

$$\cos \theta y = \frac{\gamma_{sv} - \gamma_{\mathrm{sl}}}{\gamma_{lv}} \tag{1.1}$$

This equation depends on the interfacial tension of the solid-liquid (γ_{sl}), solid surface energy (γ_{sv}) and liquid surface tension (γ_{lv}) as depicted in **Fig. 1-1**.

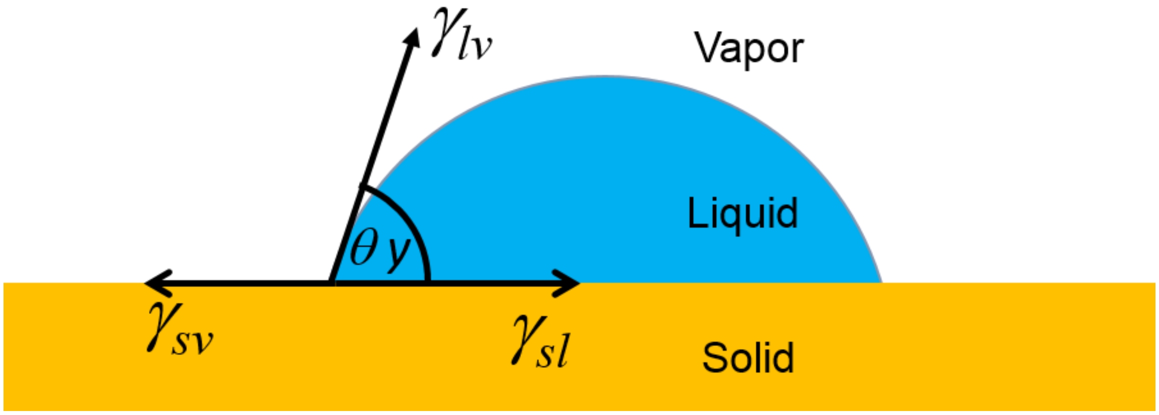

Figure 1- 1 Young's model: a liquid droplet on an ideal solid surface.

1.2.2 Wettability of Textured Solid Surfaces

In reality, no surface can be perfectly ideal due to microscopic texture and small domains with chemical discontinuities depending on surface preparation. For non-ideal surfaces, Young's equation must be modified. We thus need to consider the contact angle hysteresis which is taken to be 0^{o} in the ideal case. Here contact angle hysteresis (H) refers to the difference between advancing (θ_{a}) and receding (θ_{r}) contact angles.

$$H = \theta_{\mathrm{a}} - \theta_{\mathrm{r}} \tag{1.2}$$

The advancing contact angle refers to the maximum stable contact angle after increasing the volume of the droplet, while the receding contact angle revers to the minimum stable contact angle after decreasing the volume of the droplet. These angles and the difference between them vary widely depending on the surface. There are two different regimes in the case of textured surfaces (rough surfaces): (i) Wenzel regime and (ii) Casi-Baxter regime. In the case of Wenzel regime, all of the liquid droplet is in contact with the surface (fully wetted surface). The Wenzel's contact angle (θ_{W}) is different to that measured by Young's equation (θ) because of the roughness of the surface (see **Fig. 1-2**). The Wenzel's contact angle is related to Young's contact angle by the following relation [30]:

$$cos\,\theta_{W} = r\,cos\,\theta y \tag{1.3}$$

Where (r) is the surface roughness which is given by the ratio of the actual surface area to the ideal surface area of the solid surface. The value of r is always greater than 1 because of the surface roughness. When Young's angle is less than 90 degrees, the Wenzel's angle is less than Young's angle. However, when Young's angle is greater than 90 degrees, the Wenzel's angle is greater than Young's angle. This shows that hydrophilicity and hydrophobicity are increased in the Wenzel regime compared to the ideal case. By increasing the roughness of the surface going from the ideal case to non-ideal Wenzel case, hydrophilic surfaces become more hydrophilic and hydrophobic surfaces become more hydrophobic. The liquid droplet in the Wenzel regime demonstrates high contact angle hysteresis; this is because the droplet is in full contact with the surfaces at all points. Wenzel's surfaces also have a high sliding angle, the sliding angle is the elevation angle where a droplet starts moving due to imbalanced of the resultant of forces.

In the case of Cassie-Baxter regime, not all of the liquid droplet is in contact with the rough surface. This is shown in **Fig. 1-3**. There are pockets of air between the lower parts of the droplet and solid surface. As a result, Cassie-Baxter droplet tends to have low sliding angle. In this case, the contact angle (θ_{CB}) is modified further from Young's equation, as given by Equation 1.4 [30, 31]:

$$\cos\theta_{CB} = f_s \cos\theta y + f_{\mathrm{v}} = f_s \cos\theta y + f_s - 1 \qquad (1.4)$$

Where f_s and f_v are the fractions of the solid and vapor respectively which are in contact with the liquid droplet.

$$r = \frac{Actual\ area}{Ideal\ area} = \frac{7a + 6b + 12c}{7a + 6b}$$

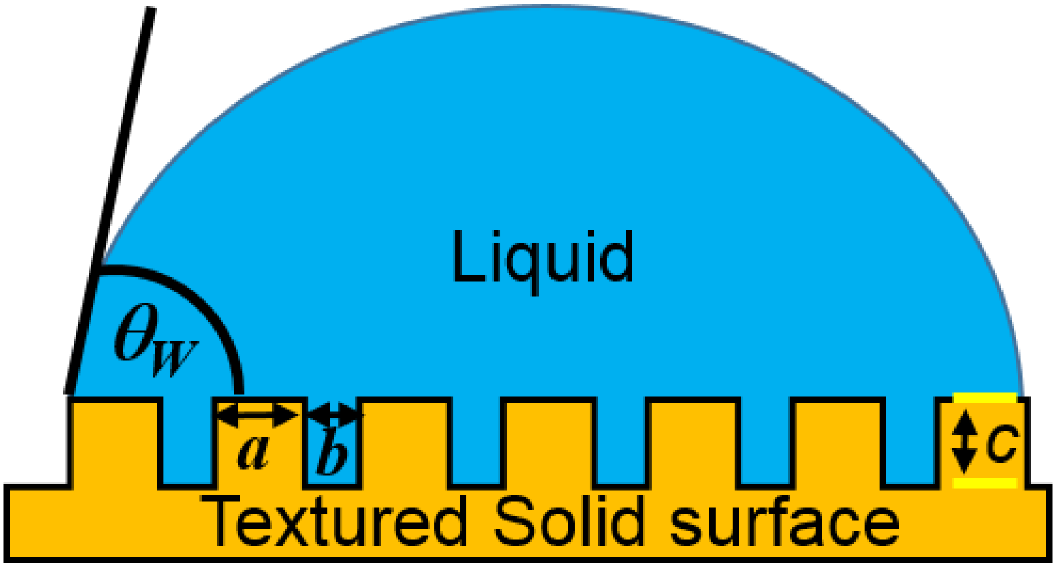

Figure 1- 2 A schematic illustration of Wenzel's regime.

$$f_s = \frac{7a}{7a + 6b} \qquad f_v = \frac{6b}{7a + 6b}$$

$$f_s + f_v = 1$$

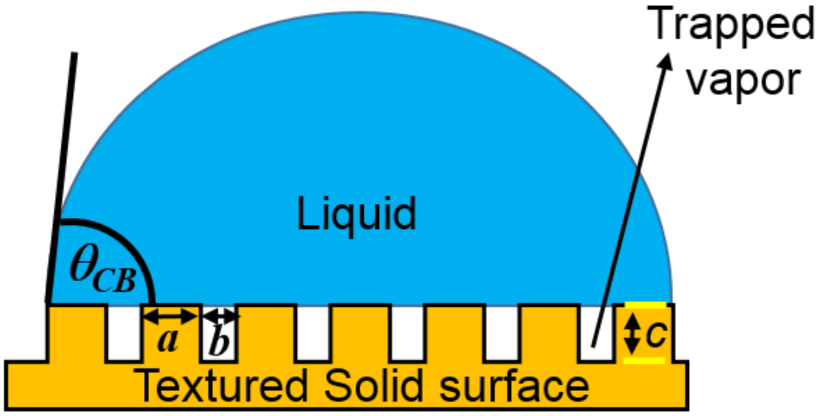

Figure 1- 3 A schematic illustration of Cassie-Baxter regime.

1.2.3 Membrane-based Oil-water Separation

One of the major problems that faces membrane-based technology is membrane fouling at the feed side due to surface adsorption of unwanted components, or plugging of membrane pores by oil droplets, resulting in flux decline [15- 17]. The modification of membrane surface energy to have selective wettability towards either the oil or water phase, is very effective in controlling fouling resistance [15- 17]. **Figure 1-4** describes the wettability behavior of a solid surface by modifying solid-vapor interfacial surface energy (γ_{sv}) relative to oil-vapor (γ_{ov}) and water-vapor (γ_{wv}) interfacial tensions. A high surface energy solid would tend to be hydrophilic-oleophilic (wet by both water and oil). On the other hand, a low surface energy solid would tend to be hydrophobic-oleophobic (non-wettable by both water and oil). In the case of an intermediate solid surface energy, hydrophobic-oleophilic surfaces can be obtained. Based on the above illustration, it is clear that there is no case where the surface is hydrophilic-oleophobic in air. In general, this kind of surface is difficult to fabricate unless the surface is functionalized in some way to introduce surface groups that enhance polar interactions (reorient themselves) to attract water molecules.

There are two types of selective membranes: oil-passing, hydrophobic (or superhydrophobic) and oleophilic (or superoleophilic), membrane and water-passing, hydrophilic (or superhydrophilic) and oleophobic (or superoleophobic), membranes. Based on **Fig. 1-4**, oil-passing membranes are relatively easy to fabricate by reducing the solid surface energy of the membrane through some surface modification.

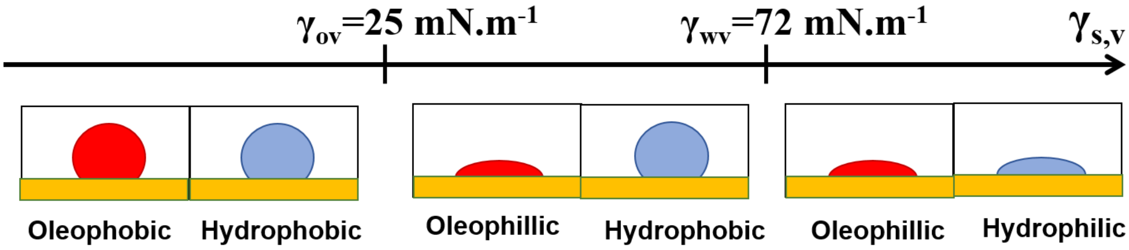

Figure 1- 4 Wetting behavior of solid surfaces by modifying surface energy [32]**.**

Oil-passing membranes are easily fouled due to the accumulation of viscous oil leading to flux decline during the separation, so it is desirable to use water-passing membranes instead for two reasons: (i) they are fouling resistant due to their intrinsic oleophobicity, so they are expected to show better performance. (ii) They are suitable for gravity-driven separation because water density is higher than that of oils. Based on Young's equation and Cassie-Baxter's relation, superhydrophilic rough surfaces in air can become superoleophobic under water due to solid-oil-water interface [32, 33]. This is the first kind of water-passing membranes which can be used for oil-water separation under gravity and they show anti-fouling properties due to the superoleophobisity under water. But, they are suitable to separate oil-water mixtures only if it is pre-wetted by water before the separation process. The second kind of water-passing membrane, super-hydrophilic and in air oleophobic (or super-oleophobic) membranes, can be used for oil-water separation without pre-wetting [16, 17, 34, 35].

1.3 Photocatalytic Semiconductors

After oil-water separation process, it is needed to decompose water-soluble pollutants. Photocatalytic semiconductors such TiO_2 are good choice in this regard as they can break down water-soluble pollutants in the presence of light illumination [36- 39]. The basic theory of the photocatalytic reaction on the surface of semiconductor photocatalysts is based on the creation of electron-hole pairs under light illumination [40- 42]. When a semiconductor photocatalyst absorbs photons with sufficient energy that matches to its band gap energy, the electrons (e^-) in the valence band (VB) get excited to the conduction band (CB) leaving positive holes (h^+) in the valence band. The photogenerated electron-hole pairs are involved in interfacial redox reactions on the surface of the photocatalyst leading to the photocatalytic process such as water splitting, CO_2 reduction, and organic pollutants degradation. **Figure 1-5** shows a schematic illustration of the possible pathways for the photogenerated electron-hole pair in TiO_2 [44]. The photogenerated electron and hole either recombine inside the bulk (path b) releasing heat or diffuse through the bulk and get trapped in trapping sites on the surface. The trapped electron (e_{tr}) either involves a reduction process (i.e acceptor molecules, path d) or recombines with a traped hole (h_{tr}), path a. Similarly, the trapped hole either involves in an oxidation process (i.e donor molecules, path c) or recombines with a tapped electron, path a. In the oxidation reaction, the trapped holes react with adsorbed water or hydroxyl molecules on the surface of the photocatalyst to generate highly chemically active free radicals (i.e oxidizing hydroxyl radicals, $\cdot OH_s$). whereas in the reduction reaction, the trapped electrons react with adsorbed oxygen molecules generating superoxide radicals ($O^{\cdot}_2$) anion which in turn react with adsorbed water or hydroxyl molecules to generate more oxidizing hydroxyl radicals ($\cdot OH_s$). The photodegradation of water-soluble organic pollutants is attributed to the high oxidizing activity of these generated free radicals [43- 45]. The time-scale of the photoinduced electron-hole generation and reaction is presented in **Fig. 1-6.**

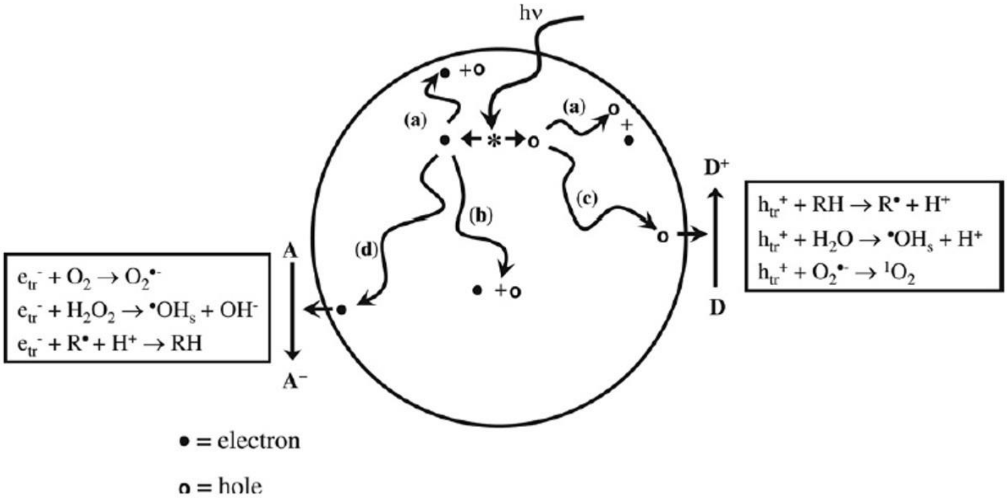

Figure 1- 5 The possible pathways of the photogenerated electron-hole pair [44].

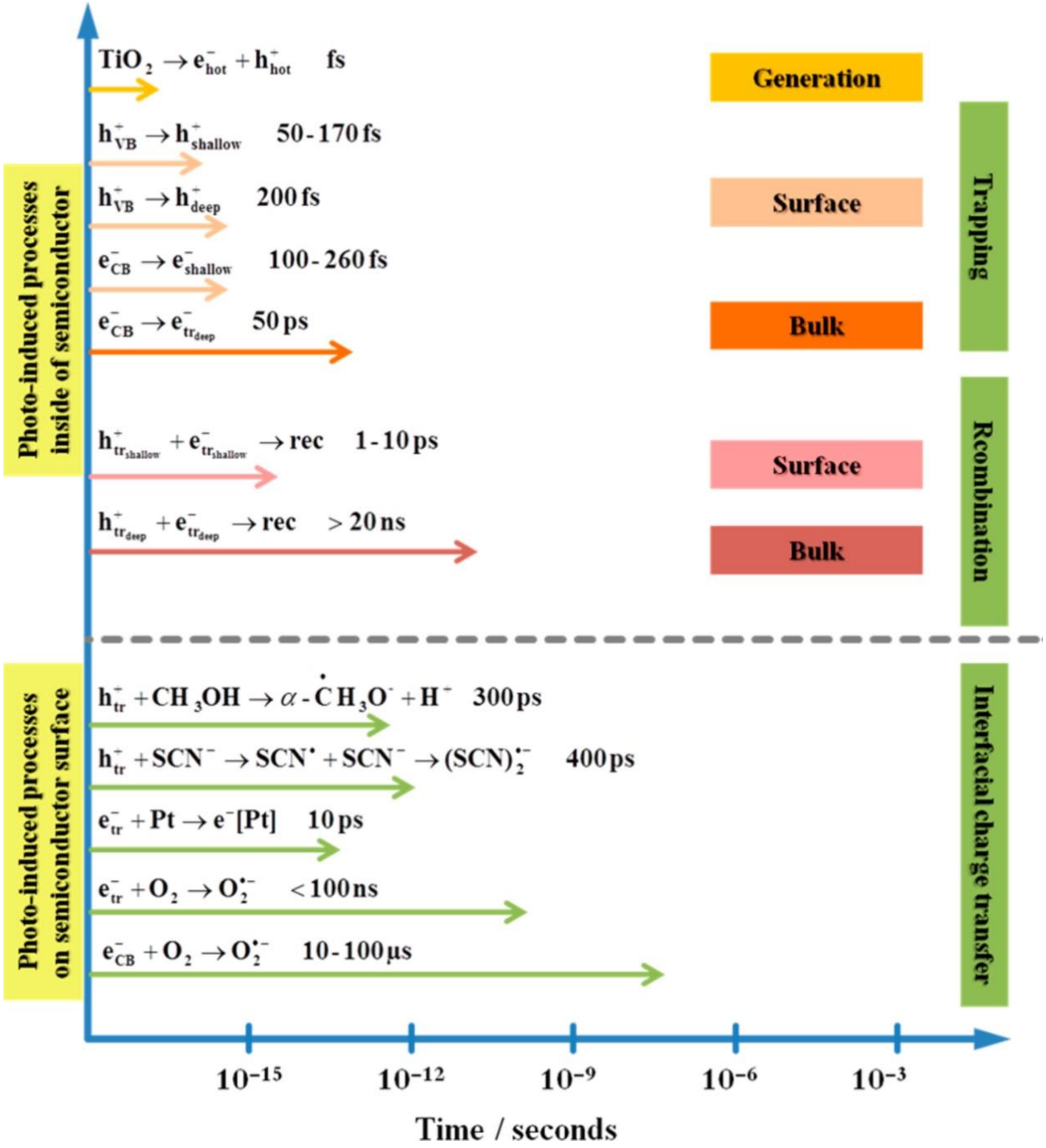

Figure 1- 6 **Time scale of the possible path ways for photo-generated electron-hole pair and photocatalytic reactions in TiO_2 [45]. The examples of the photo-induced interfacial reactions are methanol oxidation, thiocyanate (SCN-) oxidation, transfer of electron to the platinum (Pt), reduction of the adsorbed oxygen (O^{-}_{2}) .**

CHAPTER

LITERATURE REVIEW

The main objective of this chapter is to summarize the recent published literature on the development of multifunctional membranes that can be used for oil-water separation and degradation of water-soluble organic pollutants upon light illumination.

2.1 Oil-passing Multifunctional Membranes

The first study on the multifunctional membranes was reported in 2013 [13]. It was reported by Feng and coworkers that TiO_2-based mesh prepared by hydrothermal method can be used for integrated oil-water separation and photo-degradation of methylene blue (MB) dye in water. In a typical process, two copper meshes with a pore size of 45.5 µm were coated by TiO_2 through a low-temperature hydrothermal approach. The copper meshes were suspended in NaCl supersaturated aqueous solutions of titanium trichloride (0.15 M), then kept at 160 ˚C for 2 hours. One of the prepared TiO_2-based meshes was immersed in an octadecylphosphonic (ODP) solution for 48 hours at room temperature. The ODP solution was prepared by mixing 0.5 mM of ODP with 1000:7 volumetric mixture of heptane and 2-propanol. The membrane used in this study is a combination of the two TiO_2-based meshes (double layer TiO_2-based mesh). The feed side of the membrane was TiO_2 coated mesh and the permeate side is TiO_2 coated mesh modified by ODP to fabricate superhydrophobic and superoleophilic membrane (Oil-passing membrane) as shown in **Fig. 2-1**. The prepared oil-passing membrane was sandwiched between two glass tubes as shown in **Fig. 2-2** was used for oily wastewater treatment. In order to test the prepared membrane for oil-water separation, an oil-water mixture (petroleum ether and methylene blue-contaminated water) was poured on the feed-side of the membrane. The experimental setup was tilted to let oil be in contact with the feed side of the oil-passing membrane as shown in **Fig. 2-2a**. As a result of the superhydrophobic property of the membrane, oil penetrates the membrane while water retains, **Fig. 2-2b**. Then, the experimental setup was fixed vertically for the photocatalytic activity test under Ultraviolet (UV) light illumination. After 2 hours of UV illumination on TiO_2-coated membrane, MB dye in water was degraded and MB dye-free water was collected at the bottom due to the simultaneous degradation of the superhydrophobic coating (ODP) on the feed side of the membrane. The wettability of the prepared TiO_2-based mesh and superhydrophobic TiO_2-based mesh was observed by measuring the contact angle of water and oil as shown in **Fig. 2-3**. TiO_2-based mesh is superhydrophilic, whereas ODP coated TiO_2-based mesh is superhydrophobic-superoleophilic as shown in **Fig. 2-3a, b and c**. The photo-degradation of ODP coating on the feed side mesh was evaluated by measuring the water contact angle as a function of time, **Fig. 2-d**. After 2 hours of UV illumination, the contact angle of water reaches to zero indicating the complete photo-degradation of ODP coating.

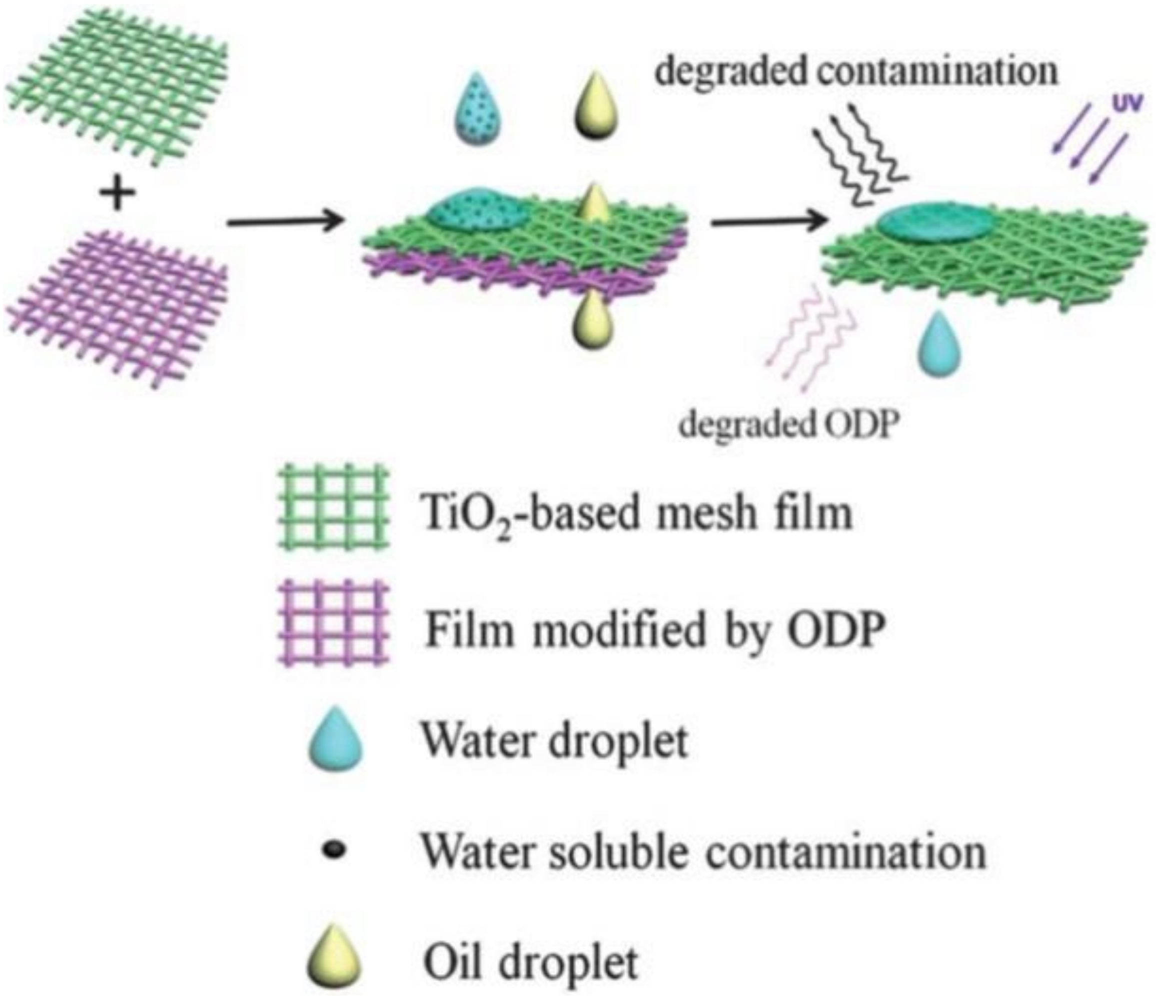

Figure 2- 1 A schematic illustration of a double-layer TiO$_2$-based mesh membrane developed by Feng and coworkers for oil-water separation and water-soluble organic pollutants photo-degradation.

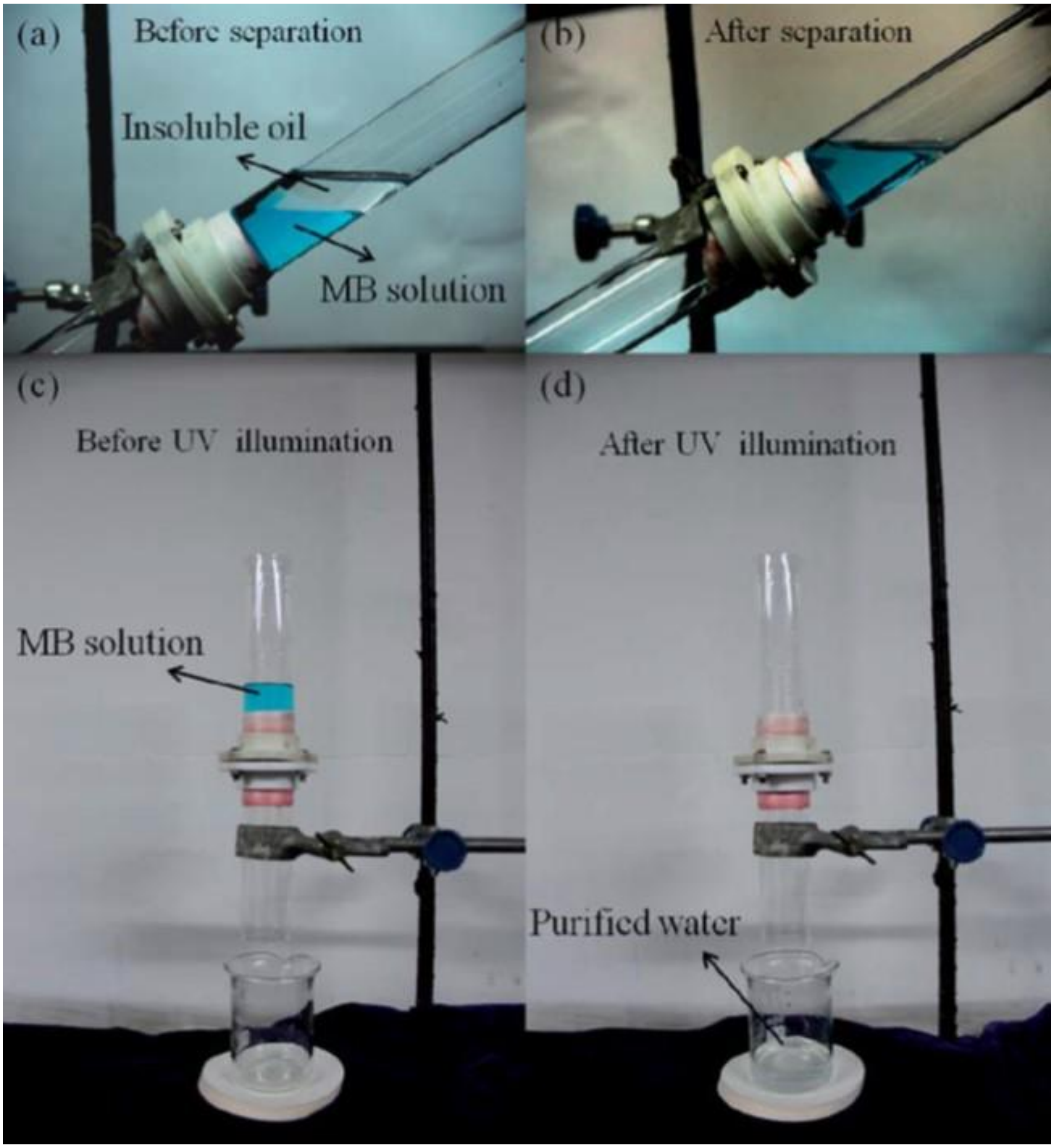

Figure 2- 2 Photograph of the experimental setup and process used by Feng and coworkers for oil-water separation and photo-degradation of MB dye in water. (a) Oil-water mixture above the membrane before separation. (b) MB dye-contaminated water stays on the membrane after the separation process. (c) The experimental setup was fixed vertically before the photo-degradation process under UV illumination. (d) After 2 hours of UV illumination, MB dye in water was degraded and MB dye-free water was collected at the bottom due to the simultaneous photo degradation of the superhydrophobic coating on the feed side mesh.

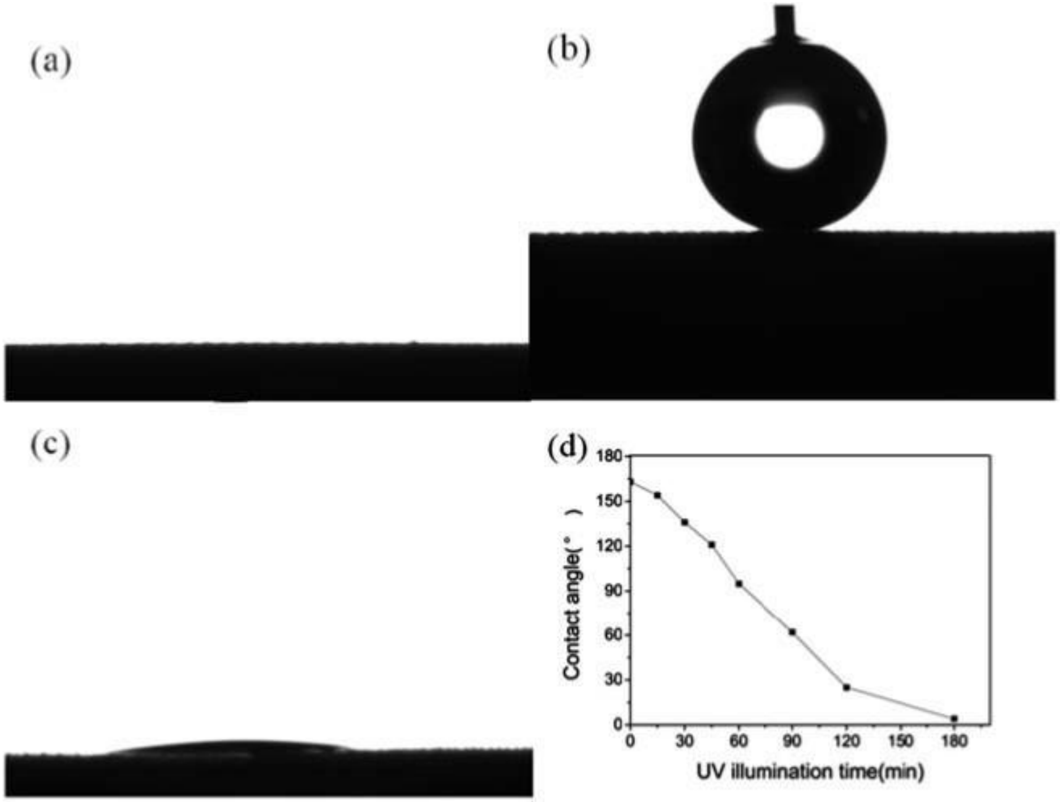

Figure 2- 3 The wettability of the prepared TiO_2-based mesh and ODP coated TiO_2-based mesh by Feng and coworkers. (a) TiO_2-based mesh is superhydrophilic (water contact angle is 0). (b) OPD coated TiO_2-based mesh is superhydrophobic (water contact angle is greater than 150 degree). (c) The wettability of OPD coated TiO_2-based mesh by oil. (d) The evaluation of water contact angle on OPD coated TiO_2-based mesh as a function of time.

In 2014, Zhang and coworkers[10] reported the fabrication of polydopamine (PDA) @ Ag-based double-layer polyester (DL-PET) membrane as an oil-passing membrane for oil-water separation and water-soluble organic days degradation under visible light illumination as shown in **Fig. 2-4**. The feed-side surface is coated by Ag_3PO_4 on PET@PDA@Ag-based textile which is superhydrophilic-superoleophilic and visible light responsive coating. The permeate-side surface is dodecylmercaptan coated PET@PDA@Ag-based textile which is a superhydrophobic-superoleophilic coating. The DL-PET membrane can be used for oil-water separation and degradation of water-soluble organic dyes under visible light illumination as shown in **Fig. 2-5**.

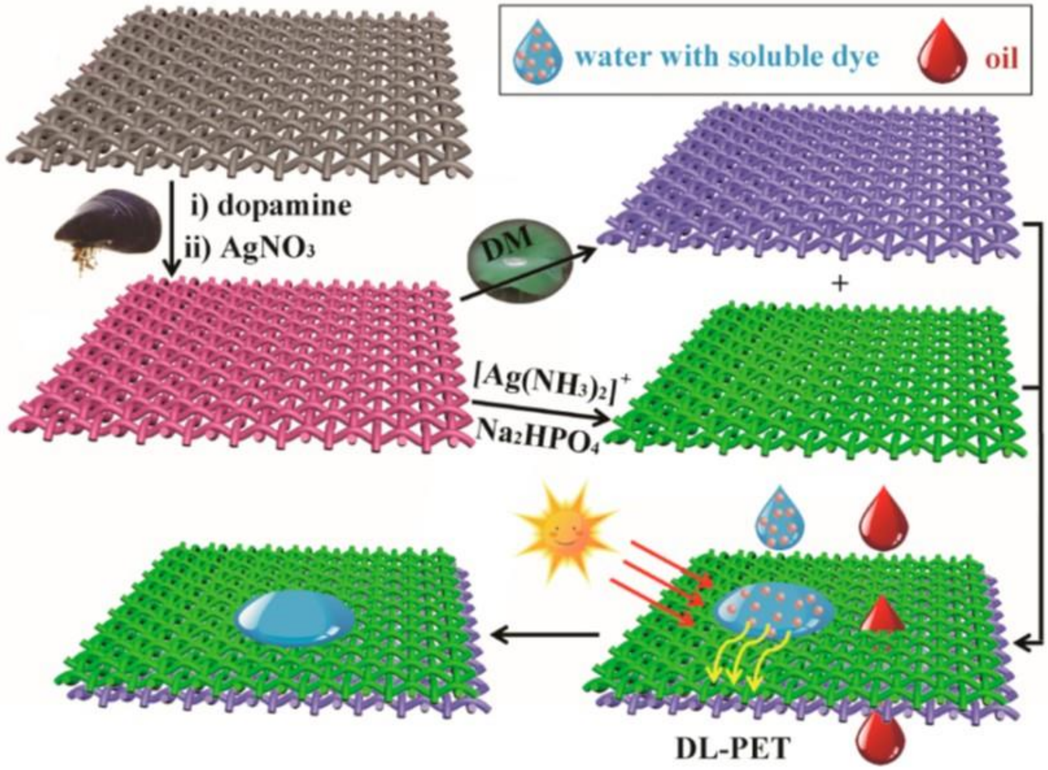

Figure 2- 4 A schematic illustration of DL-PET membrane developed by Zhang and coworkers and its application for the oily wastewater treatment.

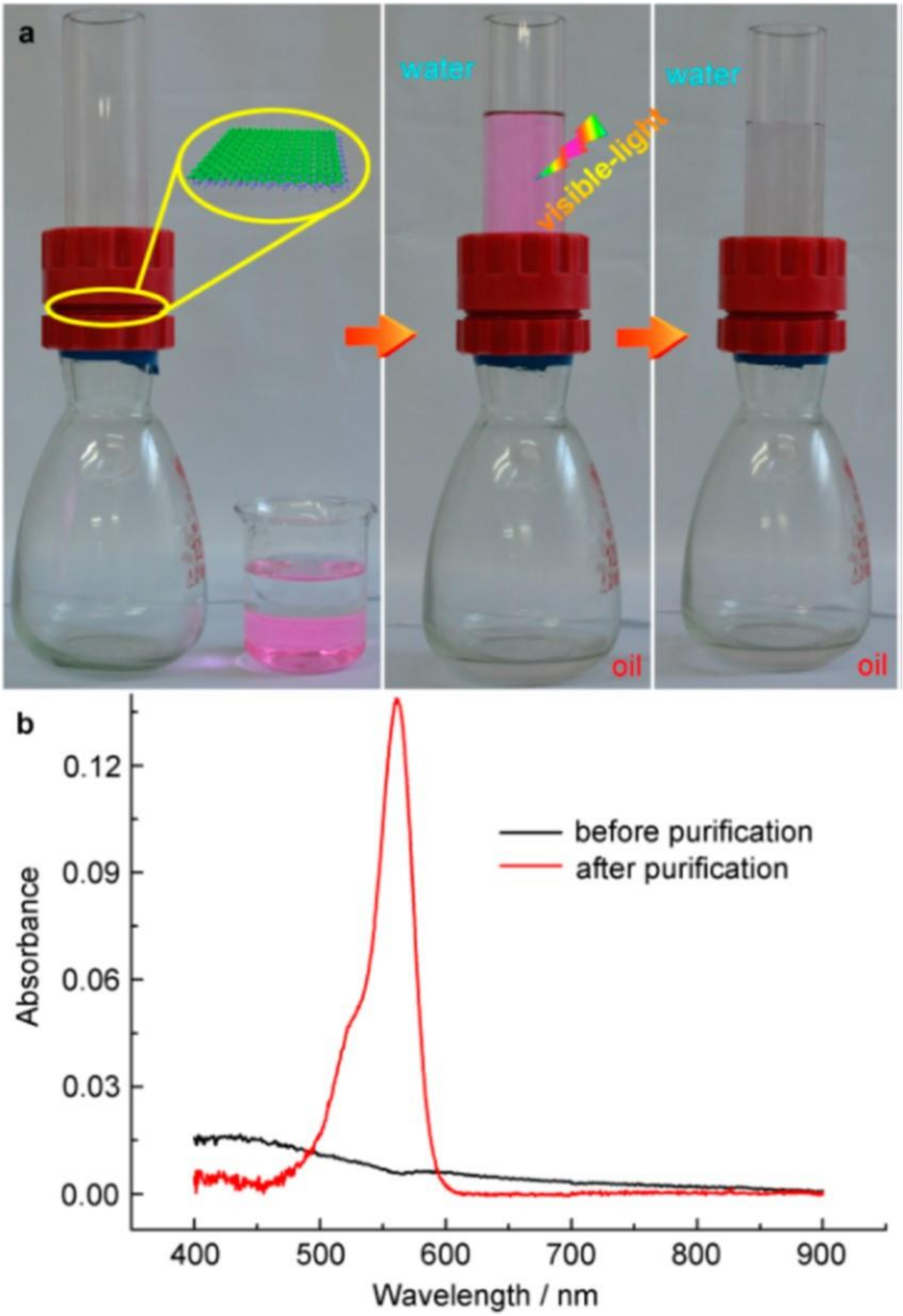

Figure 2- 5 Oil-water separation and photodegradation of rhodamine b (1 ppm) in water under visible light irradiation using the DL-PET Membrane. (b) Absorbance spectra of rhodamine b-contaminated water before and after the experiment.

Ho and coworkers reported in 2014 [47] the fabrication of flexible ZnO nanowire coated stainless steel mesh by hydrothermal methods for remediation of oily wastewater. The SEM image is shown in **Fig. 2-6**. In order to enhance the photocatalytic activity of the prepared membrane, photochemical deposition method was used to load Pt, Ag, or CuO on the surface of ZnO nanowire coated stainless steel mesh as shown in TEM images **Fig. 2-7**. ZnO nanowire coated membrane was treated with stearic acid in order to fabricate a superhydrophobic-oleophilic ZnO coated membrane (oil-passing membrane) for oil-water separation. **Figure 2-8** shows the photodegradation of methylene orange by CuO loaded ZnO coated membrane and ZnO coated membrane as well as the separation of vegetable oil-water mixture by the fabricated oil passing membrane.

As discussed in the previous chapter, oil-passing membranes are easily fouled due to the accumulation of viscous oil which leads to flux decline during the separation. Furthermore, they are not suitable for gravity-driven separation because water naturally settles below the oil due to its higher density.

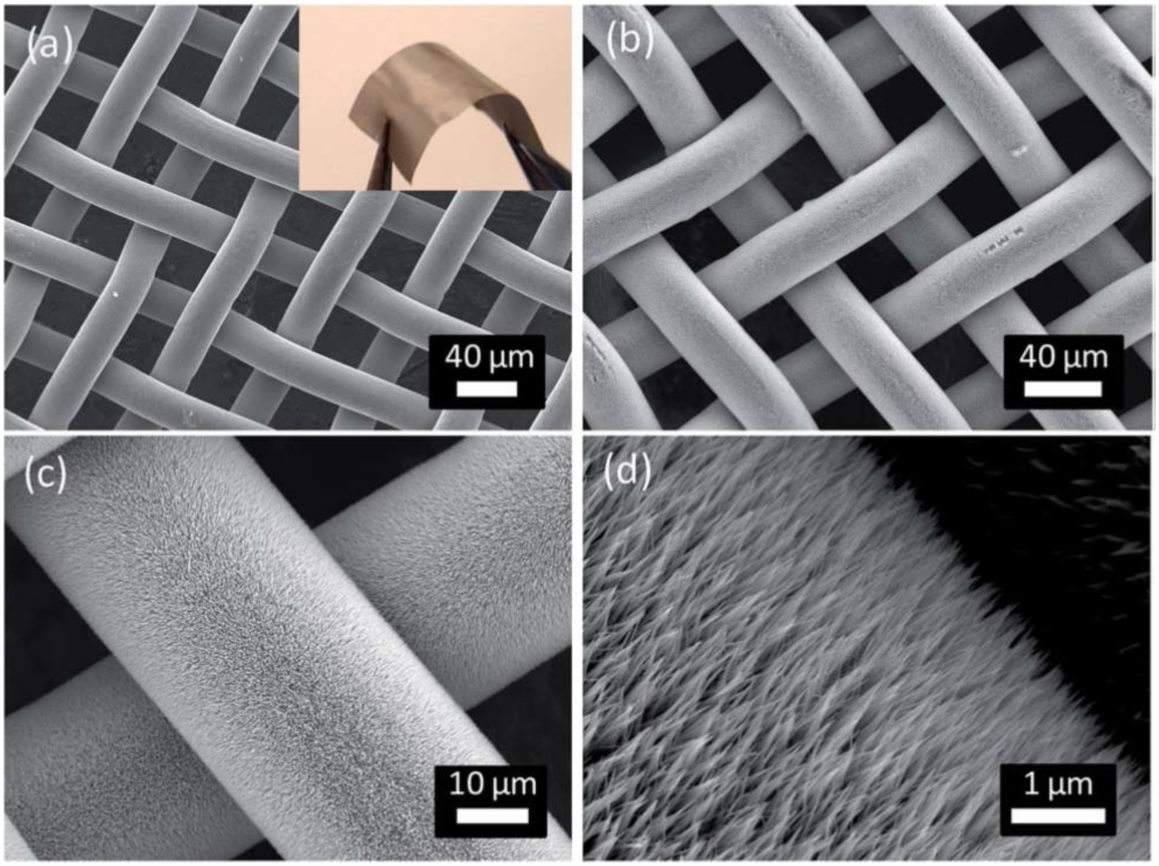

Figure 2- 6 SEM images of (a) bare stainless steel mesh and the inset is a photograph the shows the flexibility of the mesh. (b), (c) and (d) SEM images at different magnifications for ZnO nanowires coated membranes prepared by Ho and coworkers.

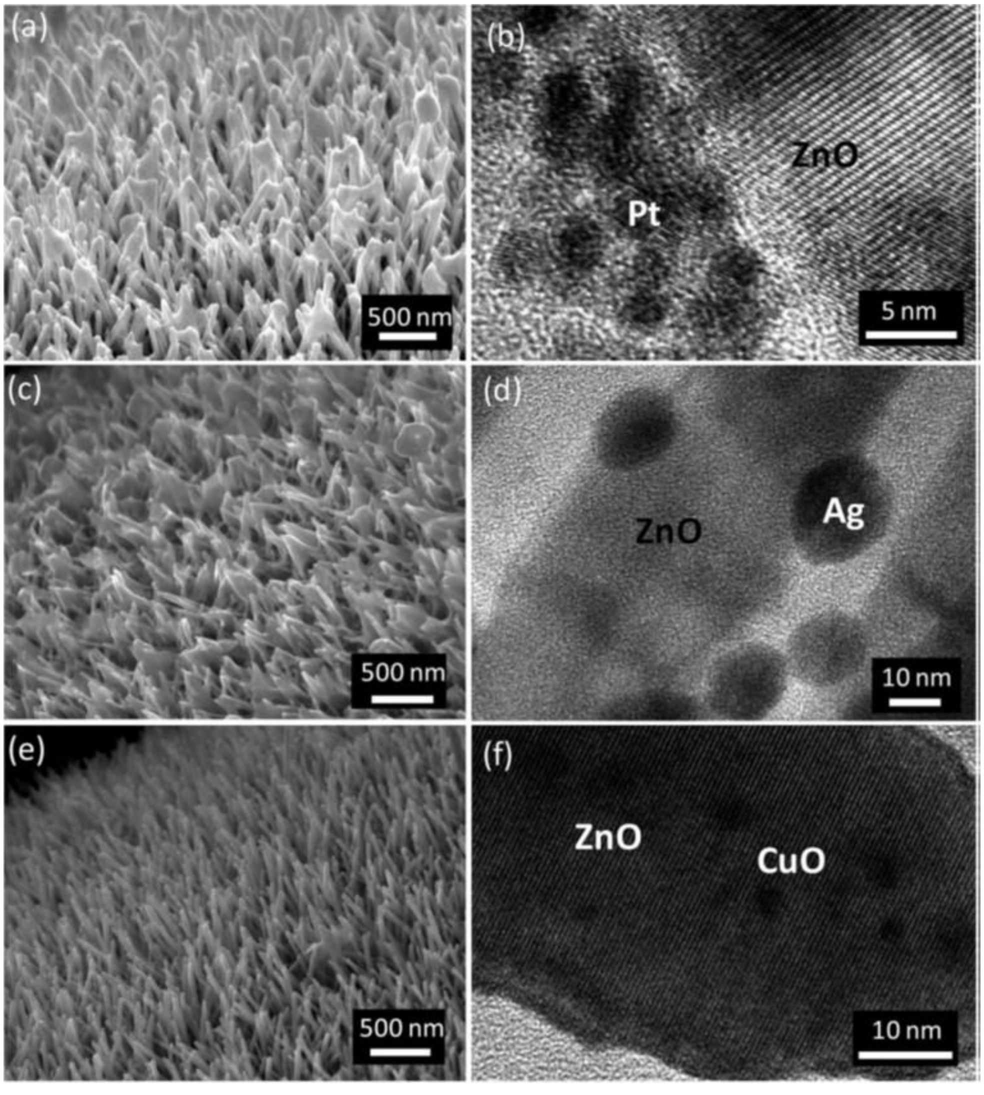

Figure 2- 7 SEM and TEM images of Pt (a and b), Ag (c and d) and CuO (e and f) loaded ZnO nanowire coated membrane prepared by Ho and coworkers.

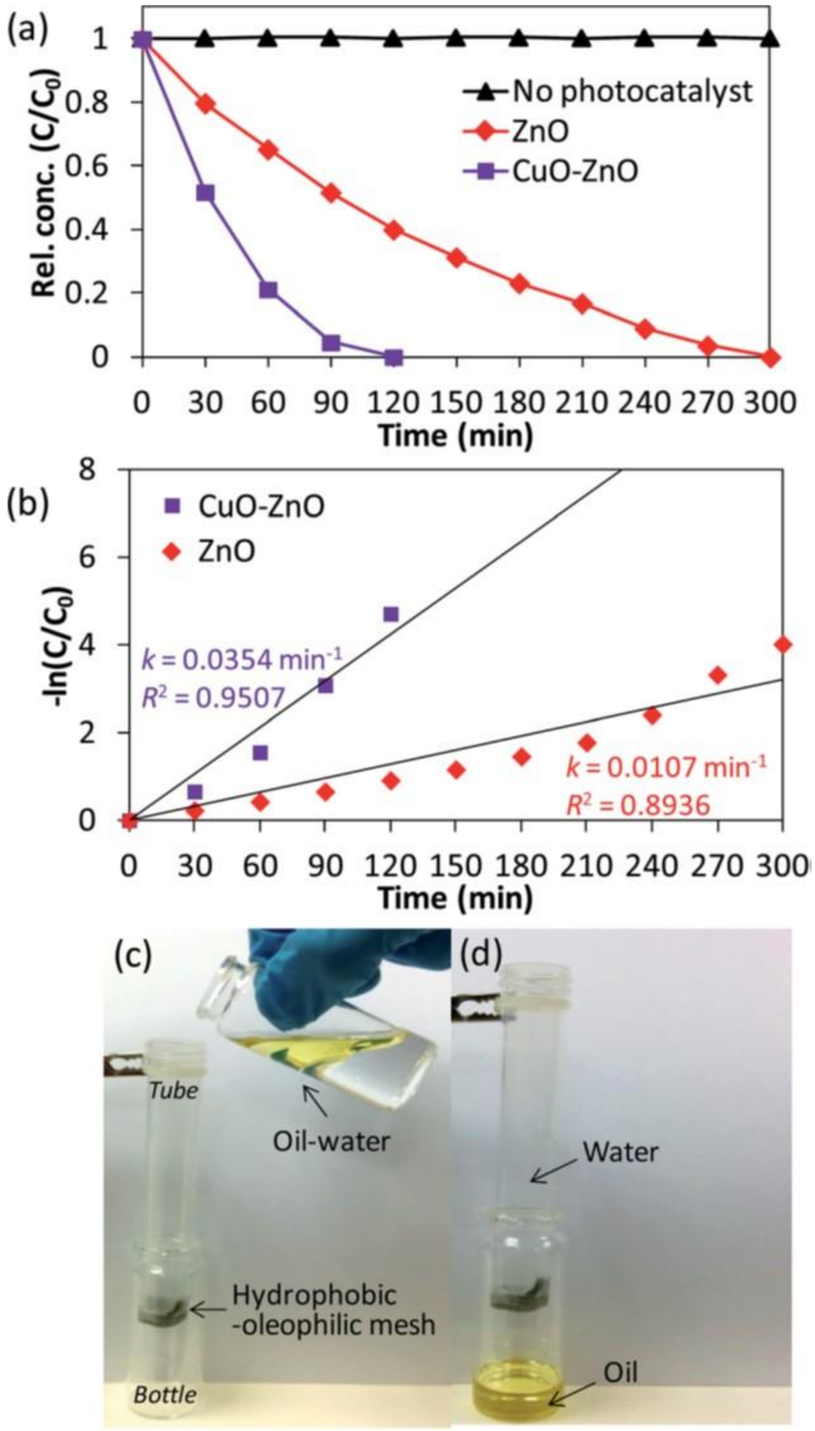

Figure 2- 8 **(a) and (b) Methylene orange photodegradation and its first order kinetics which was done by Ho and coworkers using ZnO coated membrane and CuO loaded ZnO coated membrane. (c) Oil-water separation using the prepared oil-passing membrane.**

2.2 Water-passing Multifunctional Membranes

In 2015, Zhai and coworkers[12] reported the fabrication of a superhydrophilic-underwater superoleophobic porous membrane as a water-passing multifunctional membrane for oil-water separation and simultaneous degradation of water-soluble dyes. They used an electrochemical method to develop the water-passing multifunctional membrane with three pore sizes 80, 120 and 260 μm by fabricating TiO_2 nanotubes on the surface of porous titanium mesh, followed by annealing in air. The prepared membrane is superhydrophilic-superoleophoilic in air and superoleophobic under water as shown in **Fig. 2-9**. Due to the underwater superoleophobicity and photocatalytic activity property of TiO_2, the prepared water-passing multifunctional membrane achieved the separation of oil from oil-water mixture by allowing water to permeate through the membrane as demonstrated in **Fig. 2-10** and degrade MB dye during the permeation of MB dye-contaminated water through the membrane under UV illumination as shown in **Fig. 2-11**.

In 2016, Feng and coworkers[48] reported the fabrication of water-passing multifunctional membrane (β-FeOOH coated nylon mesh) using low-temperature hydrolysis method for oily wastewater treatment under visible light illumination. As illustrated in **Fig. 2-12**, the fabrication process consist of two steps: (i) Fabrication of PDA coated nylon mesh, a nylon mesh was immersed in aqueous solution of dopamine-hydrochloride (DOPA). Meanwhile, a Tris solution with pH of 8.5 was dropwise. The chemical reactor was sealed and kept at room temperature for 48 hours. The PDA coated nylon mesh was removed and rinsed with water for the second step. (ii) Fabrication of β-FeOOH coated nylon mesh, the obtained PDA coated nylon mesh was immersed in $FeCl_3 \cdot 6H_2O$ solution with a concentration of 20 mg mL^{-1} for 24 hours at 40 ˚C.

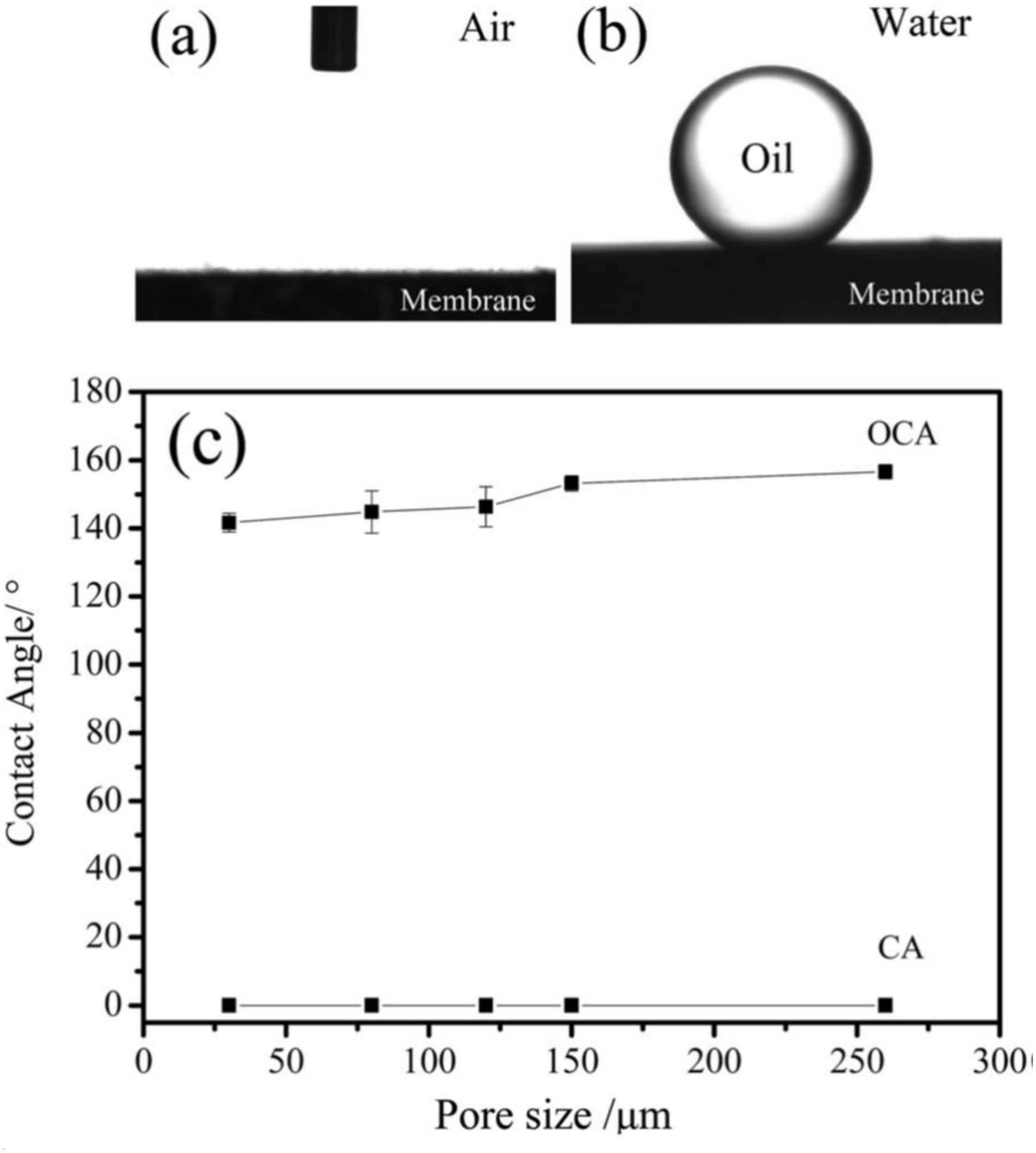

Figure 2- 9 The wettability of water-passing multifunctional membrane developed by Zhai and coworkers. (a) and (b) are water and underwater oil contact angles (CA=0 and OCA=156.7 degree) on the surface of the prepared membrane with pore size of 260 mm. (c) The effect of the pore size of the prepared membrane on water and underwater oil contact angles.

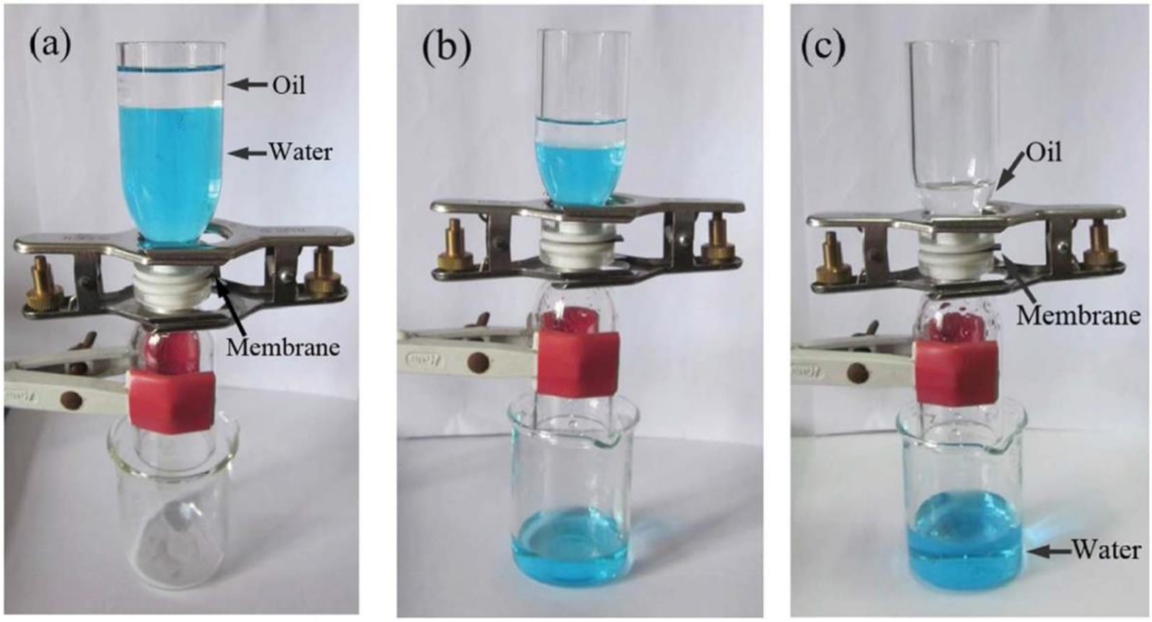

Figure 2- 10 The oil-water separation process done by Zhai and coworkers using the prepared membrane with pore size of 260 µm. (a) Oil-water mixture (ether-MB dye-contaminated water) above the membrane. (b) and (c) Oil is retained by the membrane and MB dye-contaminated water permeates through the membrane.

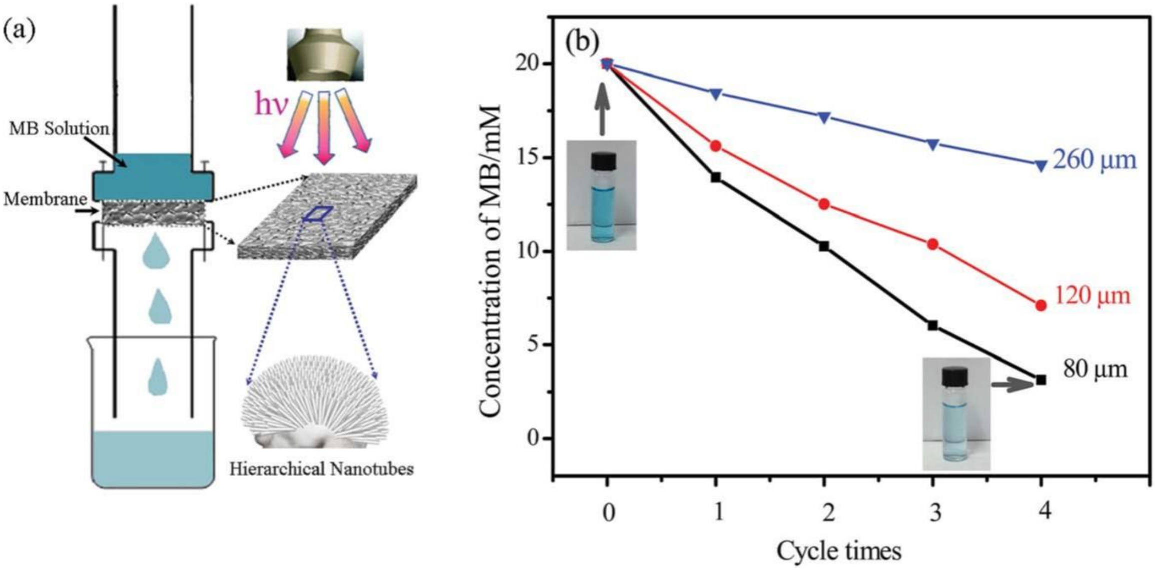

Figure 2- 11 The photocatalytic activity of the water-passing multifunctional membrane prepared by Zhai and coworkers. (a) A schematic illustration of the photocatalytic reactor used to degrade MB dye from water under UV illumination. The multifunctional membrane was sandwiched between two glass vessels as indicated. (b) The photocatalytic activity of the multifunctional membrane to degrade MB dye in water with three pore sizes as indicated. Cycle refers to the number of times water is added to the photodegradation system.

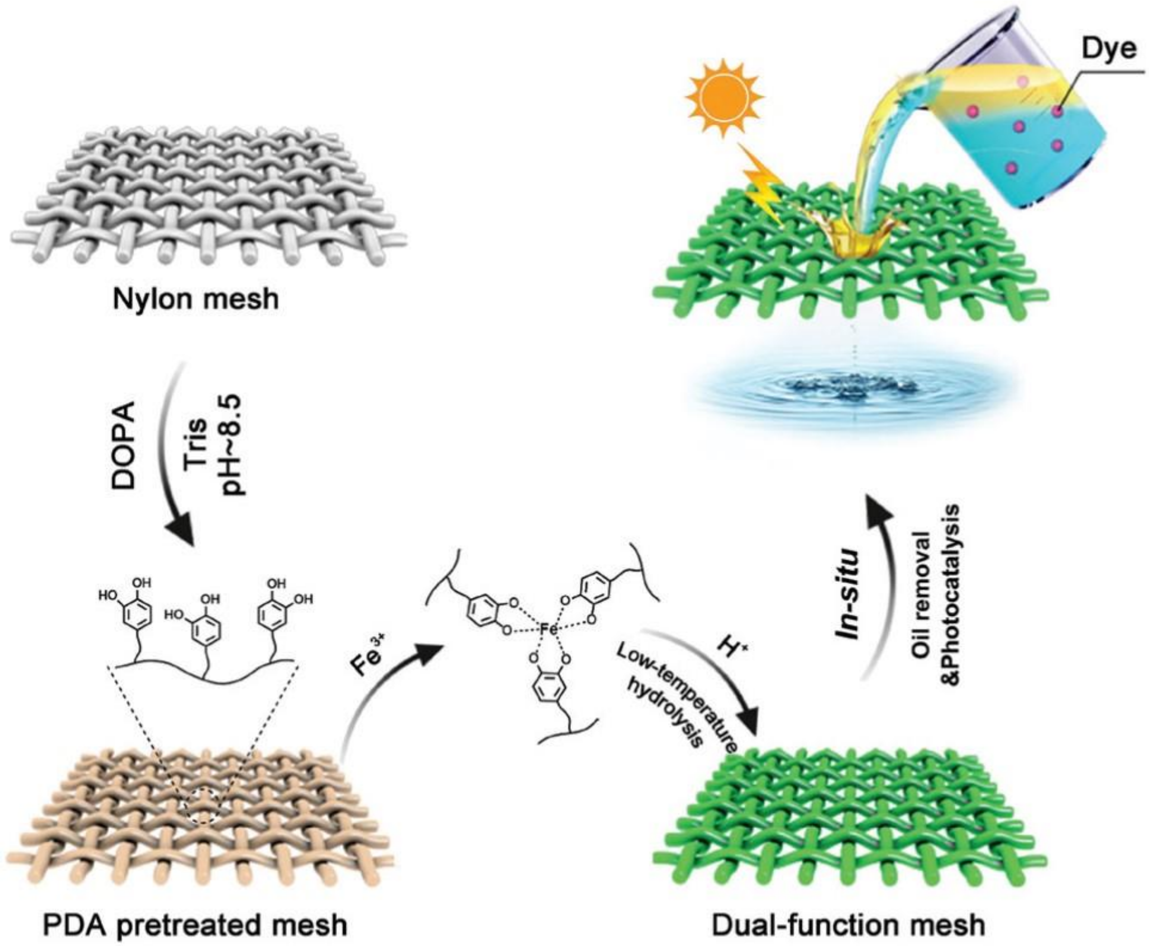

Figure 2- 12 A schematic illustration of the β-FeOOH coated nylon mesh as water-passing membrane prepared by Feng and coworkers for oil-water separation and simultaneous photodegradation of MB dye in water.

The fabricated multifunctional membrane was applied for oil-water separation and in situ photodegradation of MB dye in water. To achieve oil-water (toluene and MB dye-contaminated water) separation and in situ photodegradation of MB dye in water, six multifunctional membranes were sandwiched together between two glass tubes in order to reduce the flux of water. In addition, the entire device was tilted for visible light illumination as shown in **Fig. 2-13**. It was noted that oil is retained by the membrane and a colorless water (one droplet per 2 seconds) was collected at the bottom.

The combination of oil-water separation and water-soluble pollutants degradation in a single unit operation can be used to create more efficient systems and save process costs. There is still need to develop novel multifunctional membrane using cost-effective materials and facile methodology with high selectivity, high separation capacity, stability, fouling-resistant performance and high pollutants degradation efficiency.

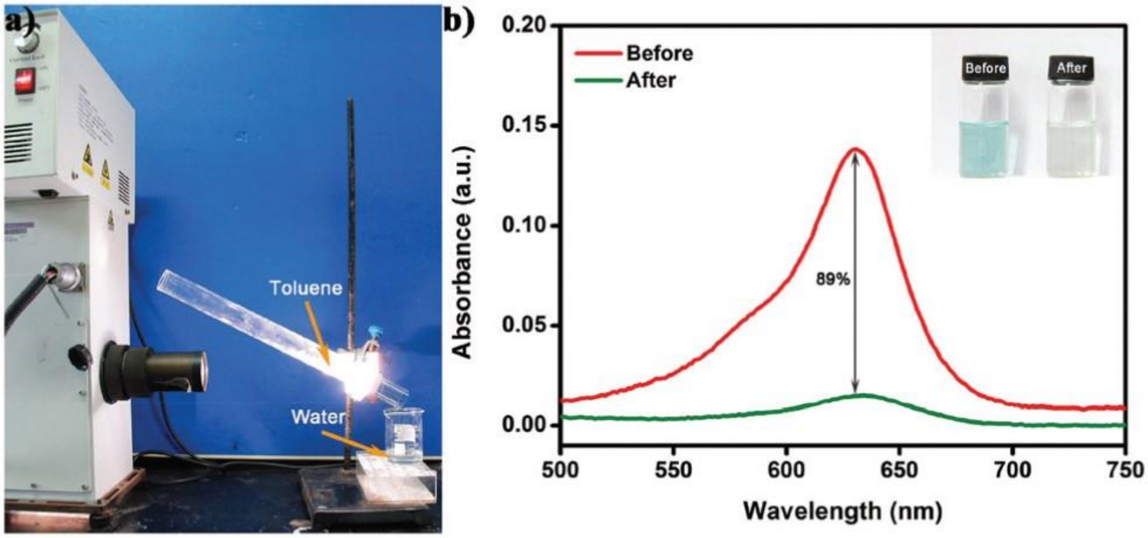

Figure 2- 13 Water-oil separation and in situ photodegradation of MB dye in water reported by Feng and coworkers. (a) Oil (toluene) is retained and colorless water (droplet per 2 seconds) is collected at the bottom. (b) The absorbance spectra of MB dye-contaminated water before and after the experiment. The photographs of the samples are presented in the inset.

CHAPTER

EXPERIMENTAL SETUP DETAILS

3.1 Fabrication of Water Jet Resistant Textured Surfaces

The paraffin candles used in this work are commercially available in the local market. Also, the solvents were of analytical grade from Sigma Aldrich. As shown in Figure 1, a 250 ml glass beaker was inverted on 5 candle flames such that the zone of incomplete combustion strikes the walls of the beaker for 5 minutes gathering approximately 250 mg of the candle soot. Highly stable homogeneous dispersions of the candle soot in the three solvents were prepared by simply mixing 250 mg of candle soot in 250 ml, 500 ml and 750 ml of three solvents (acetone, isoproponol and ethanol) followed by sonication for 5 minutes. For the preparation of superhydrophobic surfaces, 10 ml of all the above nine different combinations of candle soot dispersion were spray coated on 4 cm^2 glass substrates using a spray gun (McMaster Carr). It was found that 10 ml of 250 mg in 250ml dispersion in all three solvents is the optimum quantity and concentration needed to cover 4 cm^2 substrate by soot to fabricate superhydrophobic surfaces. Although, 10 ml of 250 mg in 250ml dispersion in all three solvents gave same result, we chose acetone as a solvent to fabricate superhydrophobic surfaces in this study. The spray gun was operated using nitrogen gas at a pressure of 170 kPa. In order to make the solvent to evaporate readily and get uniform spray-based superhydrophobic surfaces, the substrates were fixed on an electric heater maintained at 100 ^{o}C during the spray coating process.

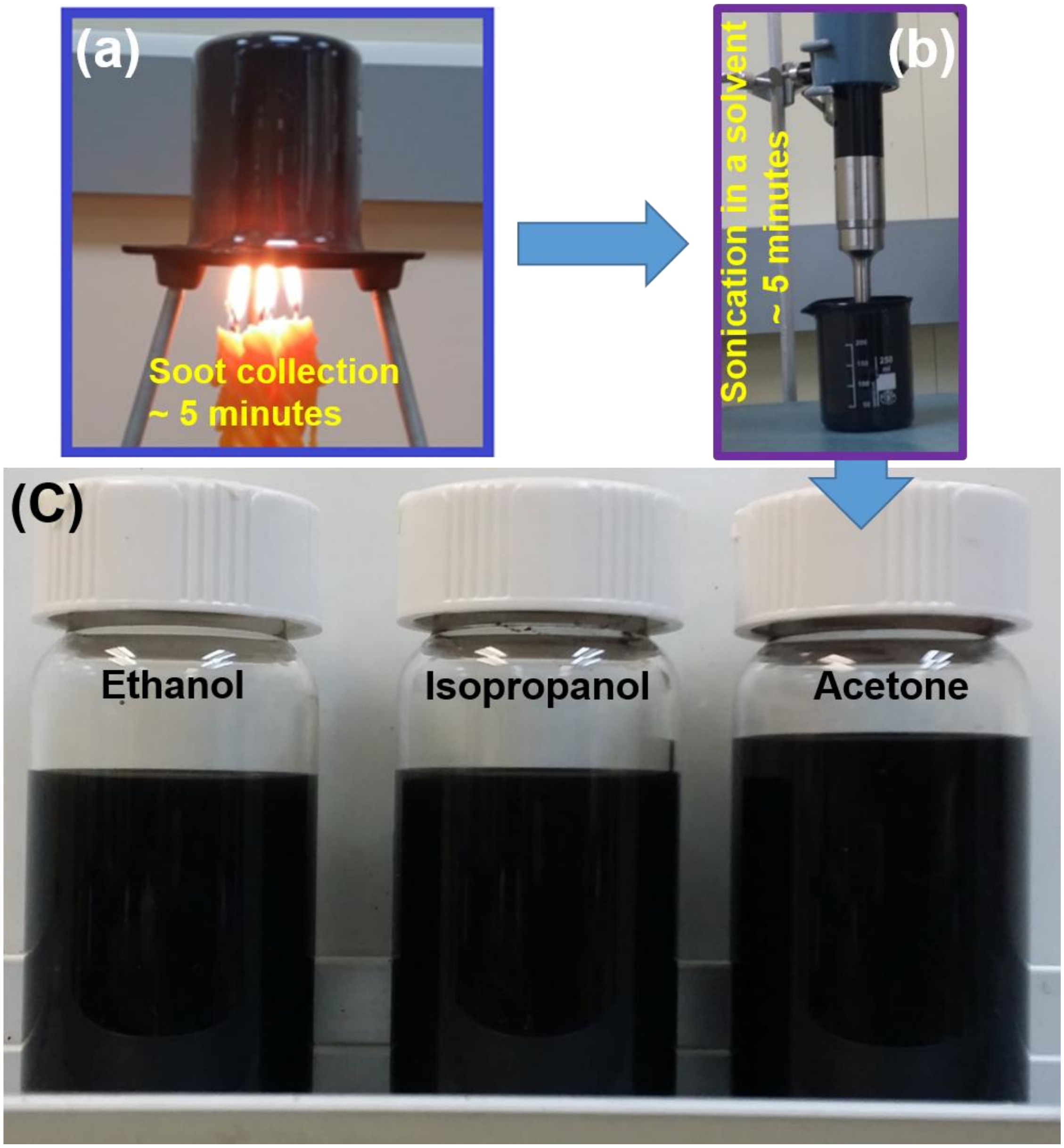

Figure 3 - 1 Preparation of candle soot dispersions. (a) Candle soot collection: A 250 ml glass beaker is inverted on 5 candle flames such that the zone of incomplete combustion strikes the walls of the beaker for 5 minutes (~250 mg of soot). (b) Sonication of collected candle soot in different solvents. The highly stable, homogeneous dispersion of the candle soot in different solvents were prepared by simply mixing the candle soot coated on the beaker with the solvents (250 mg soot dispersed in 250 ml of each solvent), and sonicating it for 5 minutes (c) Photograph of prepared candle soot nanoparticles in different solvent as indicated (ethanol, isopropanol and acetone).

To study the relative merit of the spray-based superhydrophobic surfaces, we fabricated candle-based superhydrophobic surfaces by direct candle flame soot deposition also, where the candle flame was directly intercepted by the substrate. These two variants of surfaces were used for the studies of wettability, stability against drop impact, water jet impingement and thermal stability.

3.2 Fabrication of Oxide-modified Metallic Textured Surfaces

The oxide-modified metallic textured surface are basically the corrosion resistant annealed stainless steel (316L) square meshes of 3 cm sides, 1 mm thickness and 2 micron pore size. Before annealing, the meshes were cleaned with DI water and acetone in an ultrasonic cleaner and dried by nitrogen. The annealing of the stainless steel meshes was carried out at 1 atmospheric pressure in the air environment for 3 hours at 2 different set temperatures (800 °C and 1000 °C), with the heating rate of 5 °C min^{-1}.

3.3 Fabrication of Janus Membrane

316 stainless steel mesh with average pore size of 2 μm (T316L, TWP) and a glass slide (VWR Microscope Slides) were used for porous membranes and non-porous substrate, respectively. SiO_2 nanoparticle suspension (average diameter = 7 nm, Aerosil 380, Evonik Industries) with a concentration of 15 mg/mL was prepared by adding SiO_2 nanoparticles into acetone (Sigma Aldrich) and vigorous stirrering at 800-1000 rpm. Then, 5 mg of SF-100 (Super-fast instant adhesive, 3M Scotch-Weld) was added per 1 mL of SiO_2 nanoparticle solution to yield a SiO_2/SF-100 solution. Fluoro-surfactant solution (Capstone FS-50, DuPont) was prepared by diluting FS-50 with ethanol (Sigma Aldrich) to obtain a 45 mg/mL solution. TiO_2 (Aeroxide TiO_2 P25, Evonik Industries) nanoparticles dispersions with a concentration of 5 mg/mL were separately prepared in tetrahydrofuran

(THF, Sigma Aldrich) using a magnetic stirrer at 800-1000 rpm. All membranes and glass substrates used in this study were rinsed with acetone, isopropanol, and deionized (DI) water, respectively, to remove contaminants and subsequently dried before each coating process. A spray gun (Nozzle diameter of 0.38 mm, Paasche) operated with compressed nitrogen at a pressure of 200 kPa was used. The gun was kept at a distance of 10 cm from the membrane/glass substrate for all coatings. For the SSF coating, 1 mL of SiO_2/SF-100 dispersion and 0.5 mL of FS-50 per 1 cm^2 of membrane or glass slide are sequentially sprayed on the feed side of the membrane /glass substrate. For the TiO_2 coating, 1.5 mL of the prepared dispersions per 1 cm^2 of substrate was sprayed onto the permeate side of the membrane/glass substrate as shown in **Fig. 3-2**. Finally, the SSF-TiO_2 coated membrane/substrate was transferred to an oven operating at 80 C for 10 minutes.

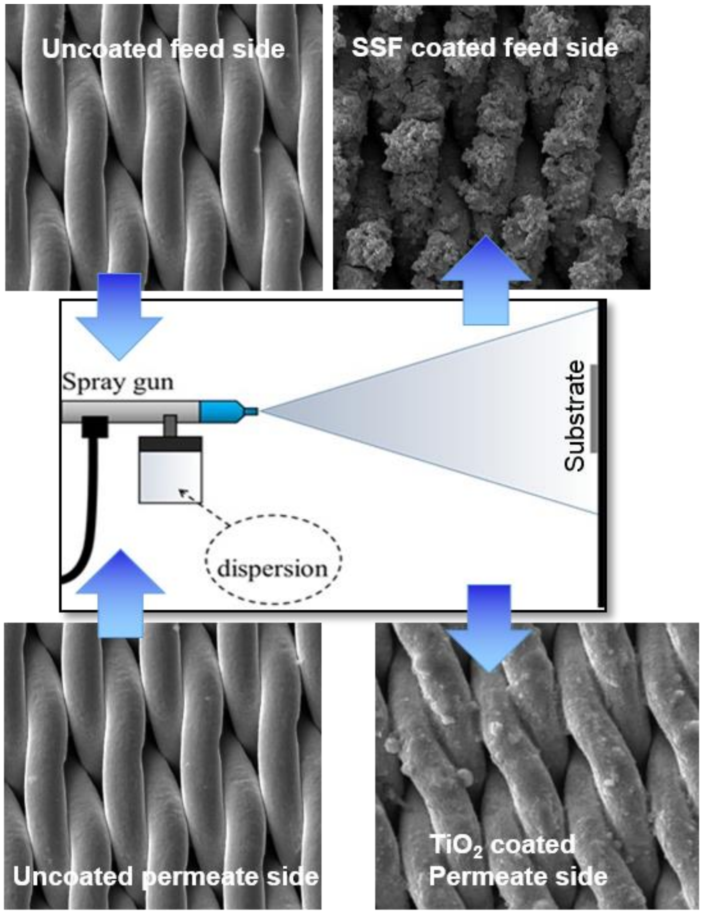

Figure 3 - 2 Fabrication procedure of the Janus membrane.

3.4 Preparation of Oil-water Mixtures

Free oil-water was prepared by mixing hexadecane and deionized water by 1:1 volumetic ratio. Oil-in-water emulsions were prepared with two different volumetric ratios (1:4 and 1:1 hexadecane:water) by mixing hexadecane and deionized water with adding 0.3 mg per mL of solution of sodium dodecyl sulfate (SDS, Sigma Aldrich). Whereas, water-in-oil emulsion with a 1:4 volumetric ratio of water-in-hexadecane was prepared by following the same procedure with adding Span80 (Sigma Aldrich) instead of SDS. All emulsions were mixed using a magnetic stirrer at 800-1000 rpm. The emulsion type was determined by measuring the electrical resistance of the prepared emulsions using a mustimeter. A small degree of emulsification was observed over time for some emulsions. Feed emulsion droplet sizes were digitally extracted from high resolution optical microscope images using the imfindcircles function in the MATLAB image processing toolbox.

3.5 Preparation of Organic Pollutants

MB dye-contaminated water was prepared by mixing 5 mg of MB dye (Sigma Aldrich) with 1000 ml of deionized water.

3.6 Visible and Ultraviolet Light Illumination

Visible light was from 300 W halogen tungsten lamp with a 420 nm cut off optical filter. UV irradiation was from the Mercury Vapor Short Arc UV lamp source (Omnicure S2000), collimated by a collimating adaptor (OmniCure Adjustable Spot Collimating Adaptor) and transmitted through a fiber optic cable. The UV intensity was measured by OmniCure R2000 UV Radiometer.

3.7 Microscopy

A field emission scanning electron microscope (FE-SEM, TESCAN ultra high resolution), was used for surface morphology analysis. An optical microscope (NikonECLIPSE Ti) was used to take optical images of oil-water feed emulsions and water-rich permeate.

3.8 Contact Angle and Sliding Angle Measurements

Droplet volumes used in this study were 5 µL. Static and advancing contact angle measurements were performed using a Goniometer Kruss Easy Drop DSA20X. Sliding angles were measured by increasing the elevation angle of the goniometer stage until each oil droplet began moving due to an imbalance of forces.

3.9 Oil-water Separation and Organic Pollutant Degradation Efficiency

The oil content in all permeates after oil-water separation was measured using thermogravimetric analysis (STA 449F3-Jupiter, Netzsch). The temperature of each sample was increased from room temperature to 105 °C at a rate of 5 °C/min, and then held at 105 °C for 50 min. As the boiling points of water and hexadecane are 100 °C and 287 °C, respectively, the loss in water weight was used to estimate the oil rejection. The concentrations of methyl blue dye before and after photo-degradation were measured with a UV-VIS spectrophotometer (Jasco 670).

CHAPTER

RESULT AND DISCUSSION

4.1 Water Jet Resistant Textured Surfaces

Over the decades, carbon in nano-scale has been synthesized in various morphological structures, such as nanotube, nanowire and other carbonaceous nanomaterial[49], [50]. These materials have been used as sorbents[51] antimicrobial agents[52], environmental sensors[53] and for the storage of gases[53, 54]. All these progress in the studies and applications of carbon nanomaterials are possible due to their novel physical, chemical and mechanical properties which arise from their morphology, high surface area, biocompatibility, low toxicity and chemical inertness inherent to their various nanostructures[56]. To realize the full potential application of carbon nanomaterials, systematic studies of carbon nanoparticle is essential in addition to other nanostructures[48, 49, 51, 56- 58]. On this basis, active research on development of carbon nanoparticles (CNPs) possessing improved chemical and physical properties with potential for many technological applications is an ongoing effort[56- 58]. Recent studies have demonstrated that CNPs can be a good material for photonic applications as they exhibit emission spectra with tunable excitation, high photostability and good electroluminescence[58, 59]. Moreover, CNPs have shown better biocompatibility, chemical inertness and less toxicity compared to conventional heavy metal based quantum dots[59]. All these positive attributes of CNPs can be harnessed for its vital applications like cell imaging and optoelectronics[56,59–61].

Conventional top-down approach adopted for the synthesis of CNPs involves disintegration of bulky carbon material using high impact mechanical process. However, these techniques naturally need high material cost, huge instrumentation and harsh operation conditions[64]. Other possible alternative is the less cumbersome and cost effective bottom-up synthesis route, where CNPs are synthesized by combustion and/or chemical process using readily available organic molecular precursors[64, 65].

In the present work, highly stable carbon nanoparticle (CNP) dispersion was synthesized from candle soot obtained through incomplete combustion of paraffin candle flame. The synthesized CNPs dispersion were found to be highly stable in different solvents (acetone, isopropanol and ethanol) for more than a year under ambient conditions. Superhydrophobic surfaces were fabricated by simply spray coating the candle soot dispersion on a glass surface using a spray-gun (spray-based coating). The superhydrophobic surfaces fabricated exhibit superior resistance to drop impact, water jet impingement and are thermally stable, compared to the same surfaces fabricated from direct candle flame soot deposition (candle-based coating). The striking feature of this method of synthesis is that the experimental set up is simple, the raw material is inexpensive. Moreover, the synthesized dispersion can be easily applied for large-scale fabrication of thermally stable superhydrophobic surfaces with high resistance to drop impact and water jet impingement.

4.1.1 Characterization of Candle Soot Dispersion

Transmission Electron Microscope (TEM) images of the dispersion of carbon nanoparticles (CNPs), through incomplete combustion of paraffin candle flame are shown in **Fig 4-1-a and Fig 4-1-b**. It is quite clear from **Figure 4-1-a** that the candle soot dispersion consists of a large number of nanospheres in the size range of 20 to 50 nm and the magnified version of the TEM image presented in the inset of **Fig 4-1-a** shows that the carbon nanospheres are formed from the irregularly patterned spherical carbon nanoparticles liked through weak Van-der-waals interaction. The agglomeration of carbon nanosphere results due to the presence of dangling bonds, which makes the surface highly reactive[63, 66, 67]. **Fig. 4-1-b** indicates the presence of few pieces of crystalline carbon nanospheres in candle soot along with amorphous carbon, which is further confirmed by Selected Area Electron Diffraction pattern (SAED) shown in the inset of **Fig 4-1-b**. The observable diffraction rings in SAED pattern are due to (002), (100) and (110) planes of crystalline candle soot nanospheres[68, 69].

The chemical composition of the paraffine candle soot was examined by EDS and XPS. The EDS measurements reveal that the main component is carbon (Atomic percentage - 97.0%) and the minor component of oxygen (Atomic percentage - 3.0%). The presence of strong C1s peak in XPS analysis depicted in **Fig. 4-1-c** indicates that these candle soot consists mostly of carbon (Atomic percentage of C1s and O1s are 97.2 and 2.8 respectively) and are free from other elements of organic contaminates, originating from paraffin and/or the environment, which is in a good agreement with EDS results. The inset of Figure 2d shows that C1s is decomposed into three peaks centered at 284.6 eV, 285.6 eV and 286.3 eV which corresponds to sp^2 hybridized C=C, sp^3 hybridized C-C and C-O bonds respectively [71]. The presence of amorphous and graphitic carbon in the candle soot is further substantiated with the Raman spectrum, shown in **Fig. 4-1-d**, where the peak at 1350 cm^{-1} (D bands) accounts for the amorphous carbon and the one at 1580 cm^{-1} (G bands) corresponds to E_{2g} mode of graphite due to the vibration of sp^2-bonded carbon atoms in a 2D hexagonal lattice. The presence of the G band indicates that the candle soot consist of highly ordered pyrolytic graphite[64].

The N_2 adsorption-desorption isotherm displayed by the candle soot is given in **Fig.4-1-e**, which resembles the Type IV isotherm described by Brunauer et al. [61], where the increase in absorption volume at high relative pressure indicates the presence of majority amount of mesopores and negligibly small amount of micropores, however, the presence of hysteresis loop at high relative pressure rules out the presence of macrospores in the candle soot. The textural parameters obtained quantitatively shows that candle soot has an average pore size of 7 nm and large BET surface area of 366 m^2g^{-1}.

In order to study the thermal stability of candle soot, thermal gravimetric analysis (TGA) was carried out and it is clear from **Figure.4-1-f** that up to the temperature of 450 °C, the weight loss of the candle soot is less than 3.5 %, which indicates the absence of significant decomposition. This result ensures that the candle soot dispersion can be used for any applications that require the functional temperature below 450 °C.

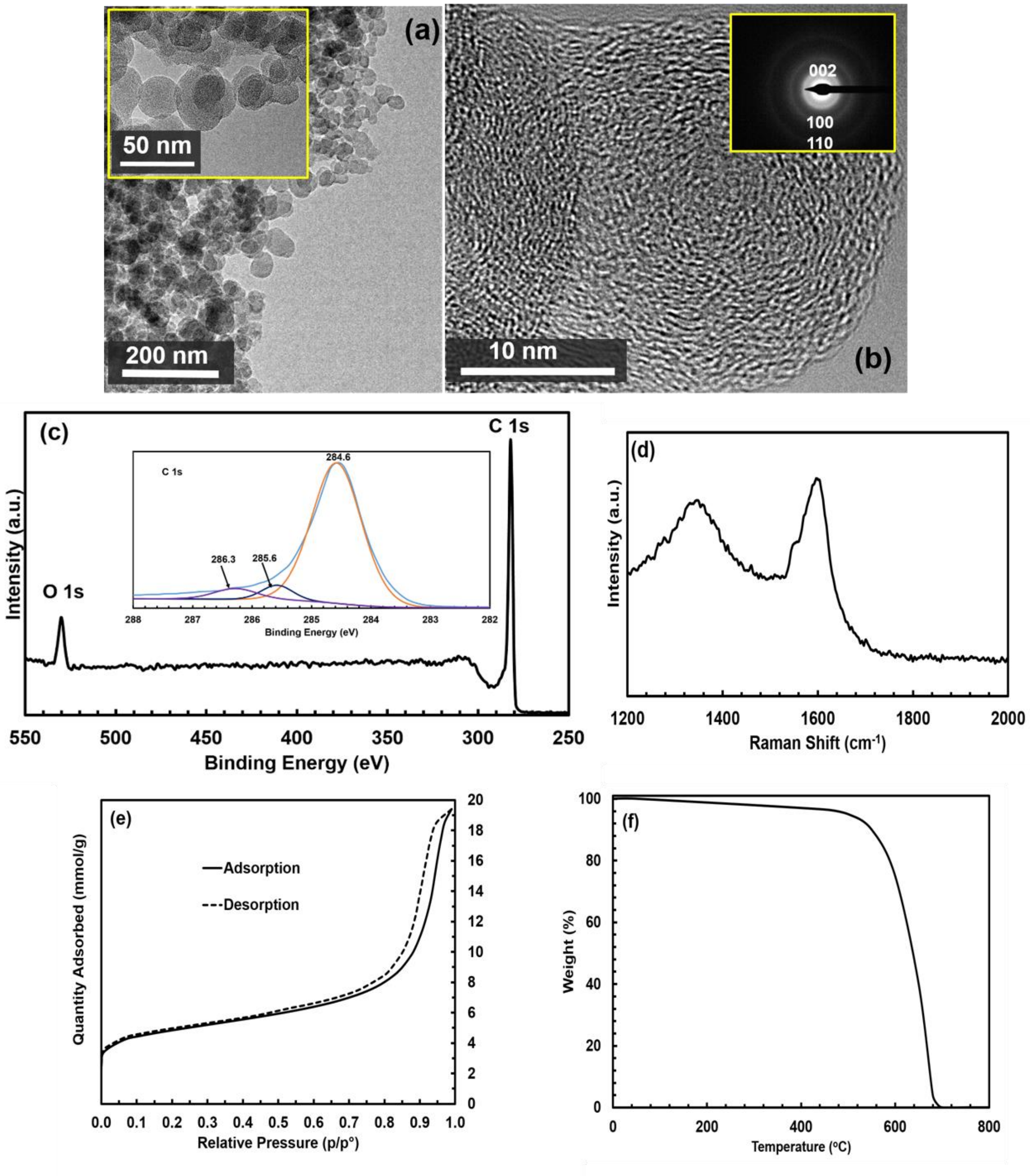

Figure 4 - 1 Characterization of the prepared Candle soot. (a) TEM images with higher magnification (inset). The candle soot dispersion consists of a large number of nanospheres in the size range of 20 to 50 nm (b) High resolution TEM image of the candle soot and its SAED pattern (inset). It indicates the presence of few pieces of crystalline carbon nanospheres in candle soot along with amorphous carbon, which is further confirmed by Selected Area Electron (c) XPS spectrum. It indicates that the candle soot consists mostly of carbon nanoparticles. The inset in the figure shows the deconvolution of C1s peak (d) Raman shift of the candle soot. The peak at 1350 cm-1 (D bands) accounts for the amorphous carbon and the one at 1580 cm^{-1} (G bands) corresponds to E2g mode of graphite due to the vibration of sp2-bonded carbon atoms in a 2D hexagonal lattice (e) Surface Area analysis of the candle soot. It is mesoporous material with an average pore size of 7 nm and a BET surface area of 366 m2g-1. (f) Thermogravimetric analysis of the candle soot. The weight loss of the candle soot is less than 3.5 % up to the temperature of 450 °C.

4.1.2 Spray-based Textured Surfaces

Water repellent superhydrophobic surfaces have found its place in many vital applications, such as oil-water separation[71, 72], corrosion prevention[73,74], self-cleaning glass windows[76] and windscreens designs[76] and hence received tremendous attention both in academia and industry. Superhydrophobicity of a surface is characterized by the high water contact angle (above 150^o) and low sliding angle (below 10^o) [16, 76, 77], and two underlying factors that results in the realization of such surfaces are low surface energy and micron-to-nanoscale hierarchical surface roughness[77- 79]. Many deposition methods such as sol-gel processing[80], chemical vapor deposition[80], laser ablation[81], [82] and radio frequency plasma etching[83] have been used for the fabrication of superhydrophobic surfaces. While these approaches have yielded the expected results, their complexity, huge power requirement and cost associated with the materials present a main challenge for the fabrication of low-cost superhydrophobic surfaces on a large scale. Candle soot, an inexpensive carbon material with promising morphology has been demonstrated as a material suitable for fabrication of superhydrophobic surfaces. However, further modification is required before it can be suitably used for fabrication superhydrophobic surfaces because the particle- particle in candle soot is physical and also weak[83-89]. To this end, Seo et al[84] prepared a superhydrophobic surface from candle soot using paraffin wax as binder to strengthen the interactions between the soot particles. Bayer et al. [89] synthesized durable superhydrophobic surfaces including flexible substrates using flame from a butane burner in conjunction with triboelectric particle deposition process. In addition, Esmeryan et. al.[87], used soot from rapeseed oil in combination with a specially-designed cone-shaped aluminum chimney to achieve superhydrophobic surface without the use of further chemical treatment. So far, significant progress has been made in terms of simplified fabrication technique for soot-based superhydrophobic surfaces. The interest to further explore novel, simple and inexpensive method for fabricating superhydrophobic surfaces is still very attractive.

In this work, a low cost facile approach for the fabrication of stable superhydrophobic surfaces by simple spraying of candle soot dispersion on the surfaces was adopted. The surface morphologies, wettability, resistance to drop impact/water jet impingement and thermal stability of the superhydrophobic surfaces, fabricated by the spray coating method is illustrated in **Fig. 4-2** by comparing these characteristics for the superhydrophobic surfaces fabricated by direct candle flame soot deposition. From the contact angle snapshots shown in insets of **Fig. 4-2-a** and **Fig. 4-2-b,** it is quite clear that the surfaces fabricated by both the techniques (direct candle flame soot deposition and spray coating) are superhydrophobic with high static water contact of $163^{o} \pm 2$ and very low sliding contact angle less than 2^{o}. Although, the candle based coating is more suitable to coat all surfaces including polymeric substrate, the surfaces fabricated by this method lose its superhydrophobicity by the impact of water droplets due to the fragile interaction between the surface and carbon nanoparticles[83, 84].

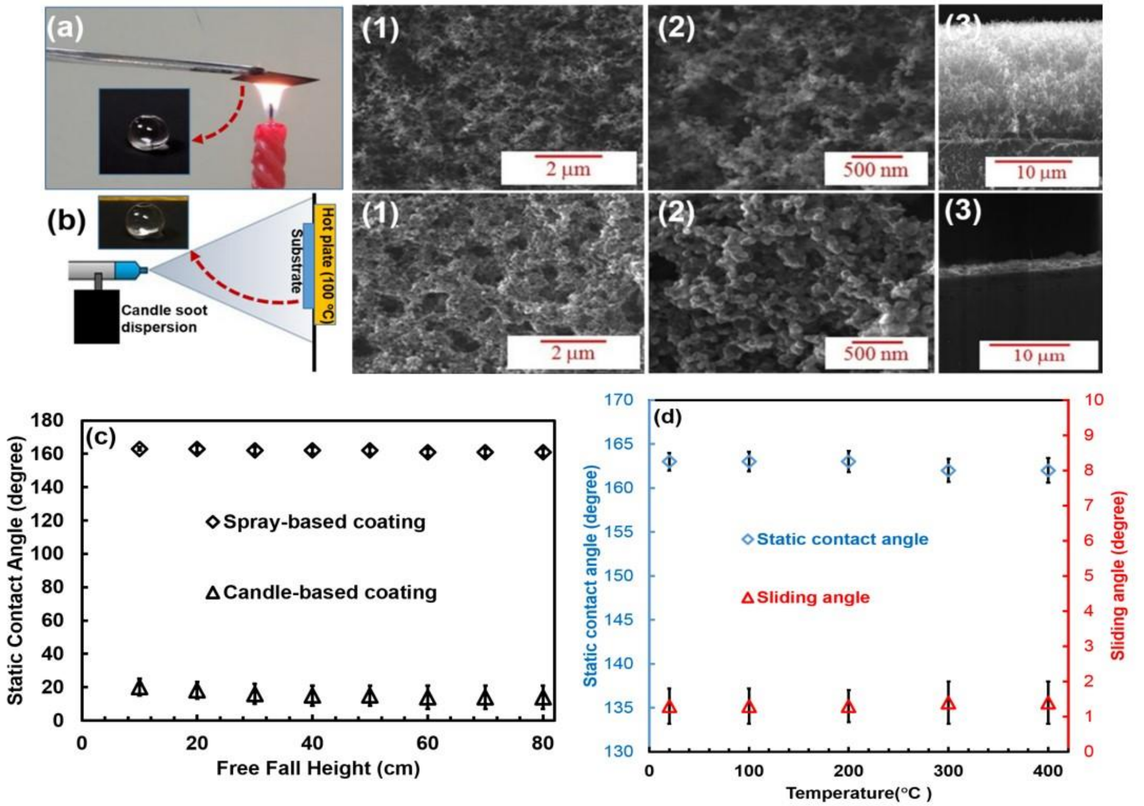

Figure 4 - 2 Fabrication of superhydrophobic surfaces using candle soot dispersions. (a) Direct candle flame soot deposition. (a-1 and 2) FE-SEM images of the surfaces prepared by direct candle flame soot deposition with different magnifications, (a-3) Cross sectional view of the surfaces prepared by direct candle flame soot deposition. (b) Spray coating method. (b-1 and 2) FE-SEM images of spray based coatings with different magnifications and (b-3) cross sectional view of spray based coatings. It shows the compact nature of this coating. (c) Robustness test of both surfaces. (d) Thermal stability test of spray-based coating. Both surfaces (candle-based coating and spray-based coating) are superhydrophobic with high static water contact of 163o ± 2 and very low sliding contact angle less than 2o. The surfaces fabricated by the candle-based coating loses its superhydrophobicity by the impact of water droplets, whereas the spray-based surface is very robust under the same test.

Fig. 4-2-a 1 and 2 and **Fig. 4-2-b 1 and 2** show the FE-SEM images of superhydrophobic surfaces fabricated by direct candle flame soot deposition and spray coating respectively, where we can notice that both surfaces reveal the patterns of irregular nanoparticle network with micron-to-nanoscale surface roughness, the condition necessary for superhydrophobicity. However, it is clear from the cross-sectional views of SEM images shown in **Fig. 4-2-a-3 and Fig. 4-2-b-3,** the thicknesses of surfaces by direct candle flame soot deposition and spray coating-based method are ~ 15 µm and ~ 3 µm respectively and also the spray coating-based surface shows hierarchical and compact nature.

The drop impact resistance of the surface fabricated by direct candle flame soot deposition and spray coating method were tested by observing its ability to retain static contact angles after striking the surfaces by water droplets from a certain height and these results are depicted in Fig. 3c. When 1000 drops of water were allowed to fall on the surfaces from varying heights from 10 cm to 80 cm, the static contact angle of the surface fabricated by direct candle flame soot deposition dropped from 163 ^{o} to 20 ^{o} when the water drops fell from the height as low as 10 cm, indicating that the surface lost its superhydrophobicity, whereas in the case of the spray coated surfaces, the static contact angle remained intact at 163 ^{o} even when the water drops fell from the height of 80 cm. This clearly proves the outstanding resistance to drop impact of superhydrophobic surfaces fabricated by spray coating -based method as compare to one made by direct candle flame soot deposition. The water jet resistance of the spray coating-based surface is demonstrated in supplementary videos S1 and S2, where we can notice that superhydrophobic surface fabricated by direct candle flame soot deposition was destroyed on application of water jet, while the spray coating-based surface clearly endures the impacts and still exhibit superhydrophobic properties under same stream of water jet. This observation can be attributed to the higher compactness of the spray coating-based surfaces as revealed from the SEM studies.

The thermal stability of the spray coating-based surface was tested by examining its ability to retain its superhydrophobicity after annealing the surface in the temperature range of 100-400^{o} C. It is quite clear from **Fig. 4-2-d** that both the static contact angle and the sliding angles remains at their initial values even after annealing the surface at a temperature of 400^{o} C, indicating that the superhydrophobicity is intact and the surface is thermally stable at a temperature as high as 400^{o}C. The thermal stability of the spray coating-based surface was further confirmed with thermogravimetric studies as described earlier. All these studies testify that the spray coating -based surface shows better resistance to drop impact/ water jet impingement and thermal stability than superhydrophobic surfaces fabricated by direct candle flame soot deposition.

4.2 Oxide-modified Metallic Texture Surfaces

According to Wenzel and Cassie Baxter equations, the surface energy and the surface roughness are the two important factors to contend with in the process of engineering a surface of desired wettability. Static contact angle and sliding angle are the key experimental parameters that characterize the wettability of the surface[25, 28, 30]. Higher the contact angle, lower the affinity of the liquid on the surface and vice versa. The surface energy of the material is a necessary but not a sufficient factor to decide the wettability, as the surfaces with certain surface energies may not yield the expected contact angle. Hence, the second factor, the surface roughness and according to Wenzel equation, if a surface is hydrophilic by virtue of its surface energy, it becomes more hydrophilic and on the other hand if a surface is hydrophobic by virtue of its surface energy, and it becomes more hydrophobic by the introduction of surface roughness[28, 30]. Coating the surface with a material of certain surface energy and surface roughness is one way of achieving the desired wettability which is widely found in literature and as mentioned earlier, it is also possible to modify the wettability of a surface by simply introducing a hierarchical surface roughness[33]. In compliance with the Wenzel, Cassie and Young−Dupré formulas, the surface, which is inherently hydrophillic in air, can be made as in-air superhydrophilic and underwater superoleophobic with the introduction of appropriate surface roughness [33]. Superhydrophilic and underwater-superoleophobic textured membranes are considered as water-passing membrane that can separate oil-water mixtures under gravity (i.e., without applying external energy). This is because a denser phase (water) is allowed to permeate through the membrane while a lighter phase (oil) is repelled from the membrane surface. Despite high separation efficiency, anti-fouling property and low energy consumption during separation operation, it can be limited by inability to degrade the water-soluble organic pollutants present in the permeate (e.g., water-rich permeate). Thus, photocatalytic materials such as TiO_2 has been applied in the separation membranes in order to degrade water-soluble organic pollutants in the water-rich permeate (i.e. to fabricate multifunctional membrane for oil-water separation and simultaneous photo-degradation of water-soluble organic pollutants present in the water-rich permeate) [11, 12, 14, 90]. Although a few methods have been developed to fabricate under-water superoleophobic-photocatalytic textured multifunctional membranes, these methods typically involve expensive equipment, environmental hazards, or multi-step processes. Furthermore, the wide band gap of most of these materials (> 3.2 eV which is located in the UV region of the spectrum) limits the large-scale application of such material under solar light irradiation (i.e. UV spectrum is only 5 % of the solar spectrum)[36, 38- 40].

In this work, we developed a universal, scalable, solvent-free, one-step methodology based on thermal annealing of stainless steel membrane to create appropriate surface texture and simultaneously modify its surface energy (i.e, chemical composition, Fe_2O_3 and/or Fe_2O_3-based composites). The crucial surface roughness and chemical composition on the stainless steel mesh with pore size of 2 micron was introduced by simple annealing of the mesh at the temperatures of 800 °C and 1000 °C in the ambient condition. The annealed membranes are under-water superelophobic-photocatalytic Fe_2O_3-based textured multifunctional membranes that can be used for oil-water separation and simultaneous photodegradation of organic pollutants in the water-rich permeate upon visible light illumination (i.e. water-passing multifunctional membrane). It is worth to mention that Iron oxide (Fe_2O_3) and Fe_2O_3-based composite are particularly interesting semiconductor photocatalysts with a visible-light responsive band gap ∼2-2.3 eV[91- 98]. This method of fabrication is not only rapid, simple, and cost-effective but also the annealed membranes show an excellent water affinity, strong underwater-oil repellency as gravity-driven oil-water separators with separation efficiency of 99.9 % as well as excellent photocatalytic activity under visible light illumination

When a liquid drop comes in contact with the solid surface of high surface energy, then the liquid tends to spread on the surface and this hydrophilic property of the surface is more pronounced if the surface is adequately roughened. Hence superhydrophilic surfaces can be fabricated by introducing appropriate surface texture on the surfaces of high solid surface energy (typically, solid-air interfacial tensions $\gamma_{sa} > 72\ \mathrm{mNm^{-1}}$). **Figure 4-3** shows a schematic illustration of fabrication procedure and application of the annealed membranes. 316L stainless steel membranes were annealed at two different temperatures 800 and 1000 ^{o}C in the ambient conditions in order to create appropriate surface texture. In addition to this, annealing at this temperatures helps for simultaneous formation of the oxides of the elements present in the stainless steel alloy, particularly Fe_2O_3 and/or Fe_2O_3 based composites. The change in the surface texture and the formation of oxides by simple annealing transforms 316L stainless steel mesh into a multifunctional membrane in the oily wastewater remediation process, where the membrane with the favorable wettability functions as a medium for water-passing oil water separation (due to its improved surface texture) and also a visible-light responsive photo-catalyst (due to the formation Fe_2O_3 and/or Fe_2O_3 based composites) to simultaneously degrade water-soluble pollutants in the filtered water by photo-catalytic process. Also the formation of Fe_2O_3 and/or Fe_2O_3 based composites on the membrane surface ensures the applicability of this membrane in the abundant visible spectral region of solar radiation. **Figure 4-3** also shows the schematic for

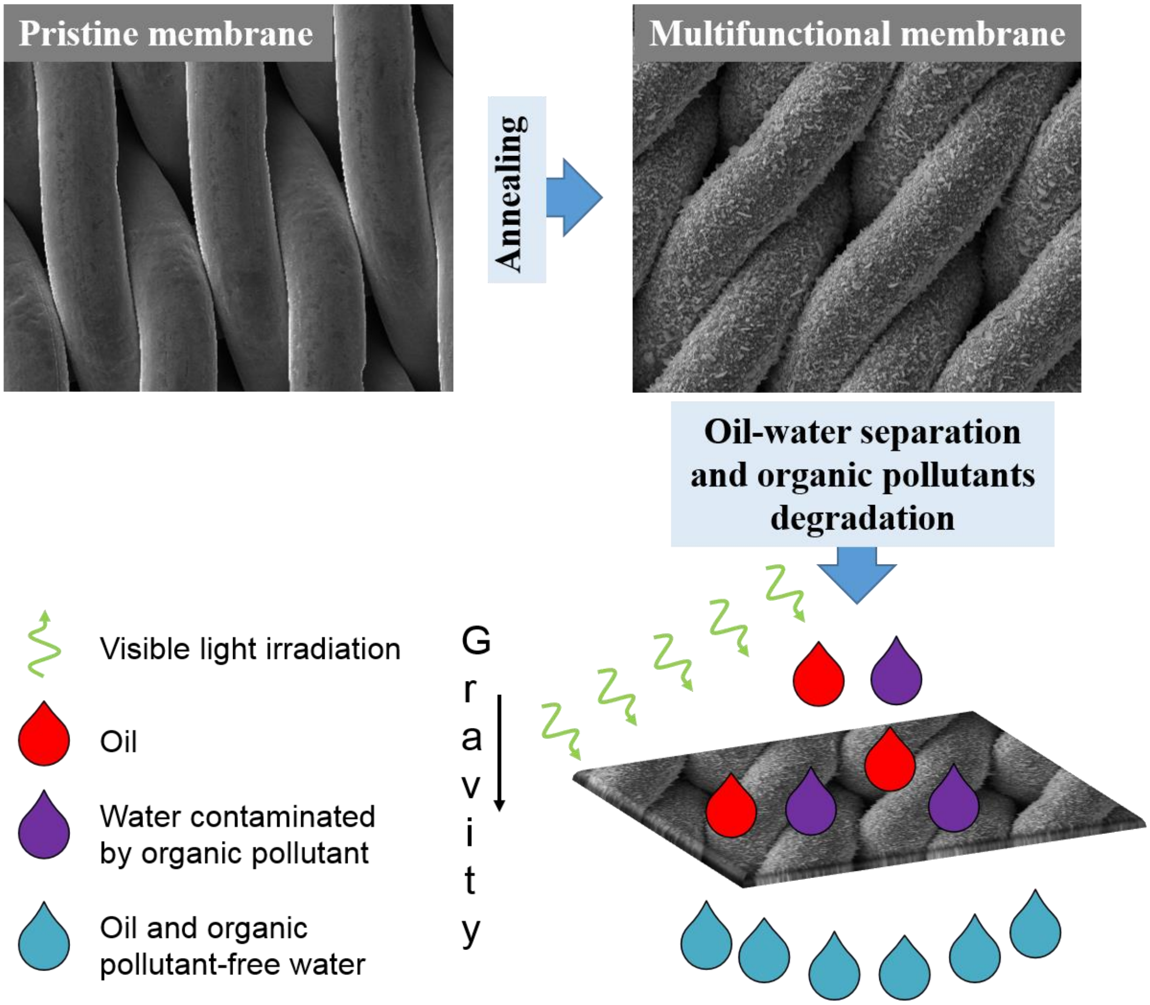

Figure 4 - 3 A schematic illustration of fabrication procedure and application of the annealed membranes.

the simultaneous process of gravity driven oil water separation and photo-catalytic degradation of water-soluble pollutants to yield oil and organic pollutant free water. FE-SEM images shown in **Figures 4-3 to 4-10** (a, b and c) with different magnifications are for the pristine membrane (PM), for the membranes annealed at 800 °C and at 1000 °C respectively. The FE-SEM images for the pristine membrane (**Figure 4-3a**) shows a quite smooth surface even at the highest magnification, which is quite typical. On the other hand, the FE-SEM images of the stainless steel membranes annealed at 800 °C and 1000 °C shown respectively in **Figures 4-3b and c** indicate the annealing temperature dependent surface roughness and structures. The progressive variation of the surface roughness structures between **Figure 4-3b and c** is quite evident even in the medium magnification of the images and at the highest magnification. The stainless steel membrane annealed at 1000 °C clearly exhibits 3D cube-like nanostructures aligned in the same direction with the increased surface area. The elemental composition of the membranes before and after annealing were studied using XPS. Before the analysis, the samples were Ar-sputtered (60 s, 2 kV) to remove the contaminations from the surface. The spectra shown in **Figure 4-11a, b and c** indicated the presence of Cr, Ni, Fe and Mn pertained to the elemental composition of 316L stainless steel alloy and also we can notice that the oxygen content on the membrane surface rose from 7.63 % in pristine membrane to 53.04% in 800 °C annealed membrane and 52.37 % in 1000 °C annealed membrane. Upon visible inspection, the stainless steel membranes annealed at two different temperatures show two different colors with respect to that of the pristine membrane, which indicates that the annealing brought about different chemical composition on the membrane surface as you see in the insets of **Figure 4-11**. So it can be inferred that the excessive oxygen on the surface of the

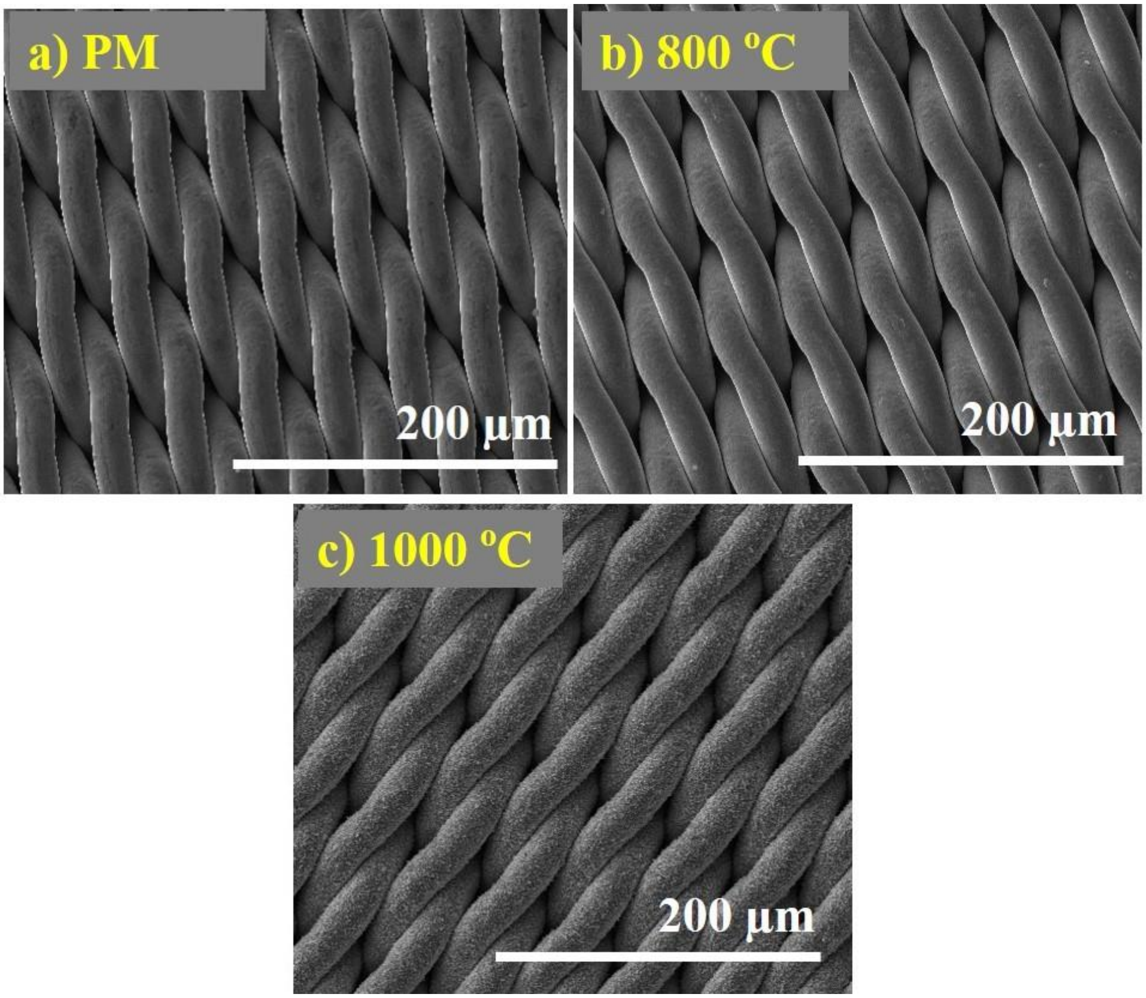

Figure 4 - 4 FE-SEM images of the pristine membrane (PM) and the membranes annealed at 800 °C and at 1000 °C as indicated.

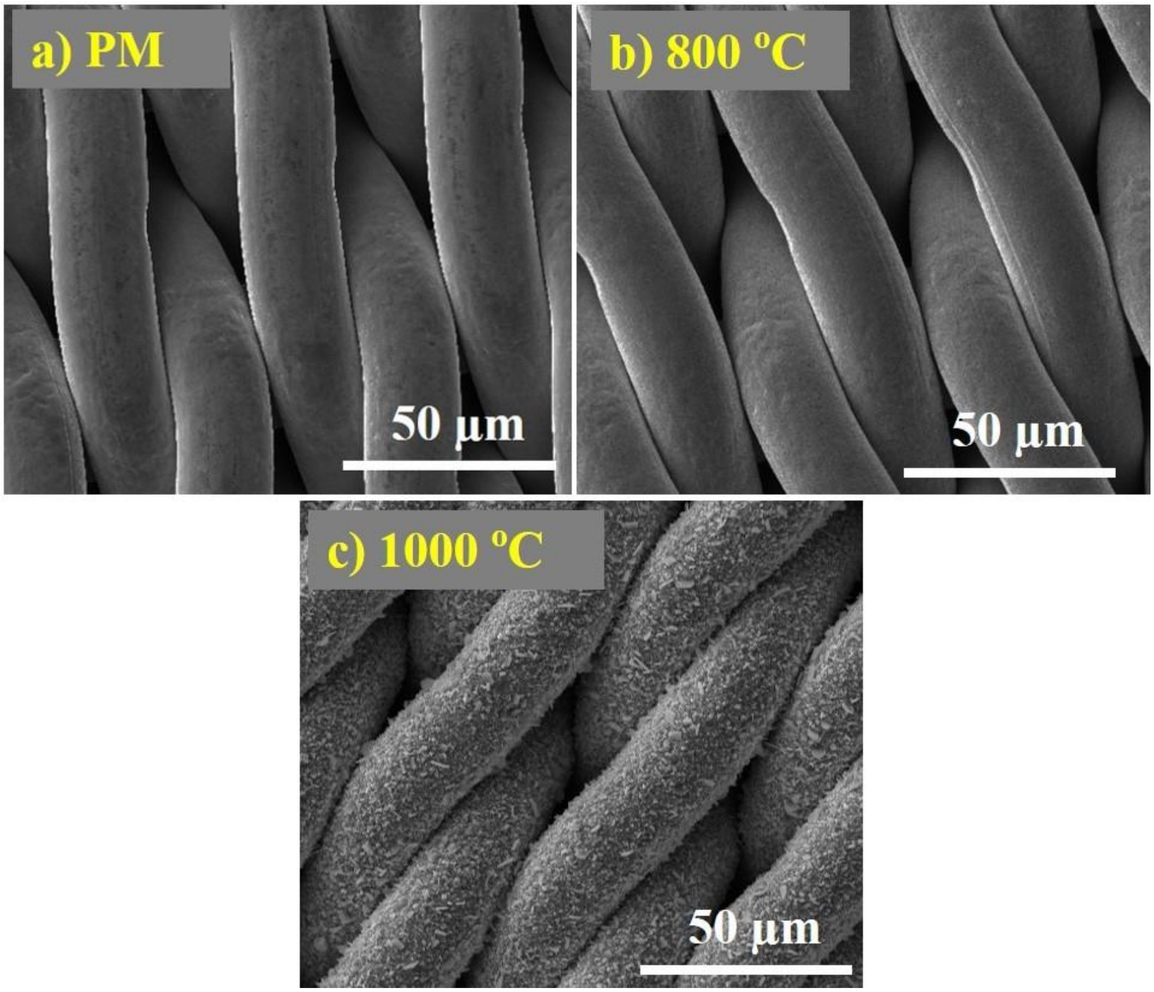

Figure 4 - 5 FE-SEM images at higher magnification of the pristine membrane (PM) and the membranes annealed at 800 °C and at 1000 °C as indicated.

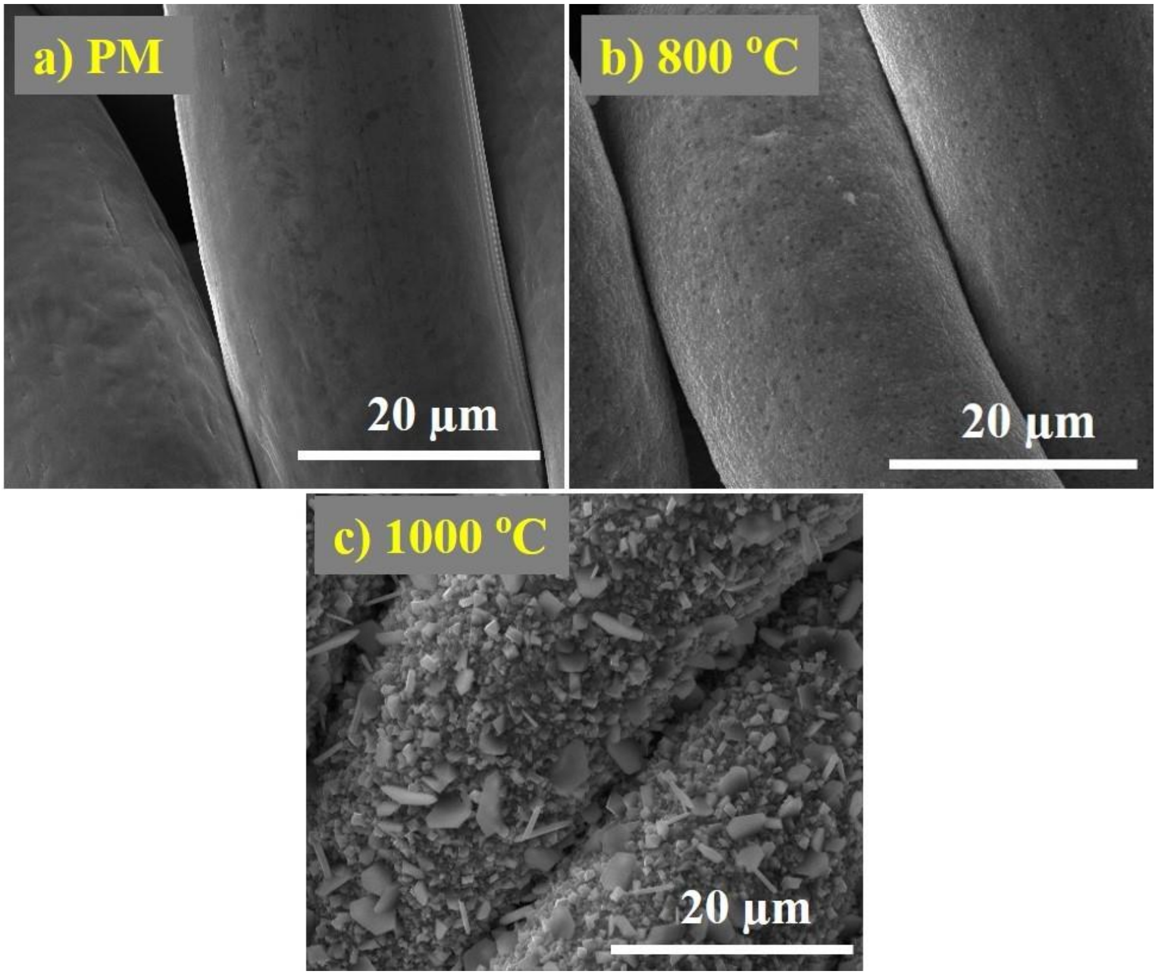

Figure 4 - 6 FE-SEM images at higher magnification of the pristine membrane (PM) and the membranes annealed at 800 °C and at 1000 °C as indicated.

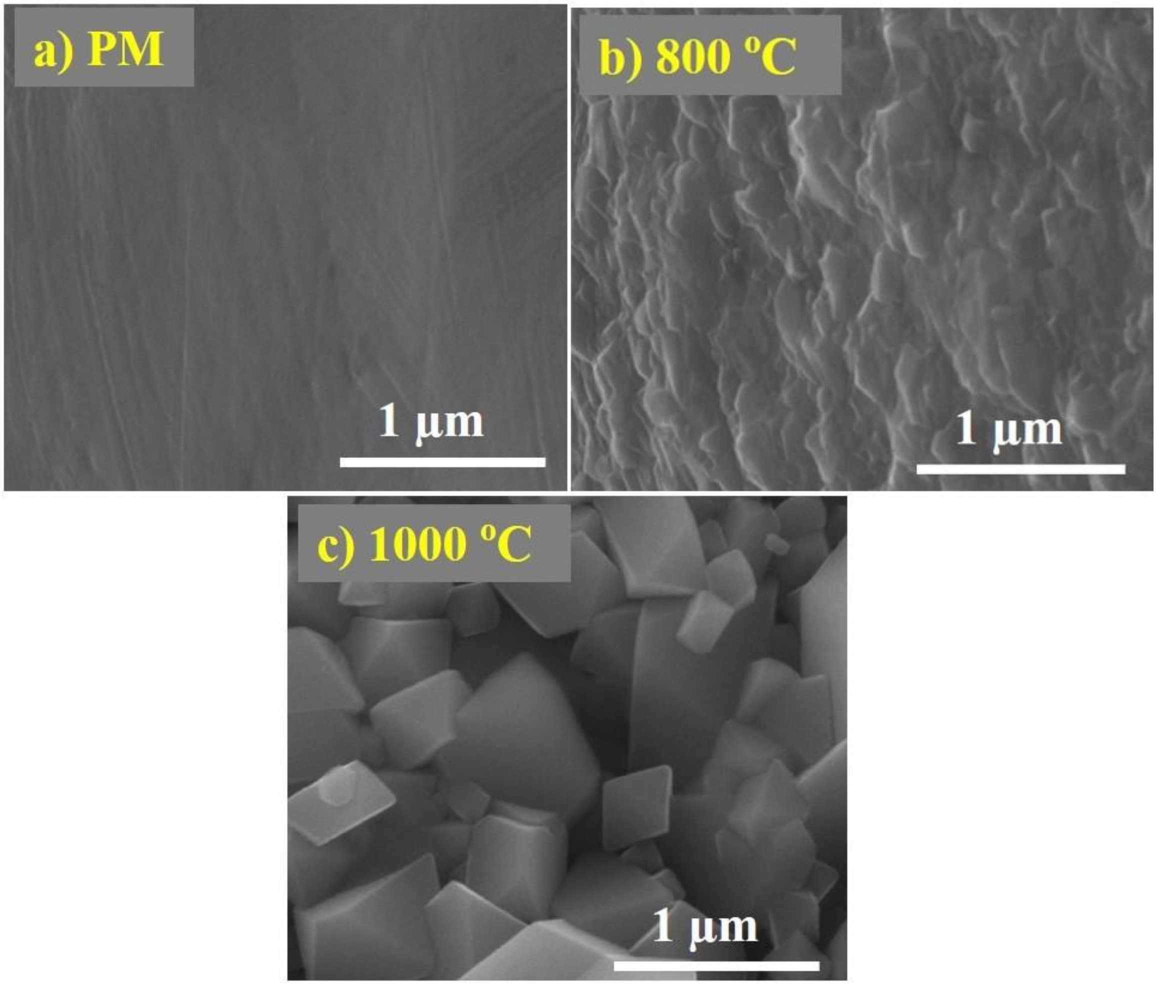

Figure 4 - 7 FE-SEM images at higher magnification of the pristine membrane (PM) and the membranes annealed at 800 °C and at 1000 °C as indicated.

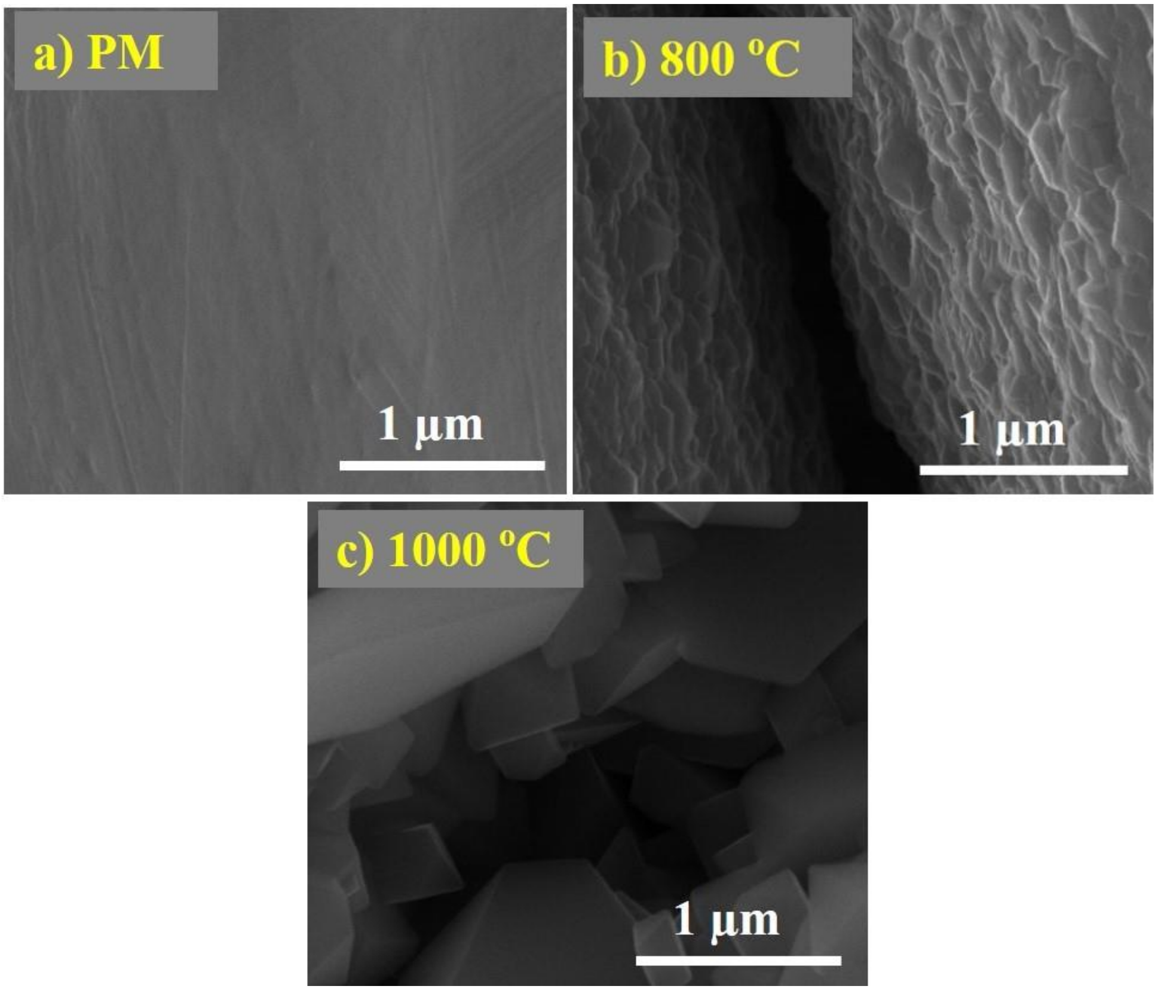

Figure 4 - 8 FE-SEM images at higher magnification of the pristine membrane (PM) and the membranes annealed at 800 °C and at 1000 °C as indicated.

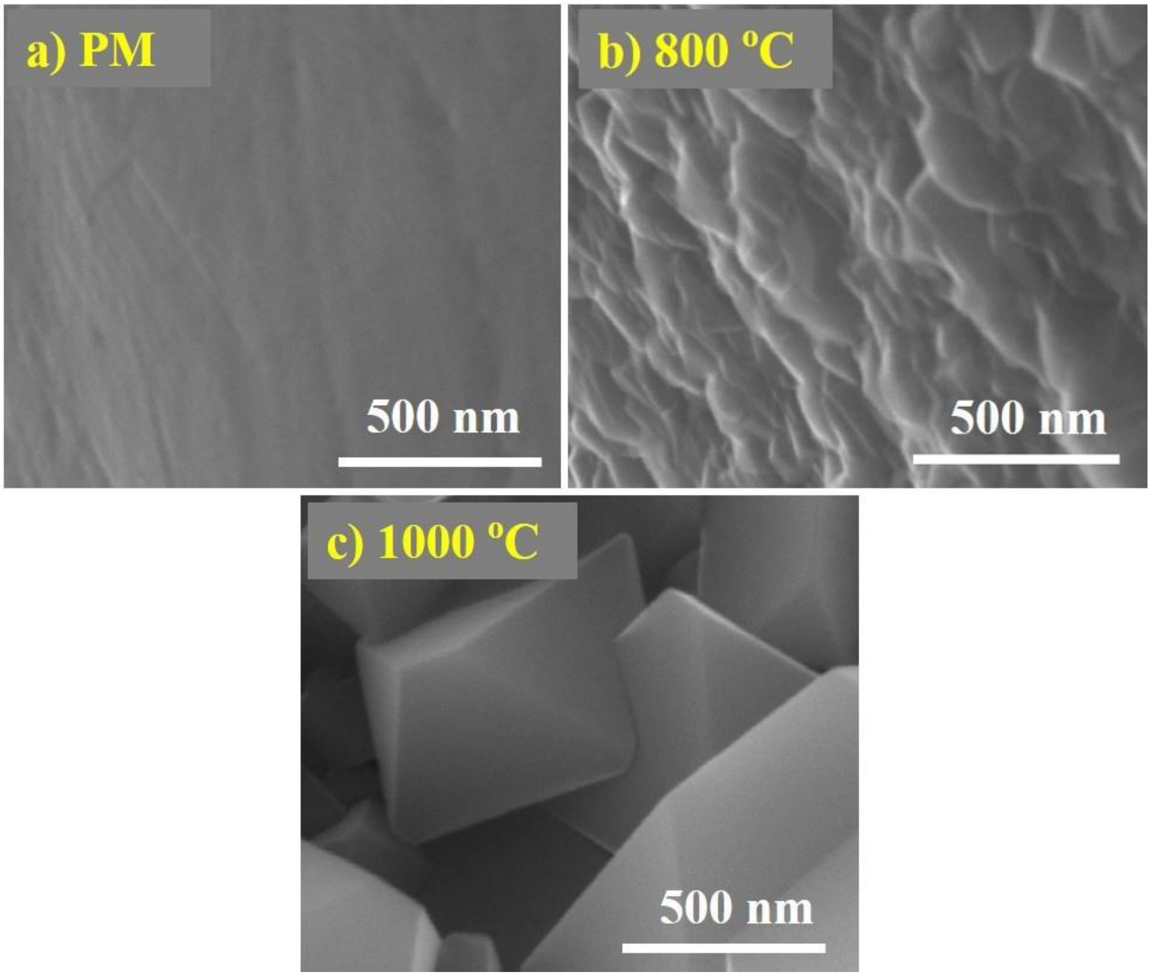

Figure 4 - 9 FE-SEM images at higher magnification of the pristine membrane (PM) and the membranes annealed at 800 °C and at 1000 °C as indicated.

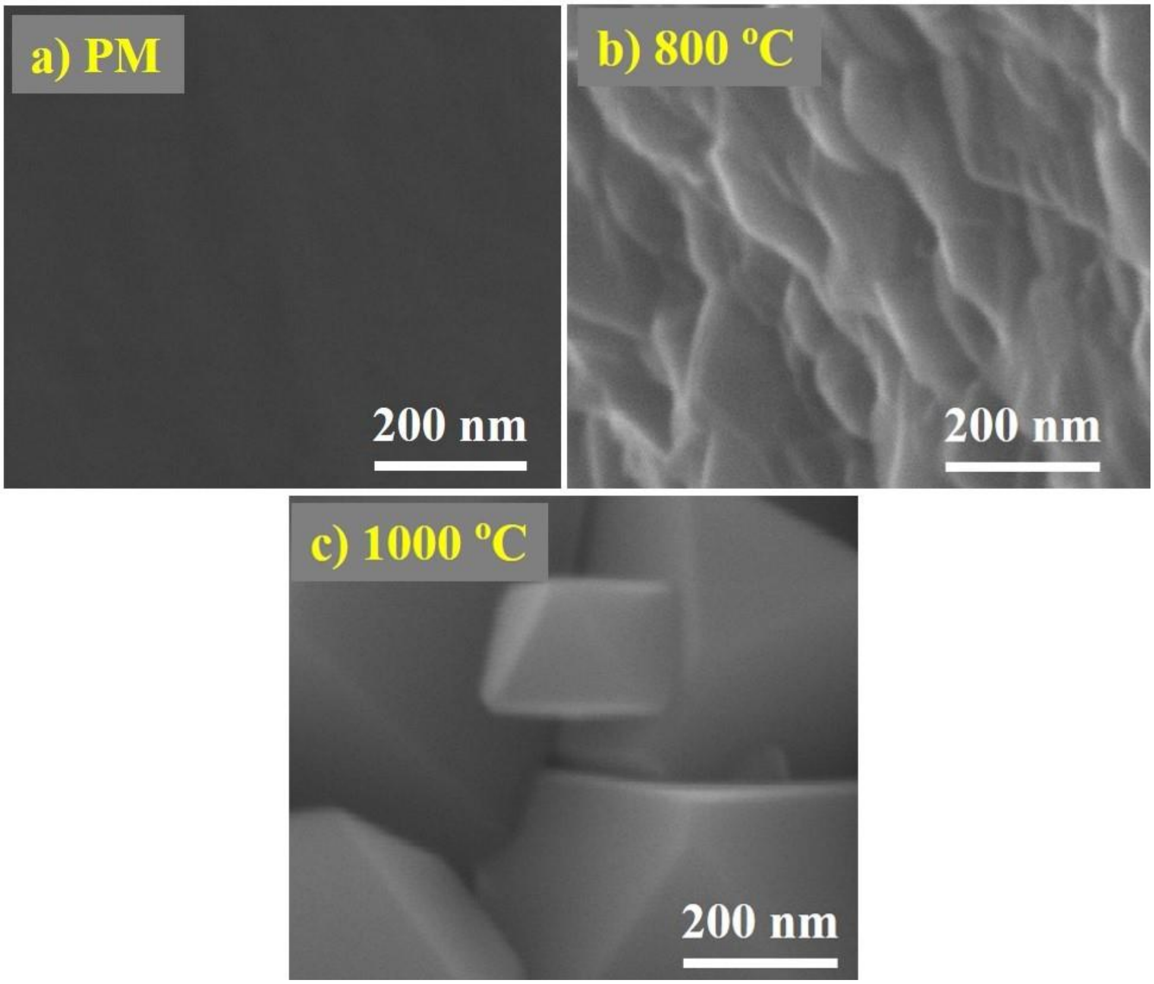

Figure 4 - 10 FE-SEM images at higher magnification of the pristine membrane (PM) and the membranes annealed at 800 °C and at 1000 °C as indicated.

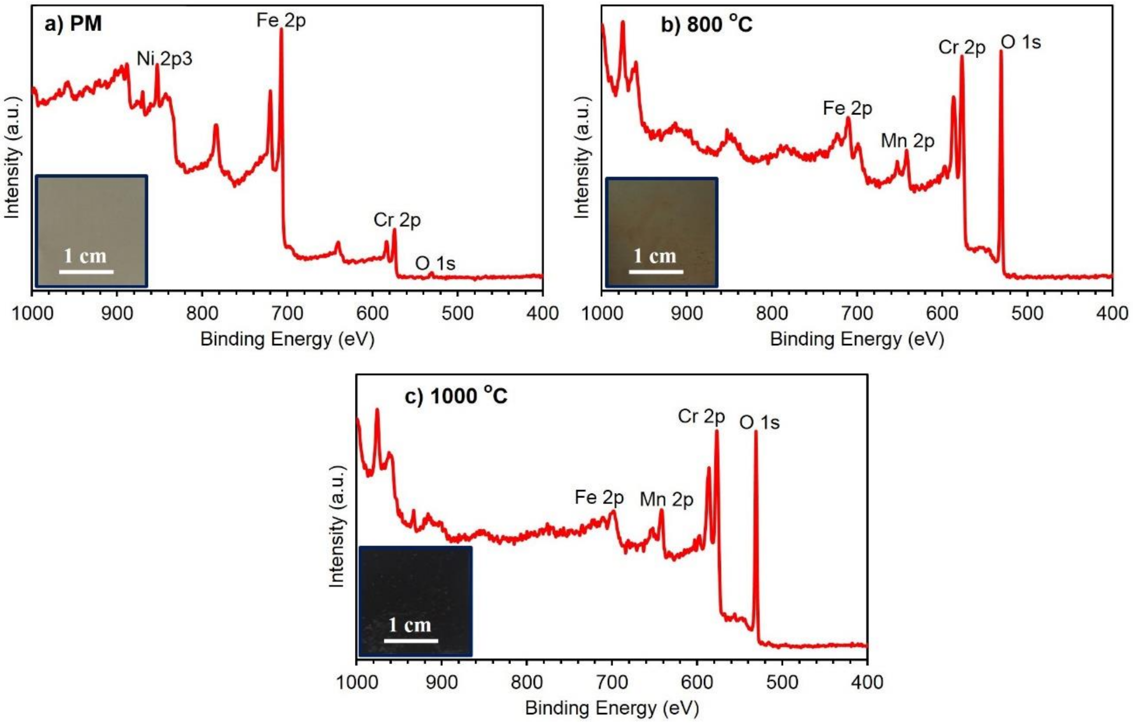

Figure 4 - 11 XPS spectra of the pristine and annealed membranes as indicated. Inset is a photograph to show the color of the pristine and annealed membrane.

annealed membrane emerge from the oxidation of Fe and other metals to form Fe_2O_3 and Fe_2O_3-based nanocomposites. The membrane as such has the pore size of micrometer scale and this in combination with the textured nanostructures brought about by annealing results in the hierarchy of micro and nanostructures on the surface. The contact angle of water on the pristine stainless steel surface in air θ_{wa} is around 86° (hydrophilic) and when the surface roughness is introduced by annealing at 800 °C and 1000° C , The surface became superhydrophilic with the contact angle θ_{wa} close to 0° with slight difference in water affinity as you see in the supplementary videos S 3-5. This superhydrophilicity on the membrane surface is attributed to the high surface energy of Fe_2O_3 and Fe_2O_3-based nanocomposites and the surface roughness generated by annealing. This is one of the wettability conditions of the surface required for the water-passing membrane. **Figure 4-12a** shows the underwater contact angle of oil on the surface (θ_{ow}) along with the sliding angle. Although the static contact angle is the commonly used measure of the wettability of a surface, often it is not sufficient to describe the liquid repellency (hydrophobicity or oleophobicity) or sliding property of the surface. The surface with high static contact angles does not always slide easily from the surface and hence the combination of underwater contact angles and the sliding angles of oil on the surfaces are presented in **Figure 4-12a**. It is quite clear from that the underwater contact angle of oil on the surface (θ_{ow}) increases with the annealing temperature and reached to the highest value of 160° for 1000 °C annealed surface), whereas the sliding angle decreases with the annealing temperature and reached the lowest value

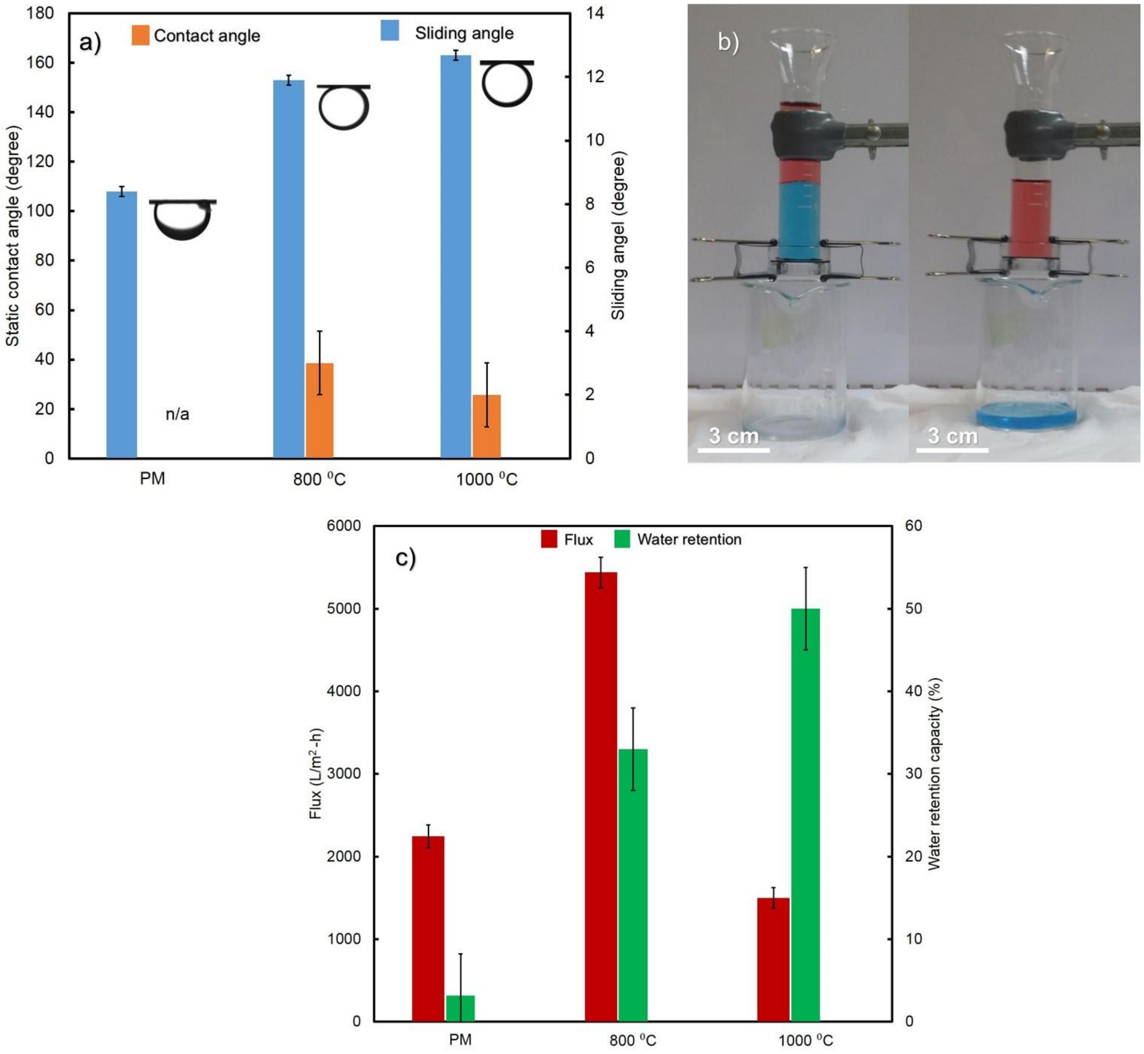

Figure 4 - 12 (a) Wettability, (b) Oil-water separation, and (c) flux and water retention of the pristine and annealed membranes as indicated.

of 2° for 1000 °C annealed surface), indicating that the surface became perfectly underwater superoleophobic (oil repellent). As the annealed stainless steel membrane surfaces possess the required wettability for water passing gravity driven oil water separation and also the photocatalytic characteristics due to the formation of Fe_2O_3 and Fe_2O_3-based nanocomposites, this surface was used for the separation process of hexadecane-water mixtures contaminated with MB dye and degradation of MB dye in water. First, the oil-water separation test was performed by keeping a stainless steel separating membrane in between the two glass tubes and **Figure 4-11b** (video S6 and S7) show the oil water separation process of hexadecane-water mixtures contaminated with MB dye. As expected, with annealed stainless steel in place, when oil water mixture (blue: water and red: oil) was poured into the upper tube, MB contaminated water passed quickly through the separator and into the beaker, whereas the oil phase was effectively blocked by the membrane and remained on the upper tube. However, in the same oil water separation procedure, when annealed membrane was replaced with the pristine stainless steel membrane, the whole mixture of hexadecane and MB dyed water permeated through the membrane altogether, indicating that the pristine membrane is not capable for oil water separation. The thermogravimetric analysis showed that oil- water separation efficiencies for both the annealed membranes were 99.9%.

As shown in **Fig. 4-12c**, the permeation flux with annealed stainless steel membranes at 800 °C and 1000 °C are above 5450 and 1500 L m^{-2} h^{-1} respectively and this is due to the variations of pore size of the membranes set in at different annealing temperatures. The high flux are important in determining the economic viability of membrane separation. **Figure 4-12c** also shows the water retention capacity of the textured membranes, which is the ratio between the weight of trapped water due to pre-wetting process to the weight of the dry membrane, i.e. (weight of the wet membrane – weight of the dry membrane)/ weight of the dry membrane). It is was found that the water retention capacity of the membranes annealed at 800 °C and 1000 °C are 33% and 50 % respectively. This means that these membranes can keep the trapped water required for the oil-water separation for long time as compared to the pristine membrane, which can keep only 3% of its weight. In addition, it indicates that residence time t within the photocatalytic reactor volume is increased and thus means higher degradation efficiency according to the Langmuir-Hinshelwood kinetic model. This increased water retention capacity is due to the water-favoring property of Fe_2O_3 and Fe_2O_3-based composites grown on the annealed membranes. Thus by simple annealing, we can enhance the crucial wettability of the membrane surface, required for the oil water separation and also can achieve high flux rate and separation efficiency.

The second favorable attribute brought by annealing process is the formation of Fe_2O_3 and Fe_2O_3-based composites on the membrane surface, which acts as an efficient photocatalyst with different active volumes for the degradation of organic pollutants present in the permeated water in the oil water separation process. The photocatalytic degradation of MB dye was carried out in a separate setup shown in **Figure 4-13a**. Since the band gap energy of Fe_2O_3 is in the visible spectral region, we used a broad band light source (300W halogen lamp with 100 mW cm^{-2} intensity) with a 420 nm cut off filter. The annealed stainless steel membrane (2.3 cm^2) was immersed in 10 ml of MB dye (5 mg L^{-1} dye concentration), which makes a water level only 2 mm above the membrane surface in order to reduce the light attenuation. Before irradiating the sample, this set up was kept in dark for 30 minutes to attain a thorough adsorption–desorption equilibrium. After turning on the light radiation for photo-catalytic degradation process, the irradiated sample was collected at a regular interval and subjected to UV-VIS absorption studies for determining the concentration of the dye. The absorption spectra of MB dye at regular time interval using stainless steel mesh annealed at 800 °C and 1000 °C are shown in **Figure 4-13b and c** respectively and the degradation efficiency with irradiation time for both the meshes are also shown in **Figure 4-13d**. As it is clear from **Figure 4-13d**, after 240 min of visible light irradiation, 20% and 40% of the MB dye from the initial concentration degraded when stainless steel mesh annealed at 800 °C and 1000 °C respectively were used as photocatalyst. The higher degradation of MB dye using the stainless steel membrane annealed at 1000 °C which acted as a photocatalyst is attributed to its 3D-like nanostructure on its surface morphology, and the resulting enhancement in the surface area.

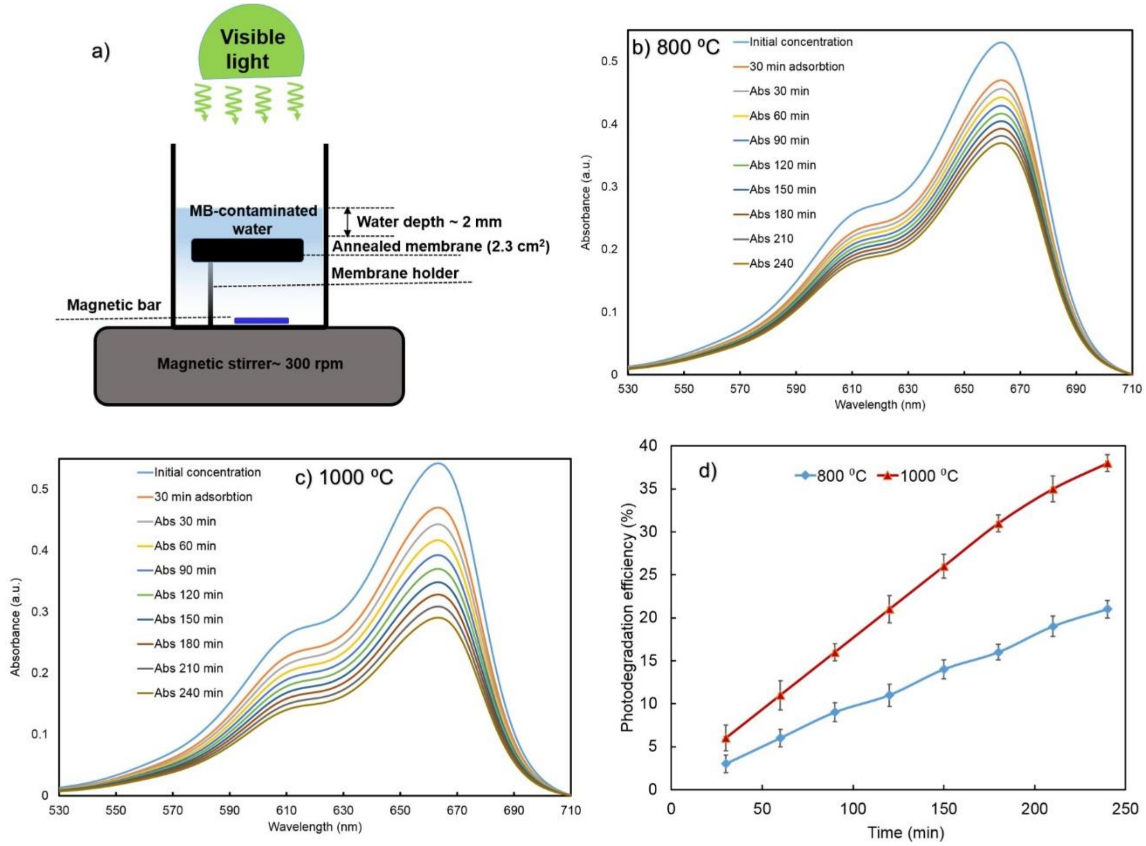

Figure 4 - 13 (a) A schematic diagram of the photocatalytic reactor. (b) and (c) The absorption spectra of MB dye at regular time interval using stainless steel mesh annealed at 800 °C and 1000 °C respectively. (d) The photodegradation efficiency of the annealed membranes at 800 °C and 1000 °C as indicated.

4.3 The Janus Membranes

Membranes with selective wettability of water over oil have received great attention due to their antifouling property and high separation efficiency for all types of oil-water mixtures without the need for pre-wetting with water[16, 17]. Several studies have investigated the development of oil-water separation membranes that are hydrophilic (water contact angle < 90^o) and oleophobic (oil contact angle > 90^o) in air[17, 34, 35, 99]. Such hydrophilic and oleophobic membranes can separate all types of oil-water mixtures (i.e., free oil-water and emulsified oil-in-water or water-in-oil mixtures) under gravity (i.e., without applying external energy)[16]. This is because the denser phase (water) is allowed to permeate through the membrane while the lighter phase (oil) is repelled from the membrane surface. Despite the high separation efficiency and low energy consumption during separation operation, such membranes can be limited by the inability to remove water-soluble organic pollutants present in the permeate (e.g., water-rich phase).

Many other separate studies have also been carried out to investigate the photo-catalytic degradation of organic pollutants [39, 41, 42, 100- 108] using photo-catalytic materials such as titanium dioxide (TiO_2) under ultraviolet (UV) light illumination, which leads to the complete mineralization of most of the organic pollutants in water [38, 39, 41, 42, 44]. Thus, photo-catalytic materials such as TiO_2 have been implemented in separation membranes in order to degrade water-soluble organic pollutants present in the water-rich permeate [12- 14]. However, to the best of our knowledge, there has been no report of a membrane that exhibits selective wettability of water over oil and simultaneous photo-catalytic degradation of water-soluble organic pollutants present in the water-rich permeate. This is because photo-catalytic materials degrade not only the water-soluble organic pollutants but also the organic molecules coated on the membrane to engender desired wettability [13]. Therefore it is required that photo-catalytic materials and the coating materials be separately applied to the membrane in order to engender selective wettability and photo-catalytic degradation of organics. In this work, for the first time, we develop a Janus membrane that exhibits selective wettability of water over oil and simultaneous photocatalytic degradation of water-soluble organic pollutants present in the water-rich permeate. Such a Janus membrane possesses two functional surfaces on either side: superhydrophilic-superoleophobic (water contact angle = 0^o, oil contact angle > 150^o and sliding angle < 10^o) feed-side surface where the feed oil-water mixture is introduced and photocatalytic permeate-side where organic pollutants in the water-rich permeate can be degraded upon UV light illumination. Because the oil-water separation and photocatalysis functions are provided by two separate coatings on different sides of the membrane, our Janus membrane allows for flexibility in the choice of photocatalyst. Other possible photocatalysts that could be used in the permeate-side of our Janus membrane include nitrogen or co-doped metal oxide (TiO_2, ZnO, WO_3) photocatalysis, which are active in the visible spectral region of sunlight [40, 45, 109- 119]. Additionally, by illuminating UV through the bottom of the device rather than through the feed solution, our system is not affected by severe UV attenuation through the turbid feed solution column according to the Beer-Lambert law [121]. We demonstrate that this kind of Janus membrane can degrade organic MB dye present in the water-rich permeate upon UV light illumination. We also developed a mathematical model that enabled us to predict the photo-degradation efficiency during water-rich permeate penetration. Finally, we showed separation of free oil-water, oil-in-water and water-in-oil emulsion and in situ photo-degradation of water-soluble organic pollutes in the water-rich permeate upon UV light illumination.

Figure 4-14 shows the overall procedure of fabricating the Janus membrane and its wettability. We fabricated the Janus membrane using a quick spray-coating method taking less than 20 minutes. The fabrication procedure includes four main steps: (i) a SiO_2/SF-100 dispersion was first sprayed on the feed side of the pores membrane to provide the required roughness and adhesion. (ii) Next, FS-50 solution was immediately sprayed on SiO_2/SF-100 layer as a second layer to provide the required selective wettability for water over oil. Note that FS-50 is a commercial fluoro-surfactant that has been utilized in fabricating superhydrophilic-superoleophobic membrane [100]. Then, we spray coat a TiO_2 nanoparticles dispersion on the permeate side of the membrane. Finally, the fabricated Janus membrane was transferred to an oven operating at 80 °C for 10 minutes in order to evaporate solvents (Boiling point of acetone, THF and ethanol are 56, 66 and 78.37 °C respectively). Henceforth, the feed-side coating of the Janus membrane is labelled as SSF (SiO_2/SF-100/FS-50), the permeate-side coating is labelled as (TiO_2) and their combination is labelled as SSF-TiO_2 (SiO_2/SF-100/FS-50/TiO_2).

To evaluate the wettability of the Janus membrane, we measured the apparent advancing contact angles for water and hexadecane on the feed-side and the permeate-side coatings. In addition to these two surfaces, the apparent advancing contact angles for water and hexadecane on an uncoated membrane was also measured for comparison. The uncoated membrane shows contact angle 0 (θ_{wa} = 0°) for a sessile water drop and contact angle 0 (θ_{oa} = 0°) for a sessile oil drop in an air environment, while the SSF coated membrane is superhydrophilic (θ_{wa} = 0°) and superoleophobic (θ_{oa} = 153$\pm$2° and sliding angle < 5°). This selective wetting behaviour between oil and water on the feed-side of our Janus membrane (Video S8) is attributed to the surface reconfiguration of the perfluorinated alkyl chains in the fluorosurfactant as reported by Sawada et al.[122] and subsequently further explored by others recently.[17, 34, 35]. The superhydrophilic-superoleophobic wetting behaviour of our SSF coated membrane indicates that our membrane has a potential for oil-water separation solely under gravity without the need for pre-wetting [12, 14, 32]. Furthermore, the extreme water wettability (θ_{wa} = 0°) on the permeate side of the TiO_2 coated membrane suggests that the organic pollutant-contaminated water-rich permeate can easily wet the photocatalytic surface, which shall subsequently enhance the photo-catalytic degradation of organic pollutants upon UV light illumination.

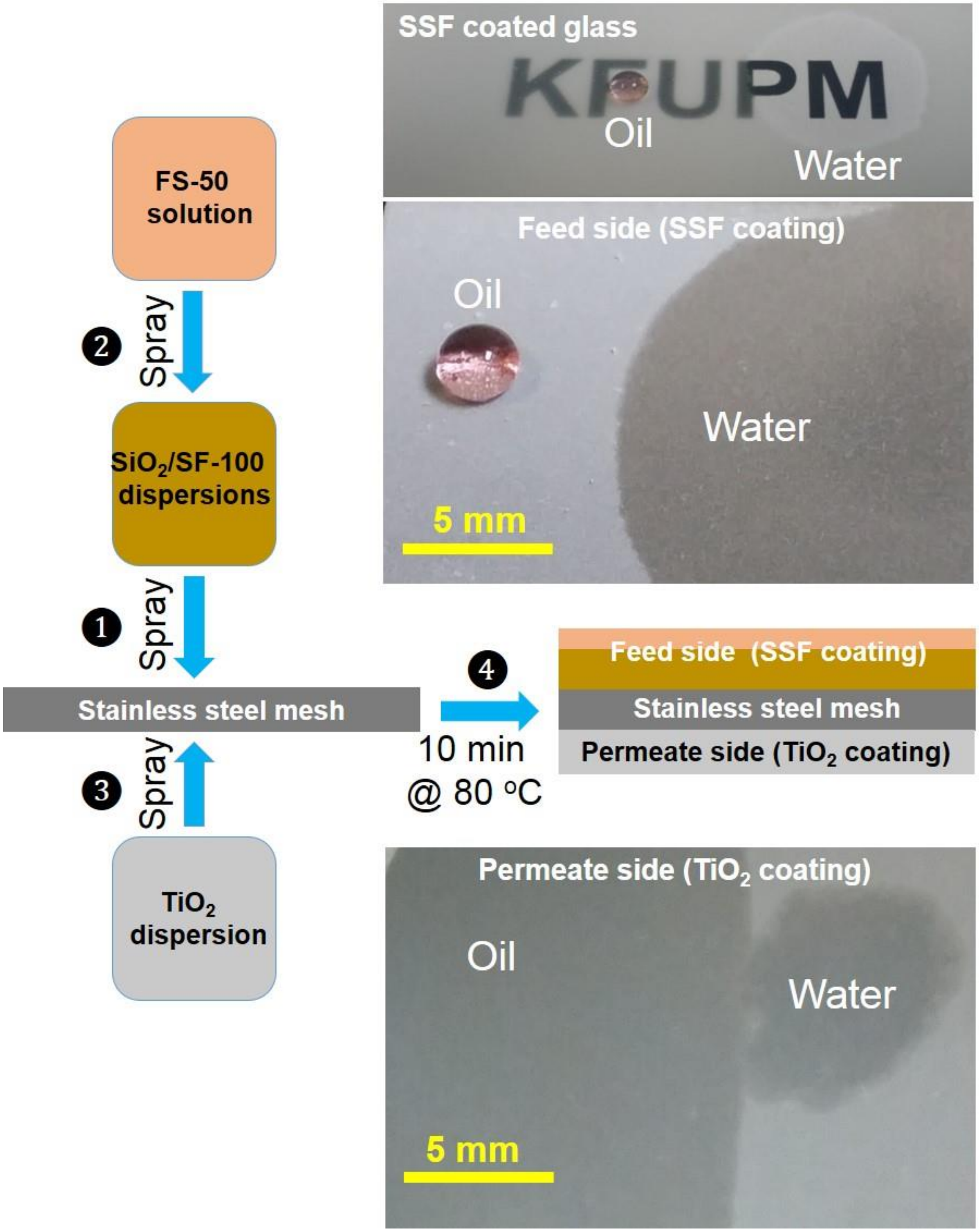

Figure 4 - 14 A schematic illustration of fabrication procedure and wettability. (a) Spray-coating based fabrication, wettability and morphology of the Janus membrane: SiO_2/SF-100 dispersion and FS-50 solution are sequentially sprayed onto the feed side of the membrane (side facing the water to be treated) while a TiO_2 dispersion is sprayed onto the permeate side of the membrane (side facing the treated water). Then, the Janus membrane was annealed at 80 ºC for 10 minutes. Inset photos show water and hexadecane droplets on both sides of the Janus membrane and SSF coated glass to show the transparency of SSF coating.

The simple and facile spray coating method allows for uniform deposition of materials on both sides of the Janus membrane. Also, **Figure 4-15** presents the Field Emission Scanning Electron Microscope (FE-SEM) images of the uncoated membrane, feed-side and the permeate-side coatings. It is quite clear from the FE-SEM images that SiO_2 nanoparticles form a porous structure with micro-nano hierarchical surface roughness attached to the membrane. SiO_2 nanoparticles were added to create hierarchical texture on the surface which is essential for achieving superoleophobicity through a Cassie-Baxter state of wetting[122, 123] as shown in **Fig. 4-16**. It shows the advancing contact angles of uncoated, FS-50 coated, SiO_2 coated, and SiO_2/SF-100/FS-50 (SSF) coated glass by water and hexadecane. The uncoated glass is superhydrophilic-superoleophilic as indicated in **Fig. 4-16-a**. FS-50 coated glass is hydrophilic-oleophobic due to the fluorinated groups inherent in FS-50 which are omniphobic (hydrophobic and oleophobic) but reconfigure in the presence of polar liquids such as water with a small molecular size as depicted in **Fig. 4-16-b**. This wetting behavior holds promise for an enhancement of wettability if SiO_2 nanoparticles are applied before the FS-50 layer. As shown in **Fig. 4-16-c**, the SiO_2 coated surface, like uncoated glass, is also superhydrophilic-superoleophilic. Both FS-50 and the SiO_2 dispersion in acetone have negative zeta potentials [100] indicating the importance of using a strong binder such as SF-100 (which is not soluble in water) to hold both layers together. SSF coated surfaces are superhydrophilic-superoleophilic as depicted in **Fig. 4-16-d**. This result indicates that the wettability of SSF coated glass by oil is in the Cassie-Baxter state while water is in the Wenzel state. SF-100 is a photo (thermal)-curable acrylate which enhances the adhesion of our coating materials to the substrate. **Figure. 4-17** shows the

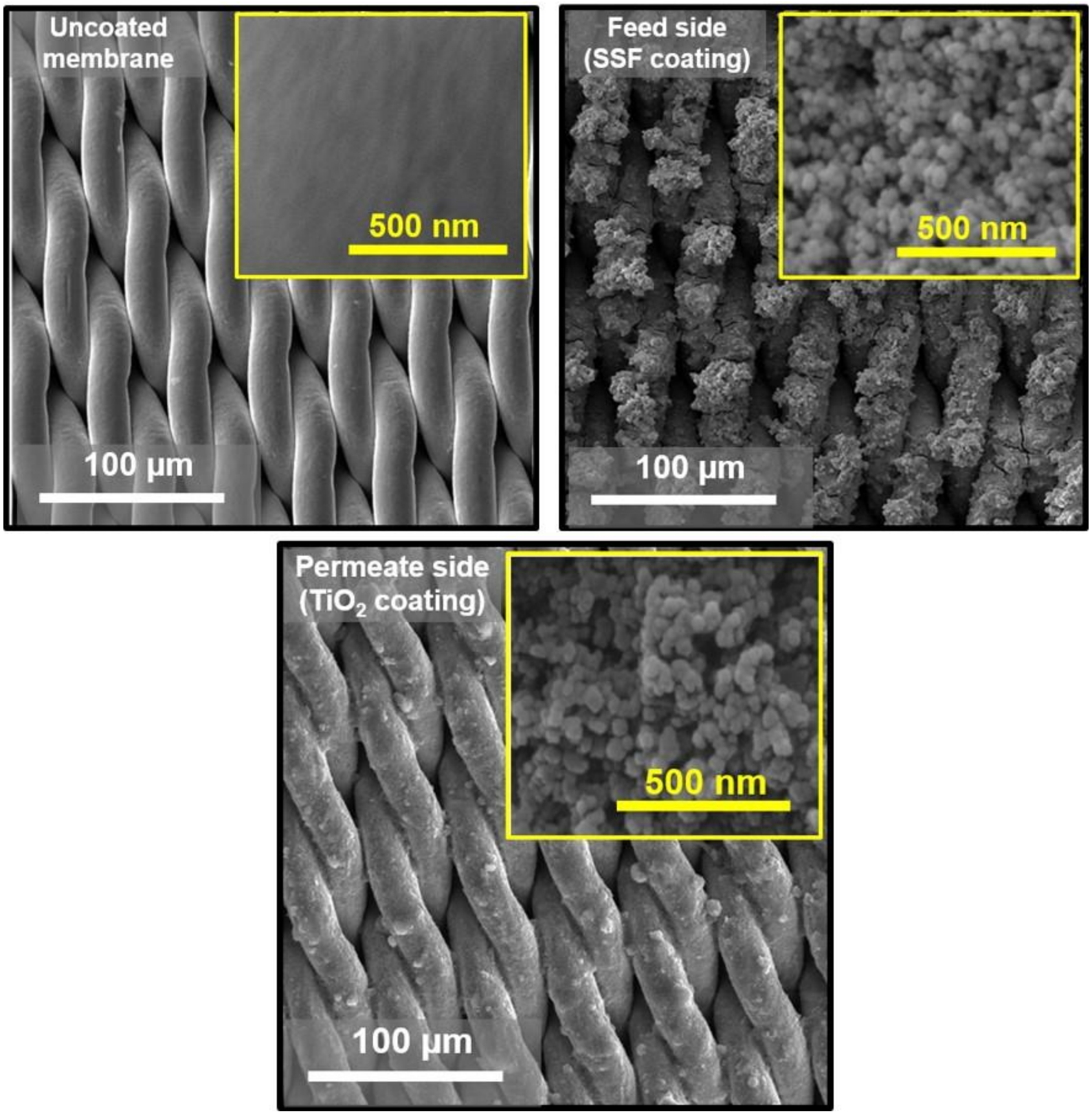

Figure 4 - 15 FE-SEM images of the uncoated membrane, feed-side and the permeate-side coatings at different magnifications as indicated.

improvement of the coating due to using SF-100. The advancing oil contact angle was measured as a function of the number of water jets as shown in the figure. Water jet was applied on SSF and SF (SF-100 free) coatings to study the effect of using SF-100 on the durability the coating. Water jet (20 ml during 4 second for each test) was issued from a spray bottle with a known diameter (1mm). The velocity of the water column and the pressure due to the water jet impingement on the coated surfaces were calculated to be 5.9 ± 0.7 m/s and 17.8 ± 4 kpa respectively. On the other hand, the FE-SEM image of TiO_2 nanoparticles on the permeate-side coating shows the micro-nano hierarchical surface morphology, rendering the essential enhanced surface area necessary for the photo-catalytic degradation of organic pollutants.

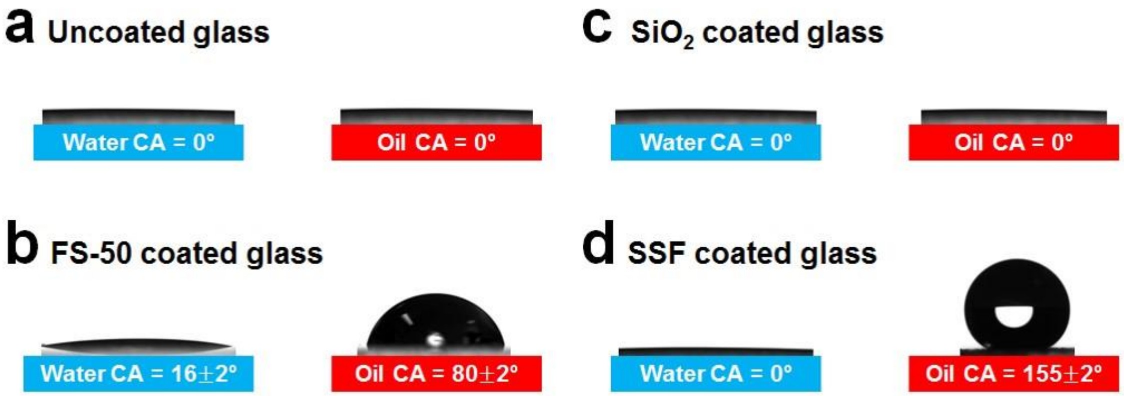

Figure 4 - 16 The advancing contact angles of uncoated, FS-50 coated, SiO_2 coated, and SiO_2/SF-100/FS-50 (SSF) coated glass by water and hexadecane.

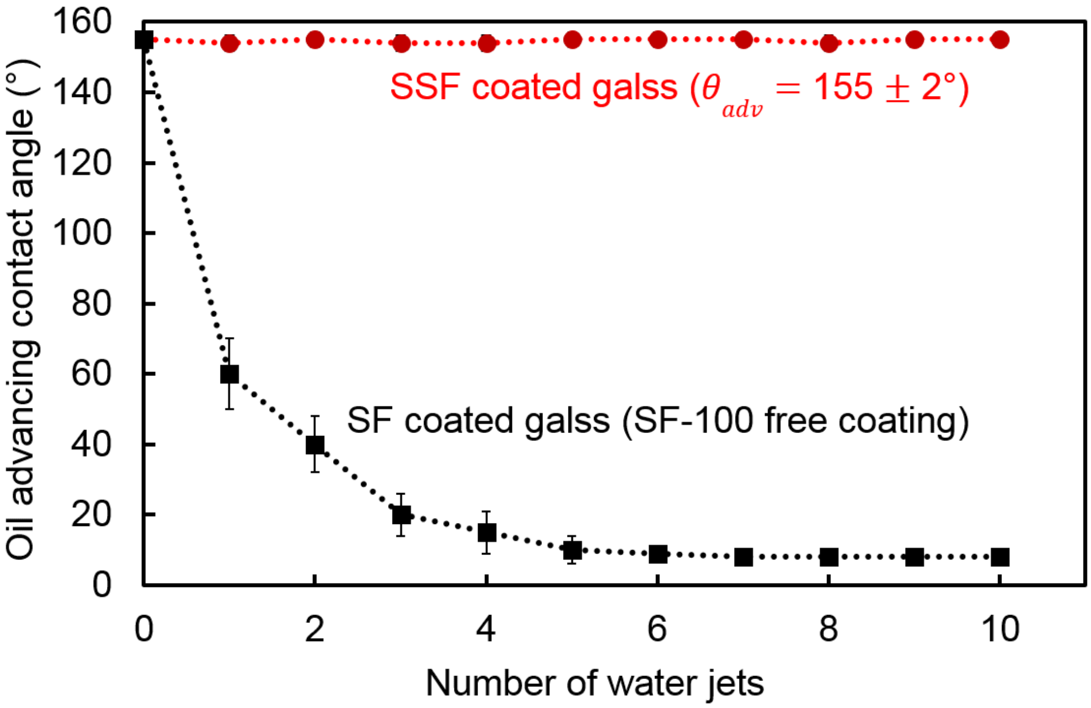

Figure 4 - 17 The improvement of the feed-side coating due to using SF-100.

The robustness of SSF and TiO_2 coated sides were carried out by observing the advancing oil contact angle and photocatalytic activity vs number of passes respectively. The number of passes refers to the number of times water is added to the separation system as presented later. It was found that our Janus membrane shows that oil contact angle is about 153° ± 2° after 10 passes of permeation of water and has a high flux (4015±144 $L/m^{2-}hr$) for each pass during the separation process of free oil-water mixtures as shown in **Fig. 4-18**. **Figure 4-19** is the robustness of the TiO_2 membrane coating as measured by comparing the photocatalytic degradation efficiency α (%) for 5 separate feed samples with the same initial concentration of MB dye ($C_o = 5$ mg/L) and volume (10 mL) after 10 passes for each sample using the same membrane at a constant UV intensity (372 mW/cm^2). Inset shows the absorbance of the five samples as nearly equivalent after each group of 10 passes illustrating the robustness of the permeate-side coating. In another robustness test, we also measured the degradation efficiency attained after every 2 passes as a function of the number of passes and found this value to be a constant $40.0 \pm 2.0\%$ as shown in **Fig. 4-20**. The photo-degradation efficiency is calculated using a calibration curve for the photodegradation efficiency α of MB dye on TiO_2 coated membrane versus the area under the MB absorbance curve as shown in **Fig. 4-21**. We found that the influence of UV light illumination on the feed side coating materials is negligible having an almost constant oil contact angle of 153° ± 2° even after 10 passes.

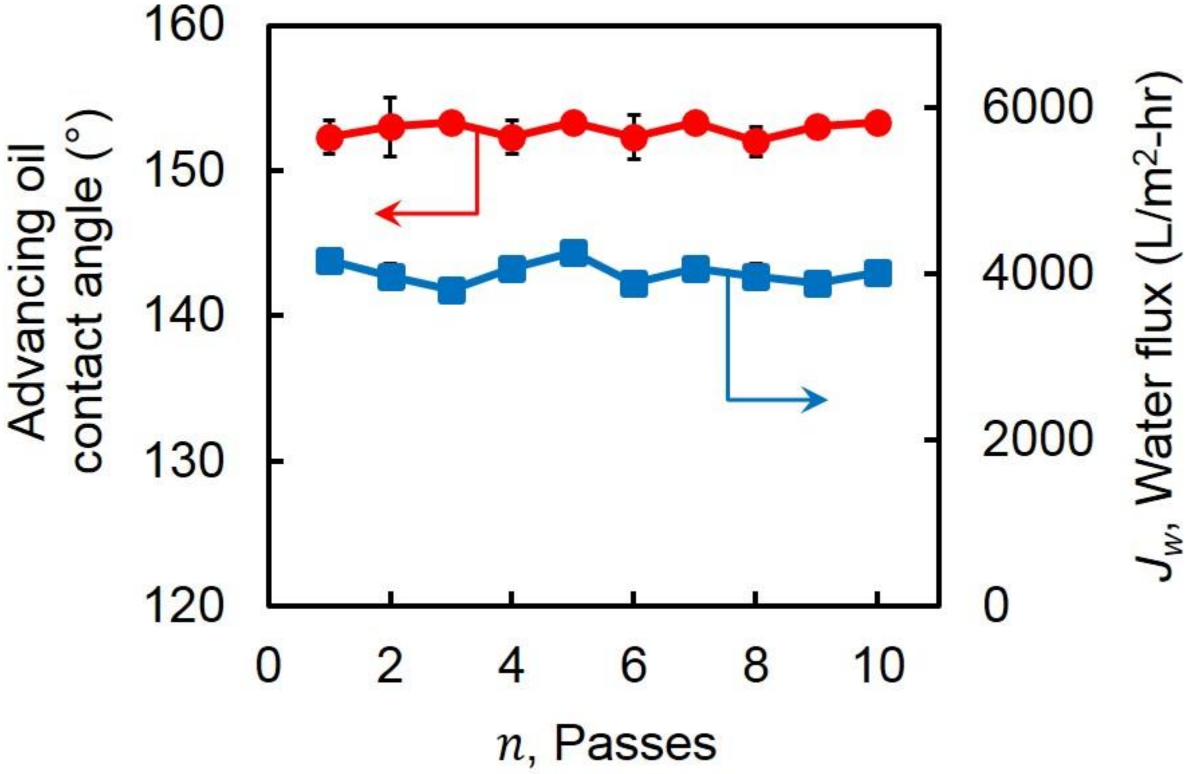

Figure 4 - 18 Advancing contact angles for hexadecane on the feed-side of the Janus membrane and water flux as a function of the number of passes.

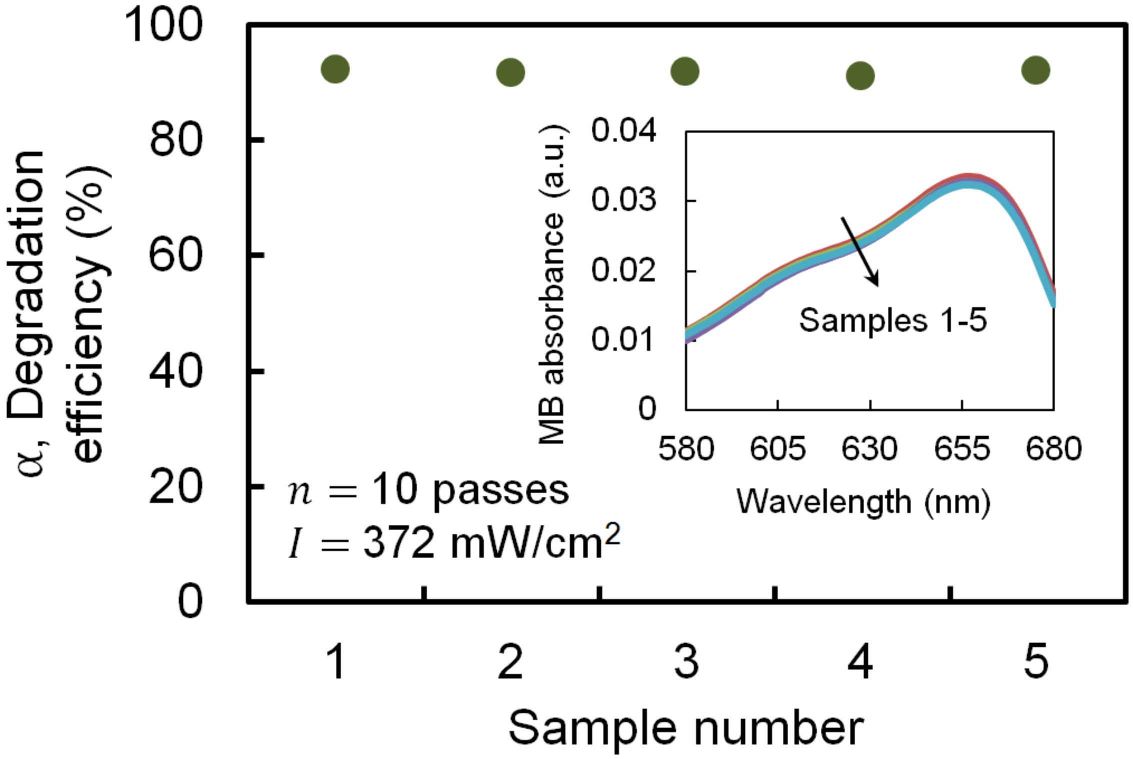

Figure 4 - 19 The photocatalytic degradation efficiency for five separate feed samples with the same initial concentration of MB dye and volume after 10 passes for each sample using the same membrane at a constant UV intensity.

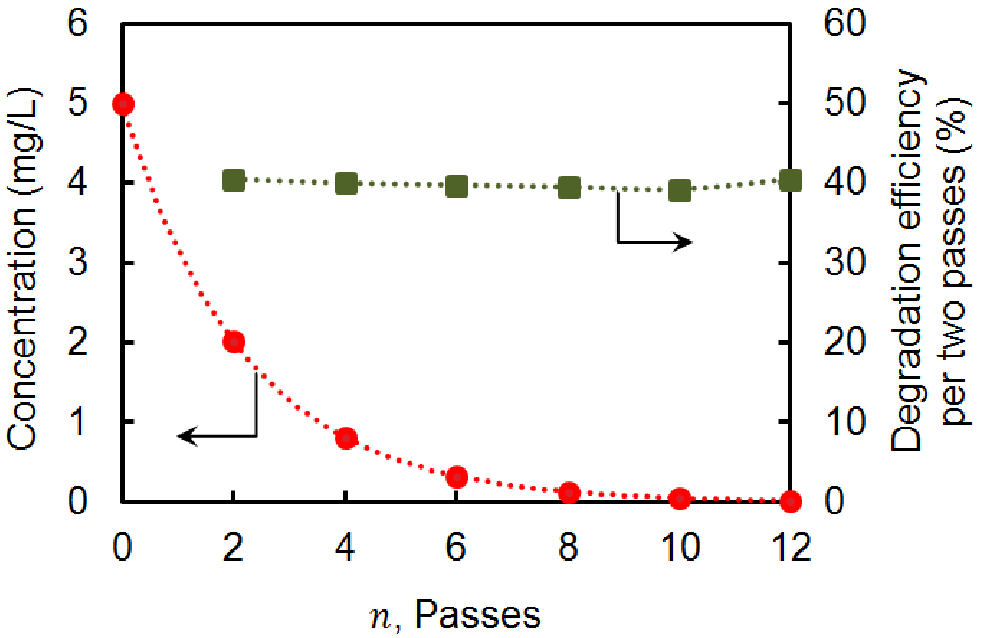

Figure 4 - 20 Concentration and degradation efficiency per two passes of organic pollutants (Methylene Blue dye) using TiO_2 coated membranes as a function of number of passes at constant UV light intensity

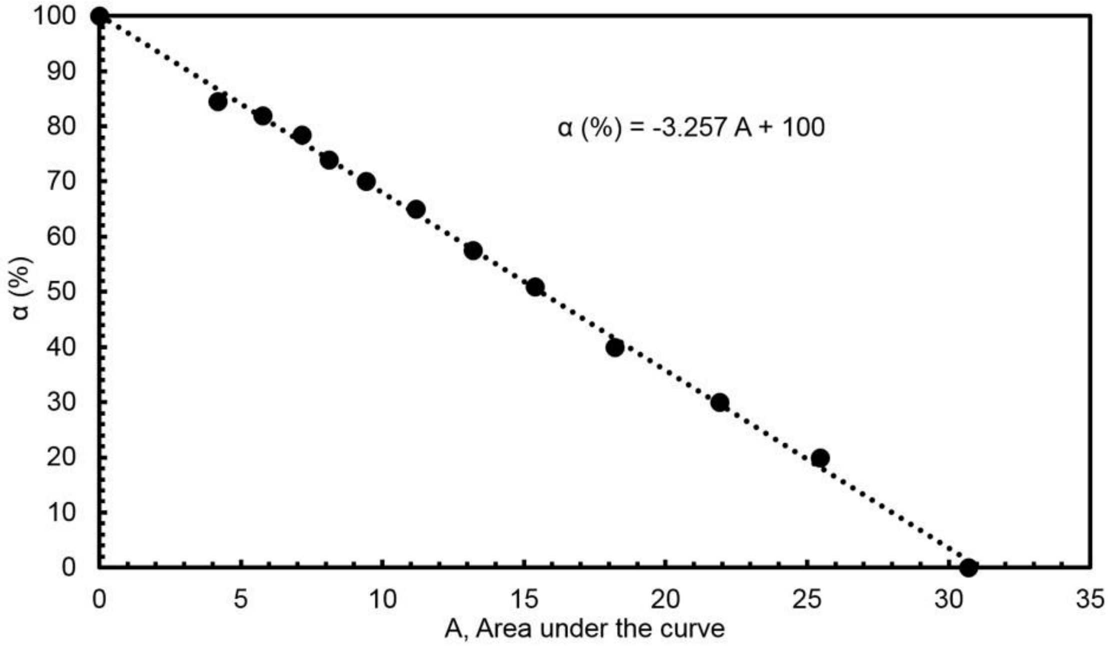

Figure 4 - 21 The calibration curve of the photo-degradation efficiency of MB dye on TiO_2 coated membrane versus the area under the MB absorbance curve (area under the curve, A).

A schematic illustration of the Janus membrane is shown in **Fig.4-22**. Therefore we anticipate that organic pollutants are photo-degraded while the water-rich permeate passes through the TiO_2 coated membrane. In order to verify this, we performed a series of tests for photo-catalytic degradation of organics in the water-rich permeate. We utilized MB dye as a representative organic pollutants present in the water-rich permeate which has been used in many studies[100, 124] and has negligible solubility in hexadecane. MB dye-contaminated water (initial concentration, C_o = 5 mg/L) is introduced to the Janus membrane. As soon as it contacts the Janus membrane, it permeates through the membrane under gravity. While MB dye-contaminated water permeates, UV light (intensity = 1050 mW/cm2) is illuminated the permeate-side of the Janus membrane. Therefore MB dye in the water is photo-degraded while it passes through the TiO_2 coated surface upon UV light illumination. After all the water passes through the Janus membrane, we again introduce the water to our membrane for further photo-degradation of MB dye.

Figure 4-23 shows a plot of MB dye absorbance in the permeates as a function of number of passes. After 10 passes, nearly all the MB dye molecules are degraded via photo-catalytic degradation upon UV light illumination as shown in the inset. Note that MB dye is not photo-bleached by UV light illumination. **Figure 4-24** shows the physical adsorption of MB dye on TiO_2 coated membrane compared with initial concentration of MB dye and the photolysis of MB dye by UV light on uncoated membrane at the lowest and highest intensities used in this study (372 and 1050 $mWcm^{-2}$).

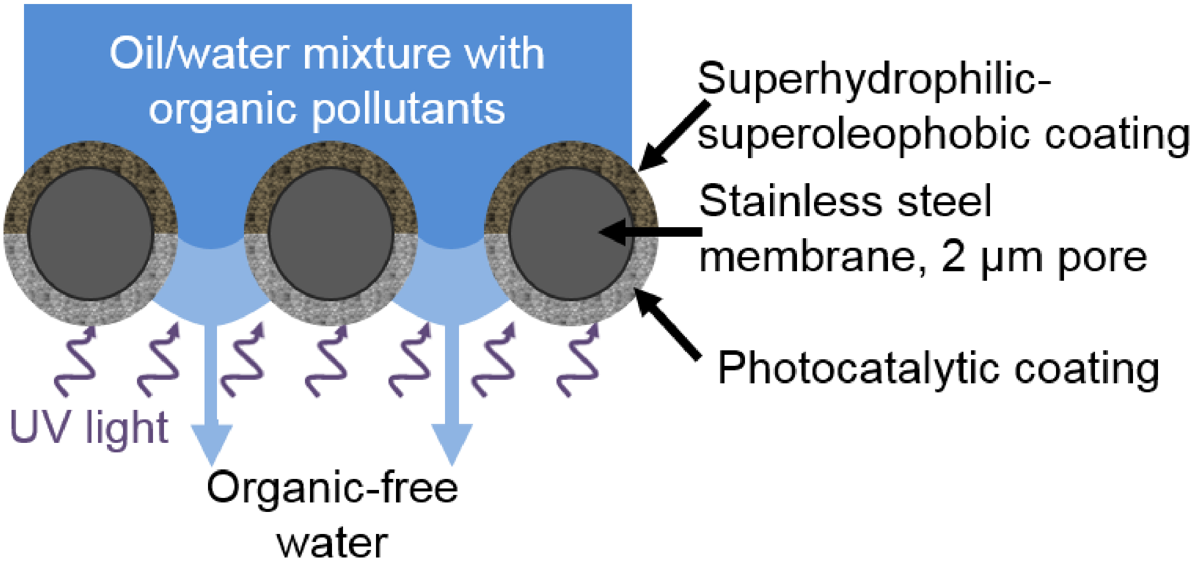

Figure 4 - 22 A schematic illustration of the Janus membrane that can separate oil-water mixtures without water pre-wetting by gravity and photo-degrade organic pollutants from the water phase upon UV light illumination.

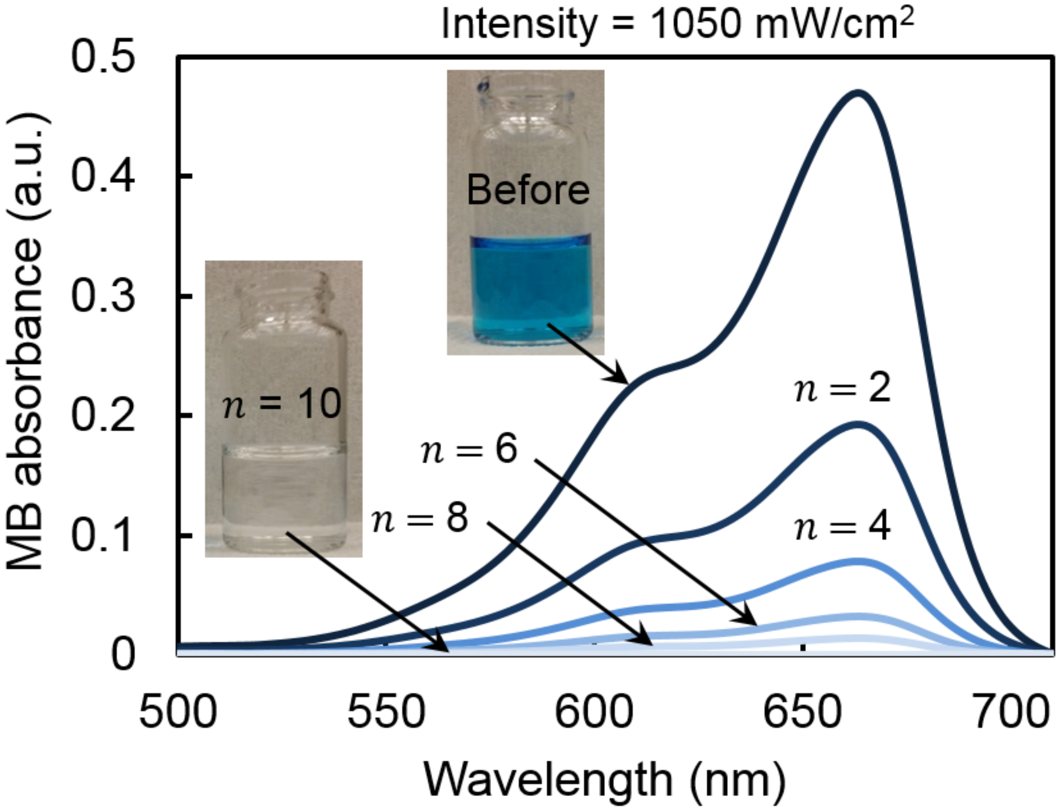

Figure 4 - 23 Absorbance spectra of the organic MB dye after consecutive passes at UV intensity of 1050 mW/cm^2. Inset photos show water-contaminated MB dye before and MB dye-free water after 10 passes.

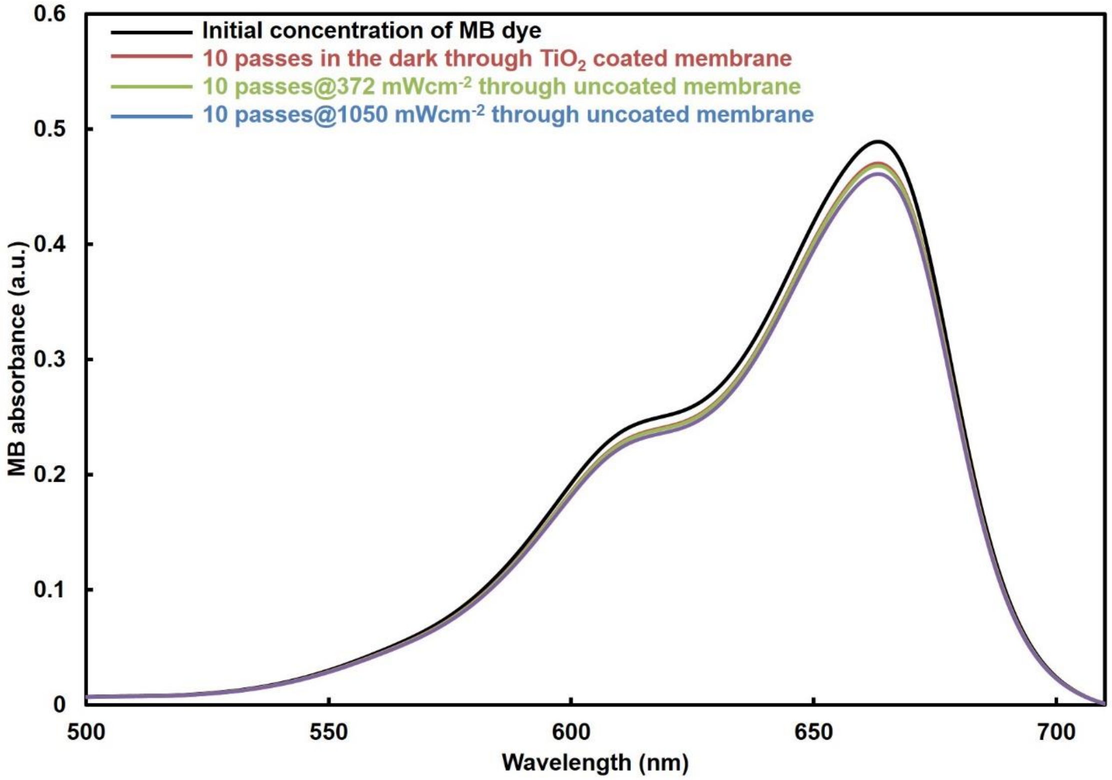

Figure 4 - 24 The physical adsorption of MB dye on TiO_2 coated membrane compared with initial concentration of MB dye and the photolysis of MB dye by UV light on uncoated membrane at the lowest and highest intensities used in this study (372 and 1050 mWcm^{-2}).

The Langmuir-Hinshelwood kinetic model has been used to characterize the photo-degradation of organic pollutants on TiO_2 surfaces[36, 104, 125]. We develop a mathematical model to describe the photo-catalytic degradation of organic molecules present in the water-rich permeate during its permeation. **Figure 4-25** shows a schematic illustration of organics degradation system associated with UV light illumination. The photo-degradation system is comprised a TiO_2 coating on the permeate side of the Janus membrane and the various experimental parameters such as reactor volume, UV light intensity, flux, number of passes. The TiO_2 reactor volume refers to the effective volume over the membrane surface area which participates in the photo-degradation process when excited by UV.

When the dye adsorption is weak and/or the MB blue concentration is low, as it is in our current work, the Langmuir-Hinshelwood equation reduces to a first order kinetics reaction (see **Supplementary Sec. A.1** for derivation details). The concentration of organic pollutant C_t as a function of the organic pollutant residence time t within the TiO_2 reactor volume is given by:

$$C_t = C_o e^{-k_a\, t} \tag{4.1}$$

Where C_o is the concentration at $t = 0$ and k_a is the apparent first order rate constant (s^{-1}). When the UV illumination intensity I provided exceeds a threshold value between 1-10 mW/cm^2, as is the case in our current work, the k_a is linearly proportional to $I^{1/2}$ with a proportionality constant which we call β ($cm/mW^{1/2}$-s)[105][127]:

$$k_a = \beta I^{1/2} \tag{4.2}$$

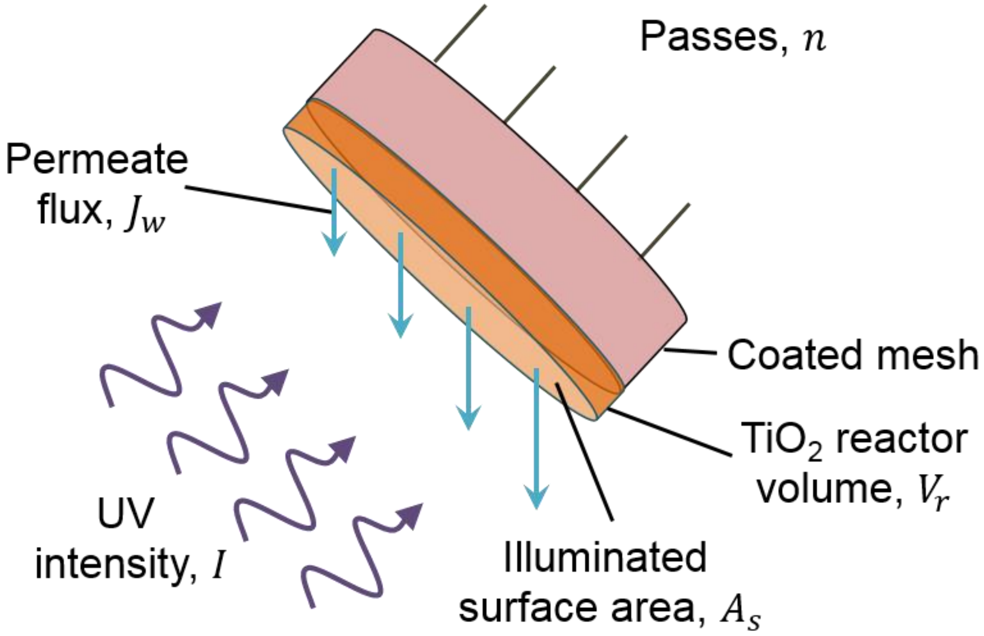

Figure 4 - 25 A schematic illustration of organics degradation system and relevant parameters for photo-degradation model.

Substituting Eq. 4.1 in 4.2 yields the following expression for C as a function of time and intensity:

$$C_t = C_o e^{-\beta I^{1/2} t} \tag{4.3}$$

For a closed reactor within which there is no dispersion across particle streamlines, we can define the mean residence time t as the ratio of the reactor volume by the volume flow rate through the reactor[128]:

$$C_t = C_o e^{-\beta I^{1/2} \frac{V_r}{J_w A_s}} \tag{4.5}$$

Where V_r (m^3) is the volume of the pores on the permeate side of the membrane participating in the photo-degradation reaction, J_w is the permeate flux through the membrane (m/s), and A_s is the wetted surface area of the membrane (m^2). Defining a dimensionless photo-degradation efficiency as $\alpha = 1 - C_t/C_o$ and multiplying the term in the exponential function by n to allow for multiple passes through the reactor yields parameters relevant to the current system:

$$\alpha = 1 - e^{-\beta I^{1/2} \frac{V_r n}{J_w A_s}} = 1 - e^{-\beta X} \tag{4.6}$$

Where X is a collapsed variable that encapsulates several input parameters. β is the photo-catalytic degradation system figure of merit with units of (cm/mW$^{1/2}$-s) and is a function of the choice of photo-catalytic surface used, the wavelength of the UV source, the type of reactor, the type of organic pollutant present in the water phase, and the turbidity of the feed solution. Equation 4.6 shows that a higher value of β results in greater photo-degradation efficiency for fixed X. Our figure of merit can be used by other researchers for photo-catalytic purification in both batch mode ($n > 1$) and continuous operation ($n = 1$).

In our experiments, the intensity was varied from $I\ = 150$ to 1530 W/cm^2 with up to 10 passes. Our permeate flux was $J_w = 1.12 \times 10^{-3}$ m/s and our reactor volume was estimated at $V_r = 2.55 \times 10^{-9}$ m^3 (**Calculations are detailed in Sec. A.1)**. In order to validate our model, we performed a series of permeation tests with different number of passes (n) and Intensities (I). **Figure 4-26 and 27** shows a plot of photo-degradation efficiency (α) as a function of number of passes at constant intensity and UV light intensity at constant number of passes respectively. It clearly indicates that photo-degradation efficiency increases with increasing number of passes. In addition, we found that photo-degradation efficiency α reaches its maxima (>99.9%) at a high UV intensity ($I\ = 1050$ mW/cm^2) and $n\ = 10$ passes. Detailed experimental parameter inputs, empirical results, model results, and errors are provided in **Supplementary Sec. A.2**. For the range of parameters used in our study, the apparent first-order rate constant $k_a = \beta I^{1/2}$ varies between 14.38×10^{-3} s^{-1} and 45.93×10^{-3} s^{-1} which is similar in magnitude to values reported in the literature[104, 126]. **Figure 4-28** shows a plot of photo-degradation efficiency as a function of variable X which consists of number of passes, light intensity, reactor volume, and surface area. Our model matches well with the data obtained from experiments. Across all data, our maximum model error was 3.9% while our mean error was 1.2%.

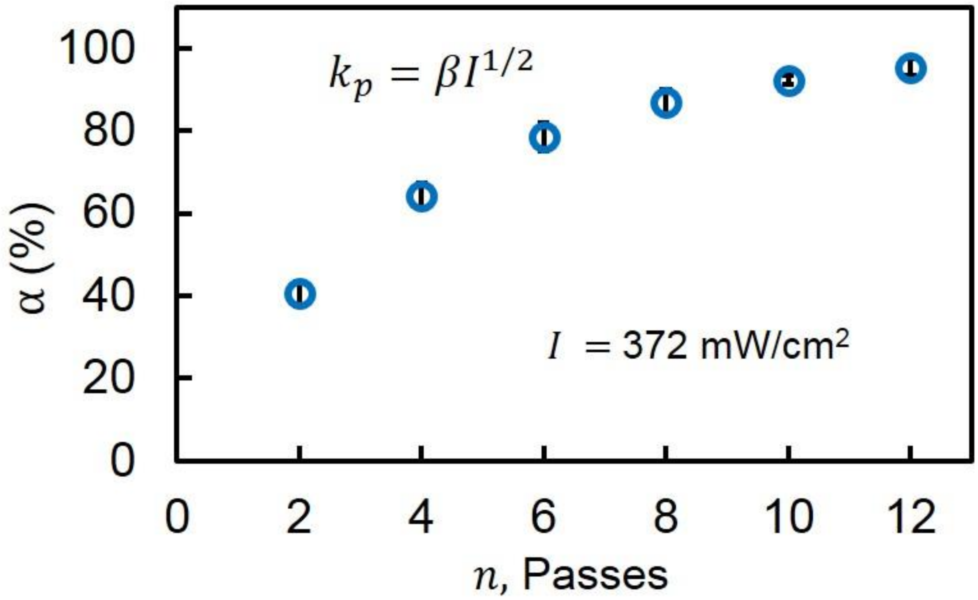

Figure 4 - 26 Degradation efficiency of TiO_2 coated membrane as a function of number of water passes at constant UV light intensity.

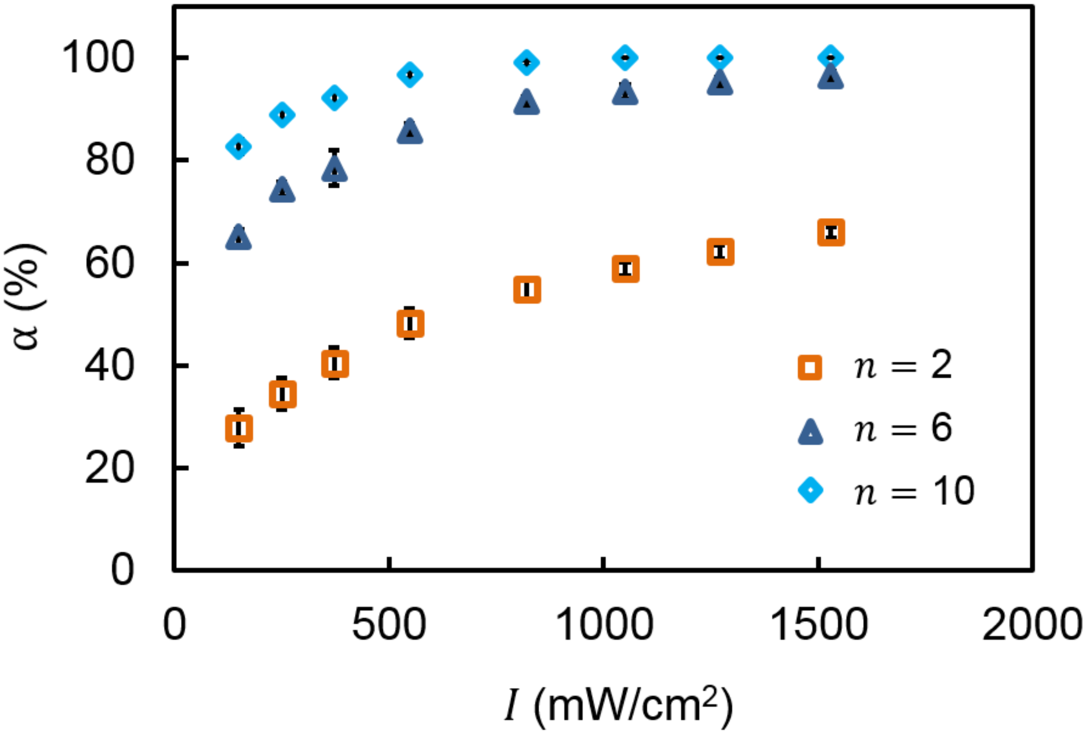

Figure 4 - 27 Photo-degradation efficiency of TiO_2 coated membrane as a function of UV light intensity at constant number of passes.

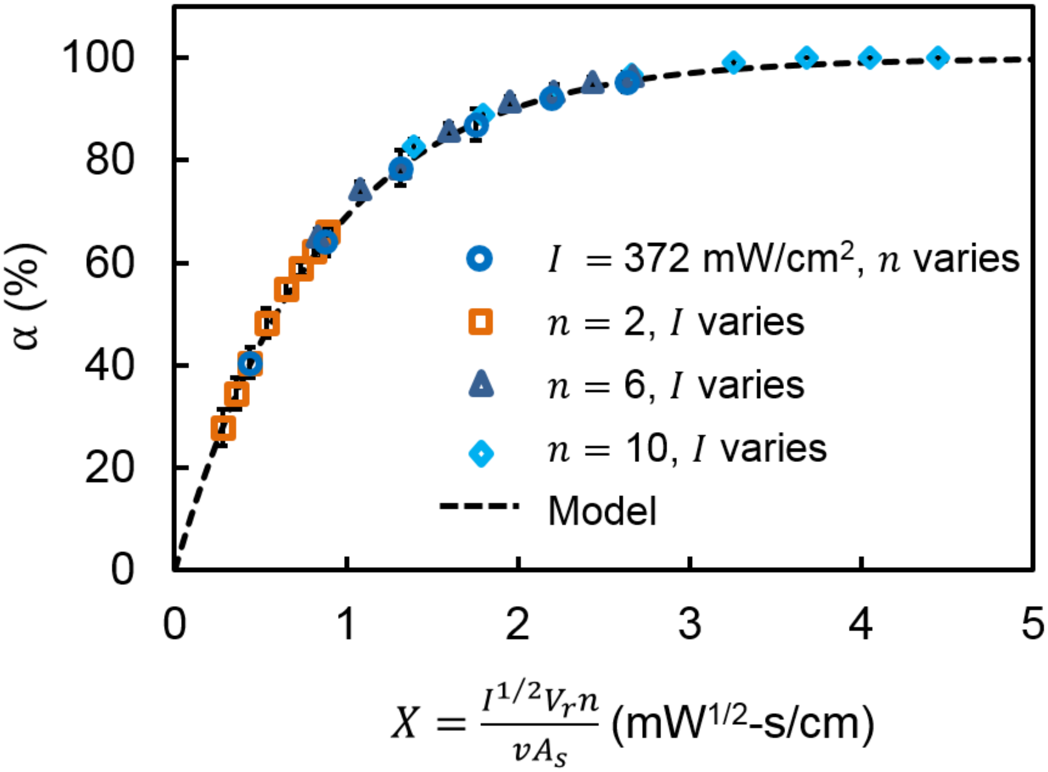

Figure 4 - 28 Photo-degradation efficiency as a function of X. Symbols correspond to empirical data while the dashed line corresponds to the photo-degradation model..

The model developed in this work can provide us with design parameters for complete photo-degradation of organic pollutants in the water-rich permeate during the separation of oil-water mixtures. Guided by our model, we demonstrated complete separation and the in situ photo-degradation of organic pollutes in free/emulsified oil-water mixtures. The Janus membrane is sandwiched between two glass tubes and the apparatus was tilted by 20 degrees with respect to the vertical axis so that the UV lamp is protected from the permeate falling during the operation of the system. Then, UV light is illuminated on the permeate side of the membrane during separation operation as shown **in Figure 4-29**. To test the degradation and separation performance of our Janus membrane, we first used the membrane for free hexadecane-water separation and in-situ MB dye degradation. A hexadecane-water mixture (1:1 by volume) with MB dye present in the water phase was poured into our apparatus without pre-wetting the membrane. MB dye is a model organic pollutant which has been used in many studies [100, 102, 128-130] and has negligible solubility in hexadecane. With a UV intensity of 1050 mW/cm^2 and 10 water loops, neither oil nor MB dye were visually observed in the water permeate as shown in **Fig.4-30**, demonstrating high separation and purification performance (Video S9). A thermogravimetric analysis plot of the permeate from the oil-water mixture showed extremely high oil rejection (~ 99.9%) as shown in **Fig. 4-31**. Oil rejection is defined as $R = 1 - C_p/C_f$ where C_p is the concentration by volume of oil in the final permeate and C_f is the oil concentration by volume in the initial feed.

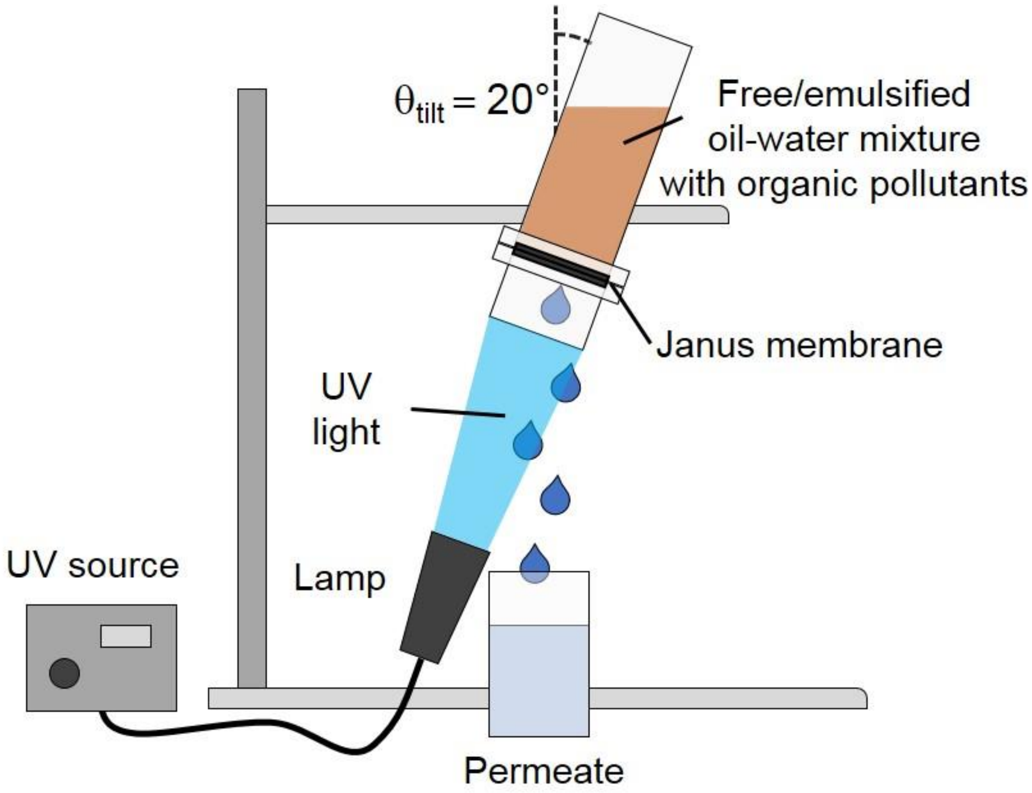

Figure 4 - 29 A schematic illustration of the separation and photo-degradation apparatus used in our experiments.

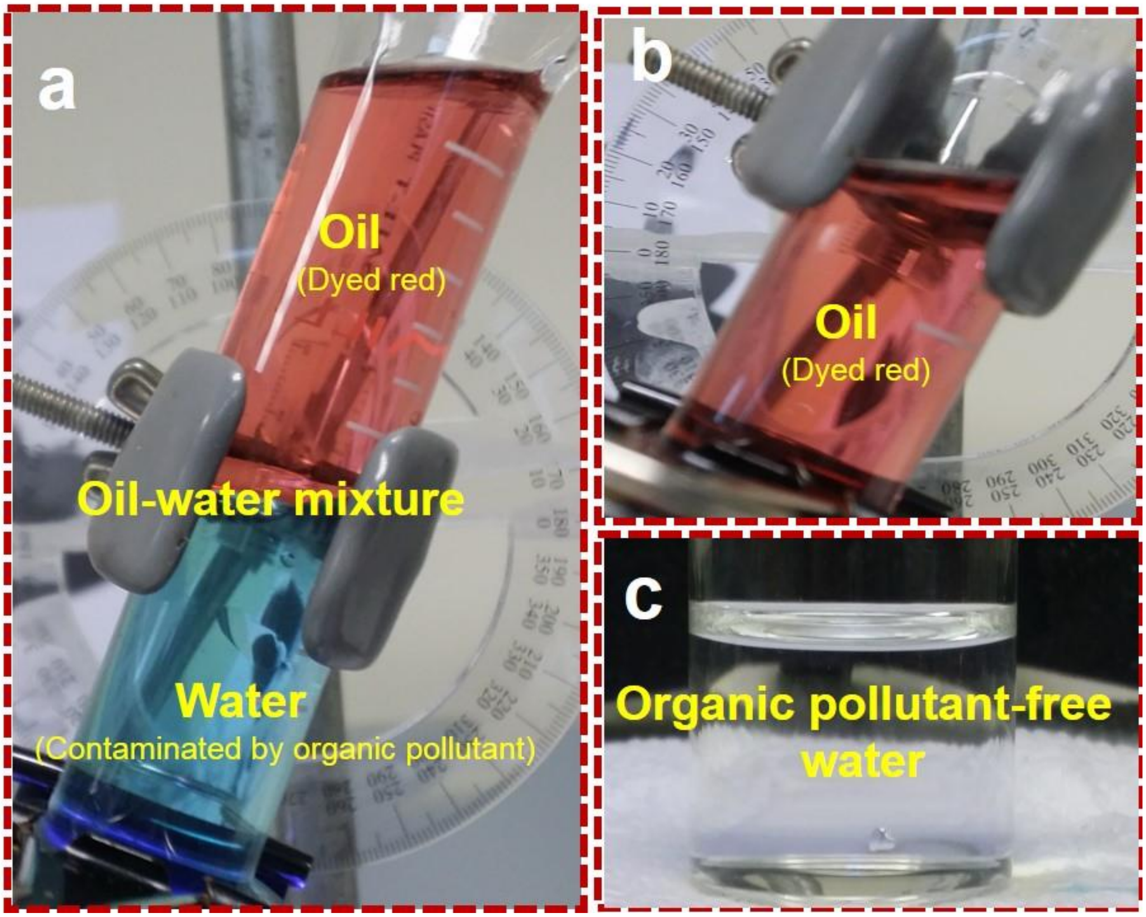

Figure 4 - 30 (a) A photograph of the apparatus with free 1:1 hexadecane-water mixture above the Janus membrane. (b) and (C) Hexadecane is retained whereas MB dye-free water is collected after 10 passes.

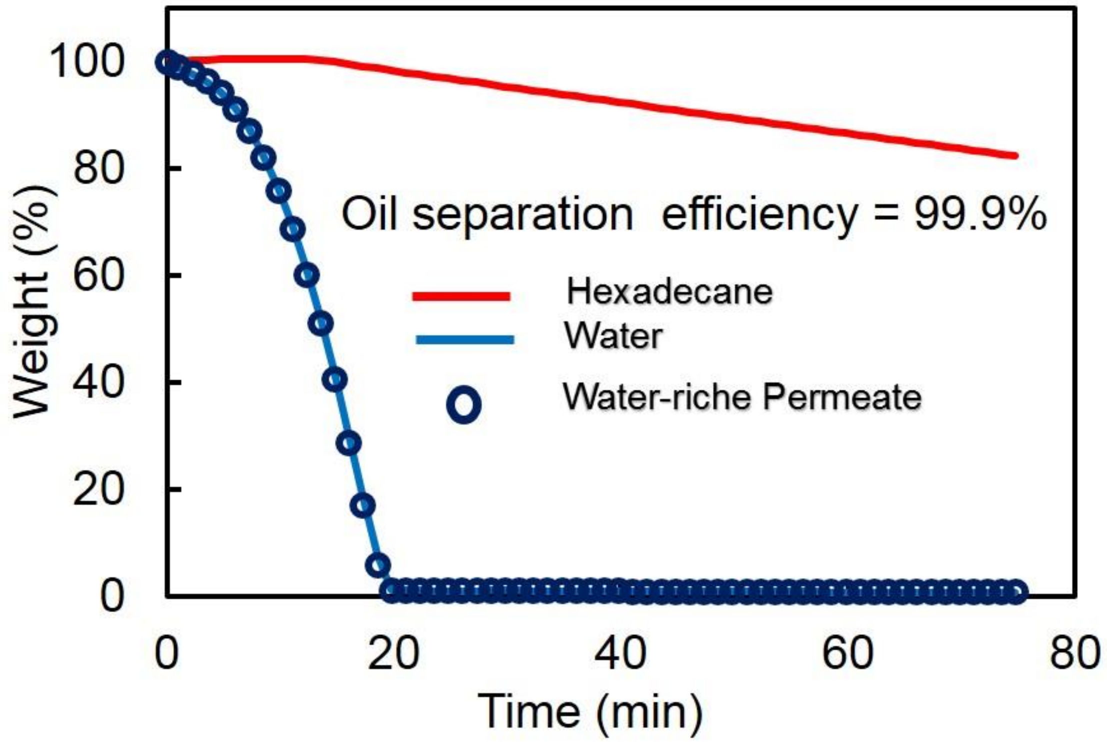

Figure 4 - 31 Thermogravimetric analysis (TGA) data of water, hexadecane, and feed solution permeate after 10 passes with high oil rejection.

Our model predicts that MB dye concentration of 5 mg/L can be ~99.9 % photo-degraded after one pass upon UV light with intensity $\geq 265, 120$ and 26 mW/cm^2 when the flux is $190{,}128\ and\ 60$ L/m^2-hr respectively. We performed the separation of the emulsified oil-water mixture using above parameters (Flux= 128 L/m^2-hr) and showed a complete photo-degradation of MB dye from the water-rich permeate.

Figure 4-32 depicts the experimental apparatus and performance of the Janus membrane for the separation of surfactant-stabilized oil-in-water emulsions and in-situ organic pollutants degradation (Video S10). MB dye-contaminated DI water was used to prepare three surfactant-stabilized hexadecane-water emulsions with volume ratios of 1:4, 1:1, and 4:1 oil to water. The prepared emulsions were separated and photocatalytically treated. As a result of the selective wettability and photocatalytic activity of the multifunctional membrane, oil phase is retained above the membrane during the separation of all the emulsions and and MB dye-free water permeates through our membrane upon UV illumination after only one water loop. The flux is 190 ± 9, 128 ± 6, and 60 ± 3 L/m^2-hr for the 1:4, 1:1, and 4:1 oil-water emulsions, respectively. The oil rejection efficiency for each emulsion are given in **Fig. 4-33**. These results indicate that our multifunctional membrane demonstrates excellent oil rejection efficiency (~ 99.9%) with surfactant stabilized emulsions in addition to simultaneous organics degradation efficiency (~ 99.9%) for all emulsions. It was found that our model matches well with the experimental data as shown in **Figure 4-34**.

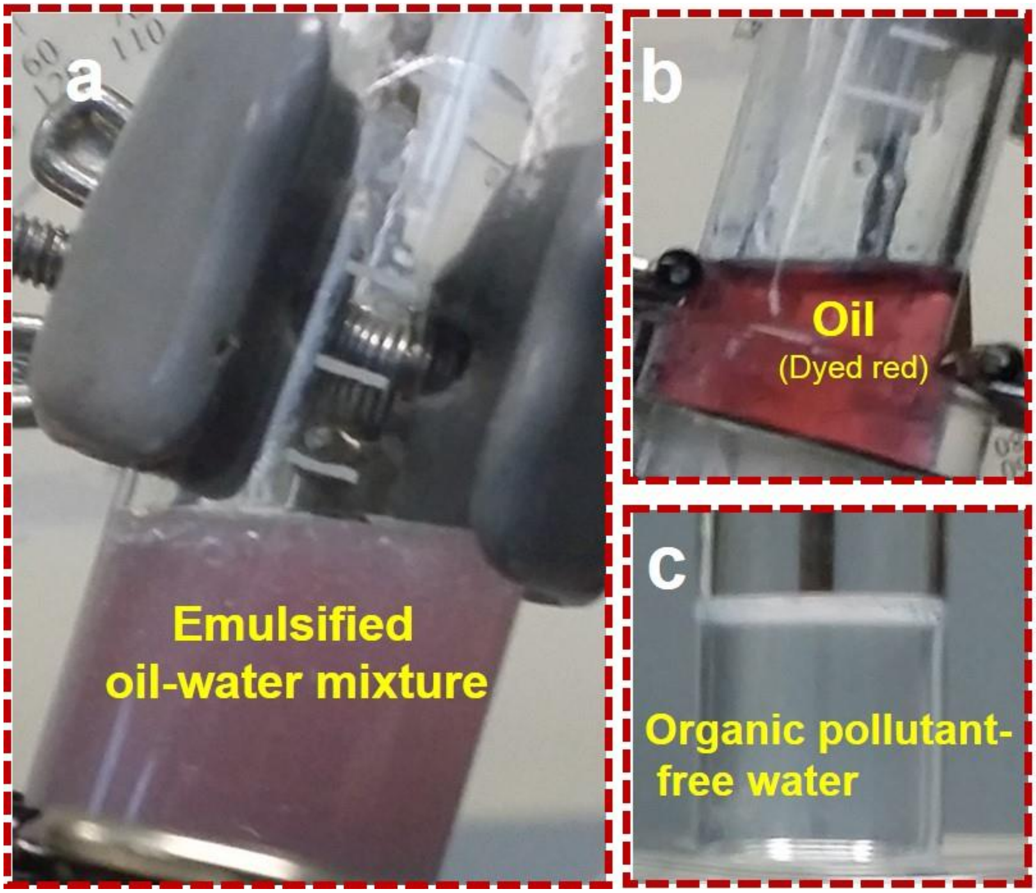

Figure 4 - 32 (a) A photograph of the apparatus with 1:1 emulsified hexadecane-in-water mixture above the Janus membrane. (b) Oil is retained whereas MB dye-free water is collected after 1 pass upon UV light with intensity ≥ 548 mW/cm2 when the flux is 128 L/m^2-h.

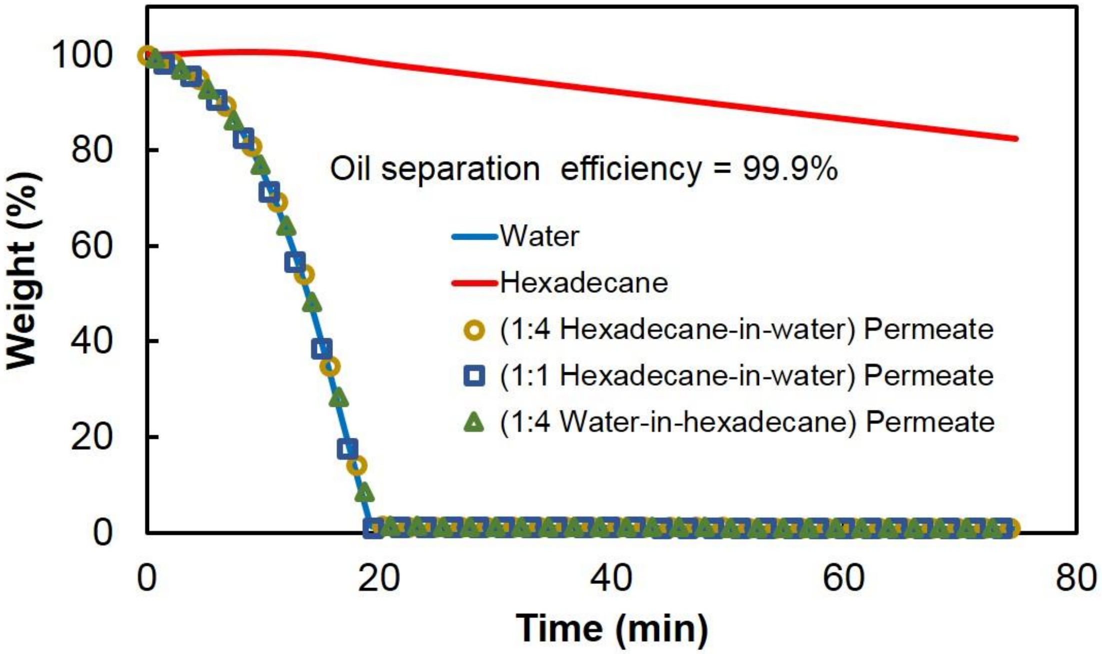

Figure 4 - 33 Thermogravimetric analysis (TGA) data of water, hexadecane, and feed solution permeate after one pass with high oil rejection.

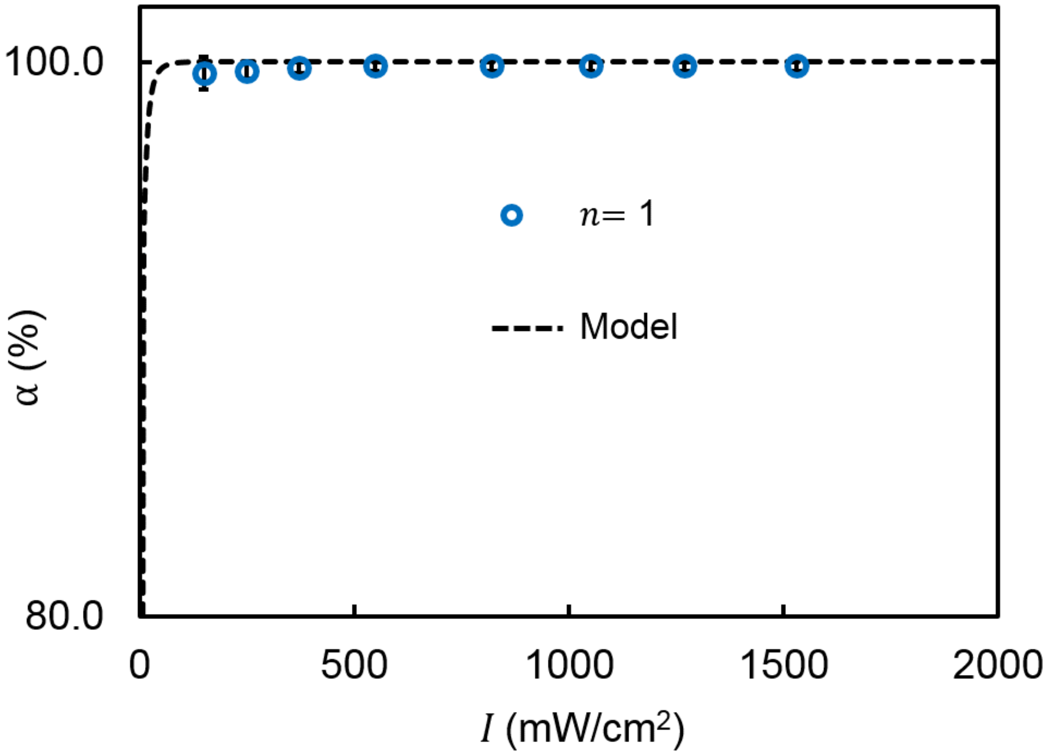

Figure 4 - 34 Photo-degradation efficiency of the Janus membrane as a function of UV light intensity at one pass of 1:1 oil-in-water emulsion.

Optical microscopy images and droplet size distributions of each emulsion and its permeate, provided in **Fig. 4-35**. **Fig. 4-35-a,c and e** show the optical microscopy images of 1:4, 1:1, and 4:1 (hexadecane:water by volume) emulsions, respectively. 1:4 and 1:1 emulsions are oil-in-water and 4:1 emulsion is water-in-oil. **Fig. 4-35-b,d and f** show droplet size distributions of 1:4, 1:1, and 4:1 emulsions, respectively. **Fig. 4-35-g,h and I** show the optical microscopy images of 1:4, 1:1, and 4:1 permeates, respectively. We can clearly see that many of the large droplets present in the feed stream are not present in the water-rich permeate after separation.

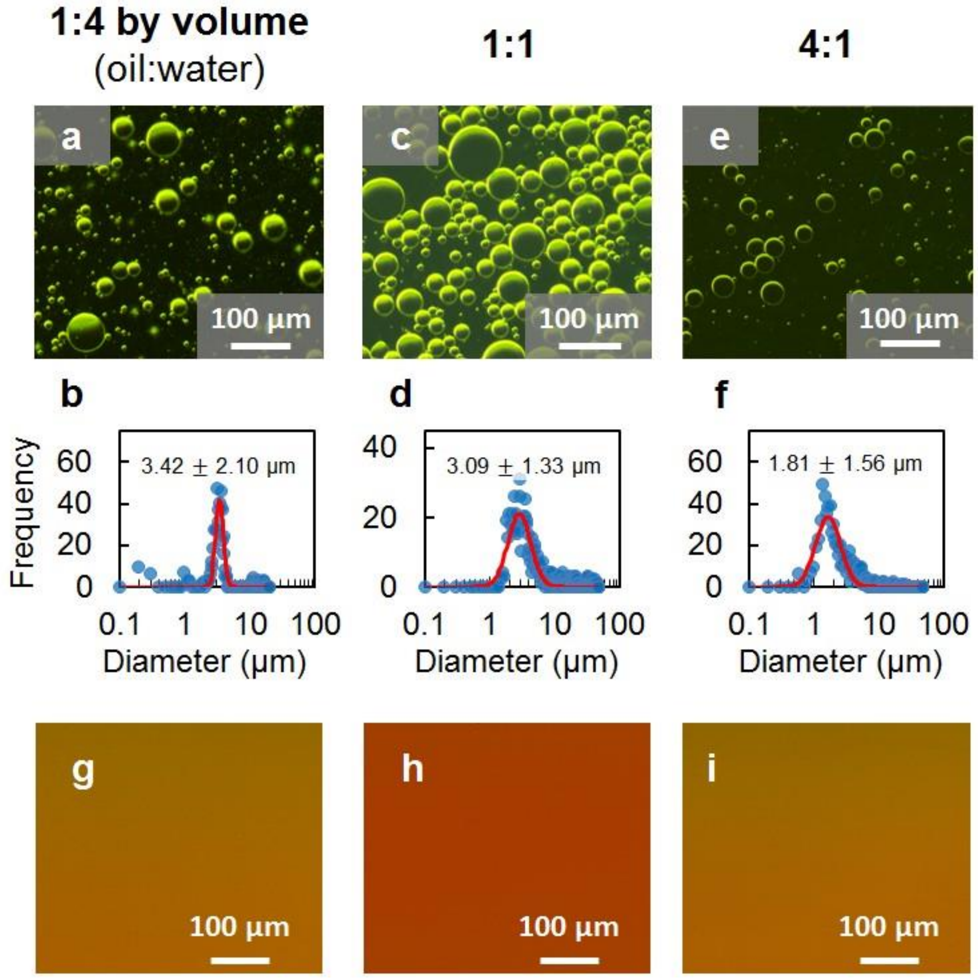

Figure 4 - 35 **(a), (c) and (e) show the optical microscopy images of 1:4, 1:1, and 4:1 (hexadecane:water by volume) emulsions, respectively. (b), (d) and (f) show droplet size distributions of 1:4, 1:1, and 4:1 emulsions, respectively. (g), (h) and (I) show the optical microscopy images of 1:4, 1:1, and 4:1 permeates, respectively.**

CHAPTER

CONCLUSION

We have used a cheap and easily available paraffin candle to prepare highly stable carbon nanoparticles (20-50 nm) dispersions in different solvents. The candle soot is mesopores nanomaterial with an average pore size of 7 nm and large BET surface area 366 m^2g^{-1} that can be used for different applications. To show the advantage of our nanomaterial for practical and large-scale applications, the synthesized carbon nanomaterial was used to fabricate superhydrophobic surfaces using spray coating-based technique. The spray coating-based surfaces exhibit much higher mechanical robustness compared to the surface fabricated by direct candle flame soot deposition. In addition, the spray coating -based surfaces are thermally stable over a wide temperature range up to 400 ^{o}C. The results of this work assures the potential of this technique that it can be used for the fabrication of mesoporous carbon nanomaterials for large-scale practical applications, which require thermally stable robust superhydrophobic surfaces and also for the solar cells electrodes and band gap engineering of metal oxides.

Also, we have presented a facile synthesis of mechanically robust, scalable stainless steel multifunctional membrane capable of being an efficient medium for gravity driven water passing kind of oil- water separation and photocatalytic degradation of organic pollutants in the permeated water. These remarkable features on the 316L stainless steel membranes were brought about by simple annealing of the membranes at 800 °C and 1000 °C. The SEM images of the annealed membranes showed the introduction of a nanostructured surface roughness on the annealed membranes, this nanoscale roughness along with the microscale pore size of the membrane provided the necessary hierarchical structure to change the surface with the desired wettability of superhydrophillicity and under water superoleophobicity as confirmed by the respective contact angle and sliding angle measurements. Also the formation of Fe_2O_3 and/or Fe_2O_3-based composites on the annealed membrane surface, as indicated by XPS studies, served as a visible light driven photocatalyst for the degradation of organic dyes present in the water permeate. As anticipated from the improved wettability of the annealed membranes, the application of it as a separating medium showed excellent oil-water separation efficiency in passing water though with very high permeation flux and retaining the oil on the top. Also the annealed membranes exhibited an excellent photocatalytic degradation of organic dye in the permeated water under visible light irradiation. We anticipate that this approach will provide a promising pathway for versatile applications in oily wastewater treatment and water purification.

Finally, we have successfully developed and presented the first single unit operation Janus membrane with selective wettability (oil is retained) and photocatalytic properties. Our fabricated Janus membrane is chemically robust and easy to manufacture. It uses two distinct coatings on one porous stainless steel mesh membrane to simultaneously separate oil and water via gravity and purify permeate *in-situ* with ultraviolet illumination. Because a separate coating is used for degradation which does not participate in oil-water separation, our Janus membrane provides flexibility in the choice of photocatalyst based on the pollutants present in the water phase and the wavelength of the radiation source. Our Janus membrane demonstrated excellent oil rejection with bulk oil-water mixtures and surfactant stabilized emulsions (oil-in-water and water-in-oil) in addition to simultaneous organics degradation (using MB dye as a model contaminant). We presented an accurate analytical model (mean error = 1.2%) to predict the organic degradation performance of the permeate-side coating of our Janus membrane for batch and continuous flow systems using TiO_2. We defined a figure of merit, β with units of cm/mW$^{1/2}$-s, which can be used to compare degradation performance between photocatalytic systems by other researchers. We expect that our single unit operation Janus membranes could be used for effective separation of oily wastewaters and simultaneous photo-degradation, showing great potential for oil-water separation and simultaneous treatment of hazardous pollutants from wastewater at an industrial level.

APPENDIX

A. 1 Organics photo-degradation model

We begin our model with the Langmuir-Hinshelwood relation for concentration reduction as a function of time due to adsorption and reaction at a surface as is often done in the literature[101], [103], [105]:

$$\frac{dC}{dt} = -\frac{k_p k_{ads} C}{1 - k_{ads} C} \tag{A.1.1}$$

where C is the concentration of organic pollutant (mg/L), t is the organic pollutant residence time within the TiO_2 reactor volume (s), k_{ads} is the adsorption constant of the organic molecule to be degraded (L/mg), and k_p is a rate constant associated with the photocatalytic process (mg/L-s).

The maximum organic contaminant (MB dye) concentration used in this study was 5 mg/L and the adsorption constant for methylene blue dye is $k_{ads} = 1.95 \times 10^{-2}$ L/mg [101]. Therefore, we can safely assume that $k_{ads}C \ll 1$, so that Eq. S1 reduces to a first order kinetics reaction:

$$\frac{dC}{dt} \approx -k_p k_{ads} C = -k_a C \tag{A.1.2}$$

where k_a is an apparent rate constant (s^{-1}). When the UV illumination power I provided exceeds a threshold value of between 1-10 mW/cm^2, as it does in our current work, then k_a is linearly proportional to $I^{1/2}$ with a proportionality constant which we call β ($cm/mW^{1/2}$-s)[105][127]:

$$k_a = \beta I^{1/2} \tag{A.1.3}$$

Rearranging and taking the integral of Eq. A.1.2 with initial condition $C(t_o = 0, t) = (C_o, C_t)$ yields the following expression for C as a function of time:

$$C_t = C_o e^{-\beta I^{1/2} t} \tag{A.1.4}$$

For a closed reactor within which there is no dispersion across particle streamlines, we can define the mean residence time t as the ratio of the reactor volume by the volume flow rate through the reactor [128]:

$$C_t = C_o e^{-\beta I^{1/2} \frac{V_r}{J_w A_s}} \tag{A.1.5}$$

where V_r (m^3) is the volume of the pores on the permeate side of the membrane participating in the photo-degradation reaction, J_w is the permeate flux through the membrane (m/s), and A_s is the wetted surface area of the membrane (m^2). Defining a dimensionless degradation efficiency as $\alpha = 1 - C_t/C_o$ and multiplying the term in the exponential function by n to allow for multiple passes through the reactor yields parameters relevant to the current system:

$$\alpha = 1 - e^{-\beta I^{1/2} \frac{V_r n}{J_w A_s}} = 1 - e^{-\beta X} \tag{A.1.6}$$

where X is a collapsed variable that encapsulates several input parameters.

V_r was estimated by considering the volume of the pores on the permeate side of the multifunctional membrane. Because the mesh used in this study was a complex twill Dutch weave wire cloth, we estimate the reactor volume by subtracting the volume of the wires of the mesh from the total volume occupied by the mesh. All the calculations were performed using data from the manufacturer’s website. The volume of the wire material is attained by dividing the specific weight of the mesh 0.488 kg/m^2 by the density of 316 stainless steel 7990 kg/m^3 and multiplying by the wetted mesh area to give 1.23x10^{-8} m^3. The volume occupied by the mesh is given by multiplying the mesh thickness 86.36x10^{-6} m by the wetted mesh area to give 1.74x10^{-8} m^3. Taking the difference of these volumes gives the volume of the pores in the mesh of 5.08x10^{-9} m^3. We now consider that only the lower half of the mesh has been coated with TiO_2 and is photoactive so that the reactor volume is 2.55x10^{-9} m^3.

To verify whether this volume is justified, we calculated the volume of the pores from an SEM image of the mesh. The membrane is composed of a repeating array of pores as shown in **Fig. A.1-a**. The image on the right shows the structure of a typical ‘Twill Dutch weave’ in order to visualize our reactor construct.

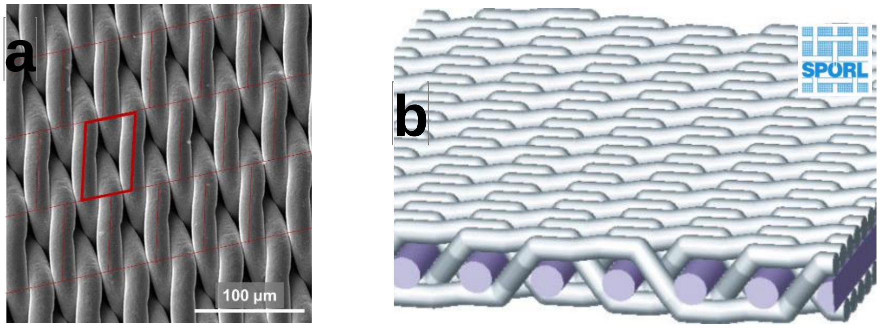

Figure A. 1(a) SEM image of twill Dutch weave mesh, (b) Digital visualization of twill Dutch weave mesh [132]. **http://www.spoerl.de/en/wp-content/uploads/sites/2/2014/08/0008_big-458x300.jpg**

The contaminants in the water react on the TiO_2 coated bottom side of the mesh as they pass through the pores. Each pore is modeled as a microreactor whose approximate volume per unit projected area is approximately calculated as below.

Area of the repeating unit, $A_{unit} = 3096.88\ \mu m^2$

Diameter of wire, $D_{wire} = 25.4\ \mu m$

Width between the warp wires = Width of the pore, $w_{pore} = 21.5\ \mu m$

Height of the pore, $h_{pore} = D_{wire}$

Length of the pore, $l_{pore} = 72.4\ \mu m$

Volume of pore, $V_{pore} \sim h_{pore} w_{pore} l_{pore} = 39537\ \mu m^2$

Volume of pore per unit area of mesh, $V_{pore} = \frac{V_{pore}^{unit}}{A_{unit}} = 12.77 \times 10^{-6}\ m^3/m^2$

Multiplying the volume of the pore per unit area by the area of the wetted membrane yields a reactor volume of 2.57x10^{-9} m^3 which has a relative difference of 0.66% from the reactor volume of 2.55x10^{-9} m^3 calculated above. Therefore, our estimation of the TiO_2 reactor volume is verified.

A. 2 Data from organics degradation experiment

Tables A.1 and A.2 contain the experimental parameter inputs (I, n, X), experimental degradation efficiency and standard deviation ($\alpha_{exp},\ \sigma_{exp}$), model degradation efficiency (α_{mod}), and model error (ε) for the fixed intensity and fixed passes data shown in **Fig. 4-16**, respectively. Model error was determined by $\varepsilon = 1 - \alpha_{mod}/\alpha_{exp}$. For all experiments, the average flux was J_w = 4015 L/m^2-hr which is 1.12x10^{-3} m/s, cross-sectional area was A_s = 2.01$\times 10^{-4}$ m^2, and excited volume of the TiO_2 reactor was V_r =2.55$\times 10^{-9}$ m^3. From the manuscript, $\beta =$ 1.174 cm/mW$^{1/2}$-s and the first-order photocatalytic rate constant $k_a = \beta I^{1/2}$ varies between 14.38×10^{-3} s^{-1} and 45.93×10^{-3} s^{-1} for the range of parameters used in our study.

Table A. 1 Effect of fixed UV intensity and varying passes on degradation efficiency.

I (mW/cm^2)	n	X (mW$^{1/2}$-hr/cm)	α_{exp} (%)	σ_{exp} (%)	α_{mod} (%)	ε (%)
372	2	0.44	40.5	3.0	40.3	0.6
372	4	0.88	64.3	3.0	64.3	0.0
372	6	1.32	78.5	3.5	78.7	0.2
372	8	1.75	87.0	3.0	87.3	0.3
372	10	2.19	92.2	1.1	92.4	0.2
372	12	2.63	95.3	2.0	95.5	0.2

Table A. 2 Effect of varying UV intensity and fixed passes on degradation efficiency.

I (mW/cm^2)	n	X (mW$^{1/2}$-hr/cm)	α_{exp} (%)	σ_{exp} (%)	α_{mod} (%)	ε (%)
150	2	0.28	27.8	3.5	27.9	0.4
250	2	0.36	34.5	3.1	34.4	0.2
372	2	0.44	40.5	3.0	40.3	0.6
548	2	0.53	48.3	2.8	46.5	3.7
820	2	0.65	54.9	1.8	53.4	2.6
1050	2	0.74	58.9	1.3	57.9	1.6
1270	2	0.81	62.2	1.2	61.4	1.3
1530	2	0.89	66.0	1.1	64.8	1.8
150	6	0.84	65.1	1.6	62.5	3.9
250	6	1.08	74.5	1.5	71.8	3.6
372	6	1.32	78.5	3.5	78.7	0.2
548	6	1.60	85.9	1.3	84.7	1.4

820	6	1.95	91.4	1.1	89.9	1.6
1050	6	2.21	93.4	1.4	92.5	1.0
1270	6	2.43	95.3	1.1	94.2	1.1
1530	6	2.67	96.4	1.0	95.6	0.8
150	10	1.39	82.7	1.4	80.5	2.6
250	10	1.80	88.9	1.0	87.9	1.1
372	10	2.19	92.2	1.0	92.4	0.2
548	10	2.66	96.7	0.8	95.6	1.1
820	10	3.26	99.0	0.6	97.8	1.2
1050	10	3.68	99.9	0.2	98.7	1.3
1270	10	4.05	99.9	0.2	99.1	0.9
1530	10	4.45	99.9	0.2	99.5	0.5

References

[1] S. B. Joye, “Deepwater Horizon, 5 years on,” *Science* , vol. 349, no. 6248, pp. 592–593, 2015.

[2] R. C. Prince, “Oil spill dispersants: Boon or bane?,” *Environ. Sci. Technol.*, vol. 49, no. 11, pp. 6376–6384, 2015.

[3] Y. Zhang *et al.*, “Titanate and titania nanostructured materials for environmental and energy applications: a review,” *RSC Adv.*, vol. 5, no. 97, pp. 79479–79510, 2015.

[4] L. Yu, M. Han, and F. He, “A review of treating oily wastewater,” *Arab. J. Chem.*, vol. 10, pp. S1913–S1922, 2017.

[5] R. P. Schwarzenbach, T. Egli, T. B. Hofstetter, U. von Gunten, and B. Wehrli, “Global Water Pollution and Human Health,” *Annu. Rev. Environ. Resour.*, vol. 35, no. 1, pp. 109–136, 2010.

[6] M. G. Anderson *et al.*, “The Challenge of Micropollutants,” *Sci. Technol.*, no. August, pp. 1072–1077, 2006.

[7] L. P. Gossen and L. M. Velichkina, “Environmental problems of the oil-and-gas industry (Review),” *Pet. Chem.*, vol. 46, no. 2, pp. 67–72, 2006.

[8] C. Wu, C. Maurer, Y. Wang, S. Xue, and D. L. Davis, “Water pollution and human health in China,” *Environ. Health Perspect.*, vol. 107, no. 4, pp. 251–256, 1999.

[9] M. A. Shannon, P. W. Bohn, M. Elimelech, J. G. Georgiadis, B. J. Marinas, and A. M. Mayes, “Science and technology for water purification in the coming decades,” *Nat. (London, U. K.)*, vol. 452, no. March, pp. 301–310, 2008.

[10] B. Li, L. Wu, L. Li, S. Seeger, J. Zhang, and A. Wang, “Superwetting double-layer polyester materials for effective removal of both insoluble oils and soluble dyes in water,” *ACS Appl. Mater. Interfaces*, vol. 6, no. 14, pp. 11581–11588, 2014.

[11] N. Liu *et al.*, “In situ dual-functional water purification with simultaneous oil removal and visible light catalysis,” *Nanoscale*, pp. 18558–18564, 2016.

[12] L. Li, Z. Liu, Q. Zhang, C. Meng, T. Zhang, and J. Zhai, “Underwater superoleophobic porous membrane based on hierarchical TiO 2 nanotubes : multifunctional integration of oil – water,” *J. Mater. Chem. A Mater. energy Sustain.*, vol. 3, pp. 1279–1286, 2014.

[13] C. Gao *et al.*, “Integrated oil separation and water purification by a double-layer TiO2-based mesh,” *Energy Environ. Sci.*, vol. 6, p. 1147, 2013.

[14] X. Lin *et al.*, “In situ ultrafast separation and purification of oil/water emulsions by superwetting TiO $_2$ nanocluster-based mesh,” *Nanoscale*, vol. 8, no. 16, pp. 8525–

8529, 2016.

[15] M. Cheryan and N. Rajagopalan, “Membrane processing of oily streams. Wastewater treatment and waste reduction,” *J. Memb. Sci.*, vol. 151, no. 1, pp. 13–28, 1998.

[16] G. Kwon, E. Post, and A. Tuteja, “Membranes with selective wettability for the separation of oil–water mixtures,” *MRS Commun.*, vol. 5, no. 3, pp. 475–494, 2015.

[17] A. K. Kota, G. Kwon, W. Choi, J. M. Mabry, and A. Tuteja, “Hygro-responsive membranes for effective oil-water separation.,” *Nat. Commun.*, vol. 3, p. 1025, 2012.

[18] J. Zhao, A. Meyer, L. Ma, and W. Ming, “Acrylic coatings with surprising antifogging and frost-resisting properties,” *Chem. Commun.*, vol. 49, no. 100, p. 11764, 2013.

[19] H. Lee, M. L. Alcaraz, M. F. Rubner, and R. E. Cohen, “Zwitter-Wettability and Antifogging Capabilities,” *ACS Nano*, vol. 7, no. 3, pp. 2172–2185, 2013.

[20] Y. Wang, Q. Dong, Y. Wang, H. Wang, G. Li, and R. Bai, “Investigation on RAFT polymerization of a y-shaped amphiphilic fluorinated monomer and anti-fog and oil-repellent properties of the polymers,” *Macromol. Rapid Commun.*, vol. 31, no. 20, pp. 1816–1821, 2010.

[21] B. Leng, Z. Shao, G. De With, and W. Ming, “Superoleophobic cotton textiles,” *Langmuir*, vol. 25, no. 4, pp. 2456–2460, 2009.

[22] M. Kobayashi *et al.*, “Wettability and antifouling behavior on the surfaces of superhydrophilic polymer brushes,” *Langmuir*, vol. 28, no. 18, pp. 7212–7222, 2012.

[23] J. A. Howarter, K. L. Genson, and J. P. Youngblood, “Wetting behavior of oleophobic polymer coatings synthesized from fluorosurfactant-macromers,” *ACS Appl. Mater. Interfaces*, vol. 3, no. 6, pp. 2022–2030, 2011.

[24] J. A. Howarter and J. P. Youngblood, “Self-cleaning and anti-fog surfaces via stimuli-responsive polymer brushes,” *Adv. Mater.*, vol. 19, no. 22, pp. 3838–3843, 2007.

[25] A. K. Kota, G. Kwon, and A. Tuteja, “The design and applications of superomniphobic surfaces,” *NPG Asia Mater.*, vol. 6, no. 7, p. e109, 2014.

[26] W. Choi, A. Tuteja, J. M. Mabry, R. E. Cohen, and G. H. McKinley, “A modified Cassie-Baxter relationship to explain contact angle hysteresis and anisotropy on non-wetting textured surfaces,” *J. Colloid Interface Sci.*, vol. 339, no. 1, pp. 208–216, 2009.

[27] A. Tuteja, W. Choi, J. M. Mabry, G. H. McKinley, and R. E. Cohen, “Robust omniphobic surfaces,” *Proc. Natl. Acad. Sci.*, vol. 105, no. 47, pp. 18200–18205, 2008.

[28] A. Tuteja, W. Choi, G. H. McKinley, R. E. Cohen, and M. F. Rubner, “Design Parameters for Superhydrophobicity and Superoleophobicity,” *MRS Bull.*, vol. 33, no. 8, pp. 752–758, 2008.

[29] P. S. Brown, O. D. L. a Atkinson, and J. P. S. Badyal, “Ultrafast Oleophobic − Hydrophilic Switching Surfaces for Antifogging , Self-Cleaning , and Oil − Water Separation,” *Appl. Mater. Interfaces*, 2014.

[30] A. K. Kota, W. Choi, and A. Tuteja, “Superomniphobic surfaces: Design and durability,” *MRS Bull.*, vol. 38, no. 5, pp. 383–390, 2013.

[31] B. D. Cassie and S. Baxter, “ wettability of porous surfaces,” *Trans. Faraday Soc.*, Vol. 40, no. 5, pp. 546–551, 1944.

[32] Divya Panchanathan, “Photoinduced Wetting Kinetics of Water on Immersed Nanoporous Titania Surfaces with Application to Oil-Water Separation,” 2015.

[33] V. K. Gondal MA, Sadullah MS, Dastageer MA, McKinley GH, Panchanathan D, “Study of factors governing oil-water separation process using TiO_2 films prepared by spray deposition of nanoparticle dispersions,” *ACS Appl Mater Interfaces*, vol. 6, pp. 13422–13429, 2014.

[34] L. Zhang, Y. Zhong, D. Cha, and P. Wang, “A self-cleaning underwater superoleophobic mesh for oil-water separation,” *Sci. Rep.*, vol. 3, pp. 1–5, 2013.

[35] J. Yang, Z. Zhang, X. Xu, X. Zhu, X. Men, and X. Zhou, “Superhydrophilic–superoleophobic coatings,” *J. Mater. Chem.*, vol. 22, no. c, p. 2834, 2012.

[36] P. S. Brown, O. D. L. a Atkinson, and J. P. S. Badyal, “Ultrafast oleophobic-hydrophilic switching surfaces for antifogging, self-cleaning, and oil-water separation,” *ACS Appl. Mater. Interfaces*, vol. 6, no. 10, pp. 7504–7511, 2014.

[37] A. Mills and S. Le Hunte, “An overview of semiconductor photocatalysis,” *J. Photochem. Photobiol. A Chem.*, vol. 108, no. 1, pp. 1–35, 1997.

[38] D. F. Ollis, E. Pelizzetti, and N. Serpone, “Photocatalyzed destruction of water contaminants,” *Environ. Sci. Technol.*, vol. 25, no. 9, pp. 1522–1529, 1991.

[39] J. Herrmann, “Heterogeneous photocatalysis: fundamentals and applications to the removal of various types of aqueous pollutants,” *Catal. Today*, vol. 53, no. 1, pp. 115–129, 1999.

[40] M. R. Hoffmann, S. T. Martin, W. Choi, and D. W. Bahnemann, “Environmental Applications of Semiconductor Photocatalysis,” *Chem. Rev.*, vol. 95, no. 1, pp. 69–96, 1995.

[41] R. Asahi, “Visible-Light Photocatalysis in Nitrogen-Doped Titanium Oxides,” *Science (80-.).*, vol. 293, no. 5528, pp. 269–271, 2001.

[42] C. S. Turchi and D. F. Ollis, “Photocatalytic Degradation of Organic-Water

Contaminants - Mechanisms Involving Hydroxyl Radical Attack.," *J. Catal.*, vol. 122, p. 178, 1990.

[43] M. N. Chong, B. Jin, C. W. K. Chow, and C. Saint, "Recent developments in photocatalytic water treatment technology: A review," *Water Res.*, vol. 44, no. 10, pp. 2997–3027, 2010.

[44] A. Fujishima, X. Zhang, and D. A. Tryk, "TiO2 photocatalysis and related surface phenomena," *Surf. Sci. Rep.*, vol. 63, no. 12, pp. 515–582, 2008.

[45] J. Schneider *et al.*, "Understanding TiO $_2$ Photocatalysis: Mechanisms and Materials," *Chem. Rev.*, vol. 114, no. 19, pp. 9919–9986, 2014.

[46] A. T. Kuvarega and B. B. Mamba, "TiO $_2$ -based Photocatalysis: Toward Visible Light-Responsive Photocatalysts Through Doping and Fabrication of Carbon-based Nanocomposites," *Crit. Rev. Solid State Mater. Sci.*, vol. 0, no. 0, pp. 1–52, 2016.

[47] W. L. Ong, K. W. Yew, C. F. Tan, T. K. Tan Adrian, M. Hong, and G. W. Ho, "Highly flexible solution processable heterostructured zinc oxide nanowires mesh for environmental clean-up applications," *RSC Adv.*, vol. 4, pp. 27481–27487, 2014.

[48] N. Liu *et al.*, "In situ dual-functional water purification with simultaneous oil removal and visible light catalysis," *Nanoscale*, 2016.

[49] Y. Li, L. Xu, T. Chen, X. Liu, Z. Xu, and H. Zhang, "Carbon nanoparticles from corn stalk soot and its novel application as stationary phase of hydrophilic interaction chromatography and per aqueous liquid chromatography," *Anal. Chim. Acta*, vol. 726, pp. 102–108, 2012.

[50] Q. Wang and S. R. Zhang, "Size separation of carbon nanoparticles from diesel soot for Mn(II) sensing," *J. Lumin.*, vol. 146, pp. 37–41, 2014.

[51] B. N. Sahoo and K. Balasubramanian, "Facile synthesis of nano cauliflower and nano broccoli like hierarchical superhydrophobic composite coating using PVDF/carbon soot particles via gelation technique," *J. Colloid Interface Sci.*, vol. 436, pp. 111–121, 2014.

[52] S. M. Dizaj, A. Mennati, S. Jafari, K. Khezri, and K. Adibkia, "Antimicrobial activity of carbon-based nanoparticles," *Adv. Pharm. Bull.*, vol. 5, no. 1, pp. 19–23, 2015.

[53] P. A. Hu, J. Zhang, L. Li, Z. Wang, W. O'Neill, and P. Estrela, "Carbon nanostructure-based field-effect transistors for label-free chemical/biological sensors," *Sensors*, vol. 10, no. 5, pp. 5133–5159, 2010.

[54] G. Che, B. B. Lakshmi, E. R. Fisher, and C. R. Martin, "Carbon nanotube membranes for electrochemical energy storage and production," *Nature*, vol. 393, no. May, pp. 346–349, 1998.

[55] A. C. Dillon, K. M. Jones, T. A. Bekkedahl, C. H. Kiang, D. S. Bethune, and M. J.

Heben, “Storage of hydrogen in single-walled carbon nanotubes,” *Nature*, vol. 386, no. 6623. pp. 377–379, 1997.

[56] L. Han, D. Ghosh, W. Chen, S. Pradhan, X. Chang, and S. Chen, “Nanosized carbon particles from natural gas soot,” *Chem. Mater.*, vol. 21, no. 13, pp. 2803–2809, 2009.

[57] P. Z. Z. Ngu, S. P. P. Chia, J. F. Y. Fong, and S. M. Ng, “Synthesis of carbon nanoparticles from waste rice husk used for the optical sensing of metal ions,” *Xinxing Tan Cailiao/New Carbon Mater.*, vol. 31, no. 2, pp. 135–143, 2016.

[58] A. Khanam, S. K. Tripathi, D. Roy, and M. Nasim, “A facile and novel synthetic method for the preparation of hydroxyl capped fluorescent carbon nanoparticles,” *Colloids Surfaces B Biointerfaces*, vol. 102, pp. 63–69, 2013.

[59] H. Yan *et al.*, “Development of multicolor carbon nanoparticles for cell imaging,” *Talanta*, vol. 108, pp. 59–65, 2013.

[60] Y. Y. Zhang, M. Wu, Y. Q. Wang, X. W. He, W. Y. Li, and X. Z. Feng, “A new hydrothermal refluxing route to strong fluorescent carbon dots and its application as fluorescent imaging agent,” *Talanta*, vol. 117, pp. 196–202, 2013.

[61] B. Zhang, D. Wang, B. Yu, F. Zhou, and W. Liu, “Candle soot as a supercapacitor electrode material,” *RSC Adv.*, vol. 4, no. 6, pp. 2586–2589, 2014.

[62] J. Sarkar and S. Bhattacharyya, “Operating characteristics of transcritical CO2 heat pump for simultaneous water cooling and heating,” *Arch. Thermodyn.*, vol. 33, no. 4, pp. 23–40, 2012.

[63] P. Kumar and H. B. Bohidar, “Physical and fluorescent characteristics of non-functionalized carbon nanoparticles from candle soot,” *J. Nanoparticle Res.*, vol. 14, no. 7, 2012.

[64] A. Nieto-Márquez, R. Romero, A. Romero, and J. L. Valverde, “Carbon nanospheres: synthesis, physicochemical properties and applications,” *J. Mater. Chem.*, vol. 21, no. 6, pp. 1664–1672, 2011.

[65] N. D. Shooto and E. D. Dikio, “Synthesis and characterization of diesel, kerosene and candle wax soot’s,” *Int. J. Electrochem. Sci.*, vol. 7, no. 5, pp. 4335–4344, 2012.

[66] L. Zhi and K. Müllen, “A bottom-up approach from molecular nanographenes to unconventional carbon materials,” *J. Mater. Chem.*, vol. 18, no. 13, p. 1472, 2008.

[67] K. Seo, M. Kim, and D. H. Kim, “Candle-based process for creating a stable superhydrophobic surface,” *Carbon N. Y.*, vol. 68, pp. 583–596, 2014.

[68] B. N. Sahoo and B. Kandasubramanian, “An experimental design for the investigation of water repellent property of candle soot particles,” *Mater. Chem. Phys.*, vol. 148, no. 1–2, pp. 134–142, 2014.

[69] P. Parent *et al.*, “Nanoscale characterization of aircraft soot: A high-resolution

transmission electron microscopy, Raman spectroscopy, X-ray photoelectron and near-edge X-ray absorption spectroscopy study," *Carbon N. Y.*, vol. 101, no. January, pp. 86–100, 2016.

[70] P. R. Buseck, K. Adachi, A. Gelencsér, É. Tompa, and M. Pósfai, "Ns-Soot: A material-based term for strongly light-absorbing carbonaceous particles," *Aerosol Sci. Technol.*, vol. 48, no. 7, pp. 777–788, 2014.

[71] A. Ermolieff *et al.*, "XPS, Raman spectroscopy, X-ray diffraction, specular X-ray reflectivity, transmission electron microscopy and elastic recoil detection analysis of emissive carbon film characterization," *Surf. Interface Anal.*, vol. 31, no. 3, pp. 185–190, 2001.

[72] X. Zhang, T. Geng, Y. Guo, Z. Zhang, and P. Zhang, "Facile fabrication of stable superhydrophobic SiO2/polystyrene coating and separation of liquids with different surface tension," *Chem. Eng. J.*, vol. 231, pp. 414–419, 2013.

[73] S. Syed, M. I. Alhazzaa, and M. Asif, "Treatment of oily water using hydrophobic nano-silica," *Chem. Eng. J.*, vol. 167, no. 1, pp. 99–103, 2011.

[74] R. Gao *et al.*, "Fabrication of fibrous szaibelyite with hierarchical structure superhydrophobic coating on AZ31 magnesium alloy for corrosion protection," *Chem. Eng. J.*, vol. 241, pp. 352–359, 2014.

[75] T. Ishizaki, J. Hieda, N. Saito, N. Saito, and O. Takai, "Corrosion resistance and chemical stability of super-hydrophobic film deposited on magnesium alloy AZ31 by microwave plasma-enhanced chemical vapor deposition," *Electrochim. Acta*, vol. 55, no. 23, pp. 7094–7101, 2010.

[76] M. Toma, G. Loget, and R. M. Corn, "Flexible teflon nanocone array surfaces with tunable superhydrophobicity for self-cleaning and aqueous droplet patterning," *ACS Appl. Mater. Interfaces*, vol. 6, no. 14, pp. 11110–11117, 2014.

[77] R. Mohammadi, J. Wassink, and A. Amirfazli, "Effect of surfactants on wetting of super-hydrophobic surfaces," *Langmuir*, vol. 20, no. 22, pp. 9657–9662, 2004.

[78] M. Miwa, A. Nakajima, A. Fujishima, K. Hashimoto, and T. Watanabe, "Effects of the surface roughness on sliding angles of water droplets on superhydrophobic surfaces," *Langmuir*, vol. 16, no. 13, pp. 5754–5760, 2000.

[79] L. Yin *et al.*, "Fabrication of biomimetic superhydrophobic steel surface under an oxygen rich environment," *Appl. Surf. Sci.*, vol. 380, pp. 40–46, 2016.

[80] M. Ma, Y. Mao, M. Gupta, K. K. Gleason, and G. C. Rutledge, "Superhydrophobic fabrics produced by electrospinning and chemical vapor deposition," *Macromolecules*, vol. 38, no. 23, pp. 9742–9748, 2005.

[81] P. Bizi-Bandoki, S. Benayoun, S. Valette, B. Beaugiraud, and E. Audouard, "Modifications of roughness and wettability properties of metals induced by femtosecond laser treatment," *Appl. Surf. Sci.*, vol. 257, no. 12, pp. 5213–5218,

2011.

[82] J. Bekesi *et al.*, “Fast fabrication of super-hydrophobic surfaces on polypropylene by replication of short-pulse laser structured molds,” *Appl. Phys. A Mater. Sci. Process.*, vol. 99, no. 4, pp. 691–695, 2010.

[83] A. Nakajima, A. Fujishima, K. Hashimoto, and T. Watanabe, “Preparation of transparent superhydrophobic boehmite and silica films by sublimation of aluminum acetylacetonate,” *Adv. Mater.*, vol. 11, no. 16, pp. 1365–1368, 1999.

[84] K. Seo, M. Kim, and D. H. Kim, “Candle-based process for creating a stable superhydrophobic surface,” *Carbon N. Y.*, vol. 68, pp. 583–596, 2014.

[85] X. Deng, L. Mammen, H.-J. Butt, and D. Vollmer, “Candle Soot as a Template for a Transparent Robust Superamphiphobic Coating,” *Science (80-.).*, vol. 335, no. 6064, pp. 67–70, 2012.

[86] K. D. Esmeryan, A. H. Bressler, C. E. Castano, C. P. Fergusson, and R. Mohammadi, “Rational strategy for the atmospheric icing prevention based on chemically functionalized carbon soot coatings,” *Appl. Surf. Sci.*, vol. 390, pp. 452–460, 2016.

[87] K. D. Esmeryan, C. E. Castano, A. H. Bressler, M. Abolghasemibizaki, and R. Mohammadi, “Rapid synthesis of inherently robust and stable superhydrophobic carbon soot coatings,” *Appl. Surf. Sci.*, vol. 369, pp. 341–347, 2016.

[88] L. Shen, W. Wang, H. Ding, and Q. Guo, “Flame soot stably deposited on silicone coatings possess superhydrophobic surface,” *Appl. Surf. Sci.*, vol. 284, pp. 651–656, 2013.

[89] I. S. Bayer, A. J. Davis, E. Loth, and A. Steele, “Water jet resistant superhydrophobic carbonaceous films by flame synthesis and tribocharging,” *Mater. Today Commun.*, vol. 3, pp. 57–68, 2015.

[90] I. S. Bayer, A. J. Davis, and A. Biswas, “Robust superhydrophobic surfaces from small diffusion flame treatment of hydrophobic polymers,” *RSC Adv.*, vol. 4, no. 1, pp. 264–268, 2014.

[91] C. Gao *et al.*, “Integrated oil separation and water purification by a double-layer TiO2-based mesh,” *Energy Environ. Sci.*, vol. 6, no. 4, p. 1147, 2013.

[92] R. Suresh *et al.*, “Synthesis of Co 2+ -doped Fe 2 O 3 photocatalyst for degradation of pararosaniline dye,” *Solid State Sci.*, vol. 68, pp. 39–46, 2017.

[93] A. M. Mansour, “Photocatalytic degradation of methylene blue with hematite nanoparticles synthesized by thermal decomposition of fluoroquinolones oxalato–iron(<scp>iii</scp>) complexes,” *RSC Adv.*, vol. 5, no. 76, pp. 62052–62061, 2015.

[94] A. Kleiman-shwarsctein, Y. Hu, A. J. Forman, G. D. Stucky, and E. W. Mcfarland,

"Electrodeposition of r -Fe 2 O 3 Doped with Mo or Cr as Photoanodes for Photocatalytic Water Splitting," no. 1, pp. 15900–15907, 2008.

[95] C. Baumanis, J. Z. Bloh, R. Dillert, and D. W. Bahnemann, "Hematite Photocatalysis : Dechlorination of 2 , 6-Dichloroindophenol and Oxidation of Water," *October*, pp. 25442–25450, 2011.

[96] X. Zhang, H. Li, S. Wang, F. R. F. Fan, and A. J. Bard, "Improvement of hematite as photocatalyst by doping with tantalum," *J. Phys. Chem. C*, vol. 118, no. 30, pp. 16842–16850, 2014.

[97] K. Kamada and N. Soh, "Enhanced visible-light-induced photocatalytic activity of α-Fe2O3 adsorbing redox enzymes," *J. Asian Ceram. Soc.*, vol. 3, no. 1, pp. 18–21, 2015.

[98] A. Ibhadon and P. Fitzpatrick, "Heterogeneous Photocatalysis: Recent Advances and Applications," *Catalysts*, vol. 3, no. 1, pp. 189–218, 2013.

[99] Y. Wei, S. Han, D. A. Walker, S. C. Warren, and B. A. Grzybowski, "Enhanced photocatalytic activity of hybrid Fe2O3–Pd nanoparticulate catalysts," *Chem. Sci.*, vol. 3, no. 4, p. 1090, 2012.

[100] P. S. Brown and B. Bhushan, "Mechanically durable, superoleophobic coatings prepared by layer-by-layer technique for anti-smudge and oil-water separation," *Sci. Rep.*, vol. 5, p. 8701, 2015.

[101] A. Houas, H. Lachheb, M. Ksibi, E. Elaloui, C. Guillard, and J. Herrmann, "Photocatalytic degradation pathway of methylene blue in water," *Appl. Catal. B Environ.*, vol. 31, no. 2, pp. 145–157, 2001.

[102] A. L. Linsebigler, G. Lu, and J. T. Yates, "Photocatalysis on TiO2 Surfaces: Principles, Mechanisms, and Selected Results," *Chem. Rev.*, vol. 95, no. 3, pp. 735–758, 1995.

[103] D. A. Fujishima, Akira, Rao, Tata N., Tryk, "Titanium Dioxide Photocatalysis," *J. Photochem. Photobiol. C Photochem. Rev.*, vol. 1, no. March, pp. 1–21, 2000.

[104] K. Sunada, T. Watanabe, and K. Hashimoto, "Studies on photokilling of bacteria on TiO2 thin film," *J. Photochem. Photobiol. A Chem.*, vol. 156, no. 1–3, pp. 227–233, 2003.

[105] A. V. Emeline, V. Ryabchuk, and N. Serpone, "Factors affecting the efficiency of a photocatalyzed process in aqueous metal-oxide dispersions," *J. Photochem. Photobiol. A Chem.*, vol. 133, no. 1–2, pp. 89–97, 2000.

[106] M. D. Hernández-Alonso, F. Fresno, S. Suárez, and J. M. Coronado, "Development of alternative photocatalysts to TiO2: Challenges and opportunities," *Energy Environ. Sci.*, vol. 2, no. 12, p. 1231, 2009.

[107] K. Hashimoto, H. Irie, and A. Fujishima, "TiO 2 Photocatalysis: A Historical

Overview and Future Prospects," *Jpn. J. Appl. Phys.*, vol. 44, no. 12, pp. 8269–8285, 2005.

[108] S. M. Gupta and M. Tripathi, "A review of TiO2 nanoparticles," *Chinese Sci. Bull.*, vol. 56, no. 16, pp. 1639–1657, 2011.

[109] X. Chen and S. S. Mao, "Titanium dioxide nanomaterials: Synthesis, properties, modifications and applications," *Chem. Rev.*, vol. 107, no. 7, pp. 2891–2959, 2007.

[110] N. C. Raut, T. Mathews, P. K. Ajikumar, R. P. George, S. Dash, and A. K. Tyagi, "Sunlight active antibacterial nanostructured N-doped TiO2 thin films synthesized by an ultrasonic spray pyrolysis technique," *RSC Adv.*, vol. 2, no. 28, p. 10639, 2012.

[111] M. Shannon, P. W. Bohn, M. Elimelech, J. G. Georgiadis, B. J. Mariñas, and A. M. Mayes, "Science and technology for water purification in the coming decades," *Nature*, vol. 452, no. March, pp. 301–310, 2008.

[112] N. Shi *et al.*, "Biogenic N-I-codoped TiO 2 photocatalyst derived from kelp for efficient dye degradation," *Energy Environ. Sci.*, vol. 4, no. 1, pp. 172–180, 2011.

[113] S. Malato, P. Fernández-Ibáñez, M. I. Maldonado, J. Blanco, and W. Gernjak, "Decontamination and disinfection of water by solar photocatalysis: Recent overview and trends," *Catal. Today*, vol. 147, no. 1, pp. 1–59, 2009.

[114] S. Rehman, R. Ullah, A. M. Butt, and N. D. Gohar, "Strategies of making TiO2 and ZnO visible light active," *J. Hazard. Mater.*, vol. 170, no. 2–3, pp. 560–569, 2009.

[115] A. Kubacka, M. Fernández-García, and G. Colón, "Advanced nanoarchitectures for solar photocatalytic applications," *Chem. Rev.*, vol. 112, no. 3, pp. 1555–1614, 2012.

[116] S. A. Ansari, M. M. Khan, M. O. Ansari and M. H. Cho, "Nitrogen-doped titanium dioxide (N-doped TiO2) for visible light photocatalysis," *New J. Chem.*, vol. 40, no. 4, pp. 3000–3009, 2016

[117] W. J. Ong, L. L. Tan, Y. H. Ng, S. T. Yong, and S. P. Chai, "Graphitic Carbon Nitride (g-C3N4)-Based Photocatalysts for Artificial Photosynthesis and Environmental Remediation: Are We a Step Closer to Achieving Sustainability?," *Chem. Rev.*, vol. 116, no. 12, pp. 7159–7329, 2016.

[118] C. K. Prier, D. A. Rankic, and D. W. C. MacMillan, "Visible light photoredox catalysis with transition metal complexes: Applications in organic synthesis," *Chem. Rev.*, vol. 113, no. 7, pp. 5322–5363, 2013.

[119] R. Asahi, T. Morikawa, H. Irie, and T. Ohwaki, "Nitrogen-Doped Titanium Dioxide as Visible-Light-Sensitive Photocatalyst : Designs , Developments , and Prospects," 2014.

[120] S. T. Ren, G. H. Fan, M. L. Liang, Q. Wang, and G. L. Zhao, "Electrodeposition of hierarchical ZnO/Cu2O nanorod films for highly efficient visible-light-driven photocatalytic applications," *J. Appl. Phys.*, vol. 115, no. 6, 2014.

[121] D. F. Swinehart, “The Beer-Lambert Law,” *J. Chem. Educ.*, vol. 39, no. 7, p. 333, 1962.

[122] H. Sawada, Y. Ikematsu, T. Kawase, and Y. Hayakawa, “Synthesis and Surface Properties of Novel Fluoroalkylated Flip-Flop-Type Silane Coupling Agents,” *Langmuir*, vol. 12, no. 15, pp. 3529–3530, 1996.

[123] S. Cassie, A.B.D, Baxter, “Wettability of porous surfaces,” *Trans. Faraday Soc.*, vol. 40, pp. 546–551, 1944.

[124] A. Kota, Arun K., Choi, Wonjae, Tuteja, “Superomniphobic surfaces: Design and durability,” *MRS Bull.*, vol. 38, no. 5, pp. 383–390, 2013.

[125] T. Ochiai, S. Tago, M. Hayashi, H. Tawarayama, T. Hosoya, and A. Fujishima, “TiO2-Impregnated Porous Silica Tube and Its Application for Compact Air- and Water-Purification Units,” *Catalysts*, vol. 5, no. 3, pp. 1498–1506, 2015.

[126] A. Mills, J. Wang, and D. F. Ollis, “Dependence of the kinetics of liquid-phase photocatalyzed reactions on oxygen concentration and light intensity,” *J. Catal.*, vol. 243, no. 1, pp. 1–6, 2006.

[127] D. Panchanathan, G. Kwon, T. F. Qahtan, M. A. Gondal, K. K. Varanasi, and G. H. Mckinley, “Kinetics of Photoinduced Wettability Switching on Nanoporous Titania Surfaces under Oil,” *Adv. Mater. Interfaces*, 2017.

[128] H. S. Fogler, “Distributions of residence times for chemical reactors,” *Elem. Chem. React. Eng.*, pp. 867–944, 2006.

[129] J. Li, L. Yan, W. Hu, D. Li, F. Zha, and Z. Lei, “Facile fabrication of underwater superoleophobic TiO2 coated mesh for highly efficient oil/water separation,” *Colloids Surfaces A Physicochem. Eng. Asp.*, vol. 489, pp. 441–446, 2016.

[130] L. Li, Z. Liu, Q. Zhang, C. Meng, T. Zhang, and J. Zhai, “Underwater superoleophobic porous membrane based on hierarchical TiO2 nanotubes: multifunctional integration of oil–water separation, flow-through photocatalysis and self-cleaning,” *J. Mater. Chem. A*, vol. 3, pp. 1279–1286, 2015.

[131] Y. Cao, N. Liu, W. Zhang, L. Feng, and Y. Wei, “One-Step Coating toward Multifunctional Applications: Oil/Water Mixtures and Emulsions Separation and Contaminants Adsorption,” *ACS Appl. Mater. Interfaces*, vol. 8, no. 5, pp. 3333–3339, 2016.

[132] Spoerl.de, “Twill Dutch Weave Image.” .

Vitae

Name : TALAL FARHAN AHMED QAHTAN

Nationality : YEMENI

Date of Birth : 12/12/1981

Email : tfqahtan@gmail.com

Address : Taiz, Yemen

Academic Background : B.Sc. in Physics from Taiz University in 2007 and M.Sc in Physics from King Fahd University of Petroleum and Minerals in 2013

Inventions and Patents

1. **T. F. Qahtan**, M. A. Gondal, M.A. Dastageer ، A Facile Method to Synthesize Stable Carbon Nanoparticles Dispersions and its Application to Fabricate Thermally and Mechanically Stable Superhydrophobic Surfaces using Inexpensive Candle Soot (as Raw Material) submitted on 13th March, 2016.
2. **T. F. Qahtan**, L. D. Banchik, M.A. Gondal, G.Kwon, D.Panchanathan, U. Baig, G.McKinley, Development of Advanced Multifunctional Robust Membrane for Efficient Oil-water Separation and Simultaneous Removal of Organic Pollutants, submitted on 3rd March, 2016.
3. M. A. Gondal, M.A. Dastageer, **T. F. Qahtan**, U. Baig, G.McKinley, Fabrication of Textured Membrane using Unique Spray Coater for Remediation of Oily Wastewater, submitted on 18th October, 2017.
4. **T. F. Qahtan**, M. A. Gondal, M.A. Dastageer ، One-step Scalable Fabrication of Mechanically Robust Visible-light Responsive Oxide-Modified Metallic Multifunctional Membranes submitted on 15th December, 2017.

Publications

1. **Talal F. Qahtan**, Mohammed A. Gondal, Z. H. Yamani, Mohammed A. Dastageer, Using the magnetic field to prove the theory of the photocatalysis, *Physical Review Letters* in progress (2017).
2. **Talal F. Qahtan**, Mohammed A. Gondal, Recent Advances in Multifunctional Textured Membrane for Oily Wastewater Remediation, *Advanced Materials* in progress (2017).
3. **T. F. Qahtan**, M. A. Gondal, M.A. Dastageer ، One-step Scalable Fabrication of Mechanically Robust Visible-light Responsive Oxide-Modified Metallic Multifunctional Membranes, *Nanoscale* in progress (2017).
4. **T. F. Qahtan**, M. A. Gondal, M.A. Dastageer ، G. Kwon and G. H. McKinley, Photodeposition of Pd NPs on WO_3 coated membranes for sulfide reducing bacteria deactivation under visible light irradiation, *Energy and Environmental Science* in progress (2017).
5. **Talal F. Qahtan**, Mohammed A. Gondal, Ibrahim O. Alade, Mohammed A. Dastageer, Fabrication of Water Jet Resistant and Thermally Stable Superhydrophobic Surfaces by Spray Coating of Candle Soot Dispersion, *Nature's Scientific Reports* 7 (2017).
6. D. Panchanathan, G. Kwon**, T. F. Qahtan**, M. A. Gondal, Kripa K. Varanasi, G. H. McKinley, Kinetics of Photoinduced Wettability Switching on Nanoporous Titania Surfaces under Oil. *Advanced Materials Interfaces* 4 (2017).
7. Idris K. Popoola, Mohammed A. Gondal and **Talal F. Qahtan**, Recent progress in flexible perovskite solar cells: materials, mechanical tolerance and stability, *Renewable & Sustainable Energy Reviews,* in press (2017).
8. **Talal F. Qahtan**, Leonardo D. Banchik, Mohammed A. Gondal, Gibum Kwonb, Divya Panchanathan, Mohammed A. Dastageer, Kripa Varanasi and Gareth McKinley, A Janus membrane for a single operation of oil-water separation and in-situ decontamination of water, *Energy and Environmental Science,* submitted (2017).
9. Idris K. Popoola, Mohammed A. Gondal, Jwaher Al-Ghamdi and **Talal F. Qahtan**, Photofabrication of Highly Transparent Platinum counter electrodes for bifacial Dye sensitized solar cells, *Nano Energy,* submitted (2017).
10. M.A.Gondal, **Talal F. Qahtan**, M.A. Dastageer, Z. H. Yamani and D. H. Anjum, A Rapid and Cost-Effective Laser Based Synthesis of High Purity Cadmium Selinide Quantum Dots, *Journal of Nanoscience and Nanotechnology* 16 (2016).
11. M. A. Gondal, T. A. Fasasi, A. Mekki, T. A. Saleh, A. M. Ilyas, **T. F. Qahtan** and X. Chang, Phase Transformation and Structural Characterization Studies of Aluminum Oxide (Al_2O_3) Nanoparticles Synthesized Using an Elegant Pulsed Laser Ablation in Liquids Technique, *Nanoscience and Nanotechnology Letters* 8 (2016).
12. M. A. Gondal, A.M. Ilyas, T. A. Fasasi , M.A. Dastageer, Z. S. Seddigi, **T.F. Qahtan**, M. Faiz, G. D. Khattak, Synthesis of Green TiO_2/ZnO/CdS Hybrid Nano-catalyst for Efficient Light Harvesting using an Elegant Pulsed Laser Ablation in Liquids Method, *Applied Surface Science* 357 (2015).

13. Amani M. Alansi, Waed Z Alkayali, Maha Al-Qunaibit, **Talal F. Qahtan** and Tawfik A. Saleh, Synthesis of exfoliated polystyrene/anionic clay MgAl-layered double hydroxide: structural and thermal properties, *RSC Advances* 5 (2015).
14. M. A. Gondal, Y. W. Maganda, M.A. Dastageer, F. F. Al Adel, A. A. Naqvi , **Talal F. Qahtan**, Optimization of Plasma Parameters and Detection of Fluoride in Toothpaste using Laser Induced Breakdown Spectroscopy, *Optics & Laser Technology* 57 (2014).
15. M. A. Gondal, Y. W. Maganda, M.A. Dastageer, F. F. Al Adel, A. A. Naqvi , **Talal F. Qahtan** Detection of Carcinogenic Chromium in Synthetic Hair Dyes using Laser Induced Breakdown Spectroscopy, *Applied Optics* 53 (2014).
16. M. A. Gondal, **Talal F. Qahtan** , M.A. Dastageer,M.Y.Maganda, D. H. Anjum Effects of Oxidizing Medium on the Composition, Morphology and Optical Properties of Copper Oxide Nanoparticles produced by Pulsed Laser Ablation, *Appl. Surf. Science* 286 (2013).
17. M.A. Gondal, **Talal F. Qahtan**, M. A. Dastageer and Yasin. W. Maganda, D. H. Anjum Synthesis of Cu/Cu_2o Nanoparticles by Laser Ablation in Deionized Water and Their Annealing Transformation into CuO Nanoparticles, *Journal of Nanoscience and Nanotechnology,* 13 (2013).

Conference Publications & Posters

1. **T.F. Qahtan**, M.A. Gondala, U. Baigb, M.A. Dastageer, L. Oloore, Facile Fabrication of Candle Soot Based Super-Hydrophobic Surface , *International Conference on Physics and Chemistries at Hydrophobic Interfaces*. KAUST, Thawal, Saudi Arabia (Feb 14 -17 , 2016).
2. M.A. Gondal, M.S. Sadullah, **Tala F. Qahtan**, M.A. Dastageer, Umair Baig, G. H. McKinley, Oil-Water Separation Using Nano-Structured Semiconducting Metal Oxide Coated Surfaces, *International Conference on Physics and Chemistries at Hydrophobic Interfaces*. KAUST, Thawal, Saudi Arabia (Feb 14 - 17, 2016).
3. D. Panchanathan, G. Kwon, M. A. Gondal**, T. F. Qahtan**, Kripa K. Varanasi, G. H. McKinley, In-situ self-cleaning wetting kinetics on immersed nanoporous titania surfaces under UV irradiation, *89th ACS Colloid and Surface Science Symposium*, Carnegie Mellon University, USA (June 15-17, 2015).
4. M.A. Gondal, A. M. Ilyas, T.A. Fasasi, M.A. Dastageer ,**T. F. Qahtan**, Synthesis of Ag-ZnO Core-Shell Composite Structures Using Pulsed Laser Ablation in Liquids (PLAL) for Visible Light Applications, *Interantional Conference on Atomic, Molecular and Optical Physics (AMOP),* Al-Jouf University, Saudi Arabia (March 31 – April 2, 2015).
5. M.A. Gondal, T.A. Fasasi, A. M. Ilyas, M.A. Dastageer, **T. F. Qahtan** , Synthesis and Characterization of Phase Transition of Al_2O_3 Nanoparticles Via Pulsed Laser Ablation in Liquids, *Interantional Conference on Atmoic,*

Molecular and Optical Physics (AMOP), Al-Jouf University, Saudi Arabia (March 31 – April 2, 2015).

6. M.A. Gondal, **T. F. Qahtan**, M. A. Dastageer, Synthesis of High Purity CdSe Quantum Dots using Nanosecond Pulsed Laser Ablation in Liquids,*Gordon Resaerch Conference on Noble Metal Nanoparticles Synthesis Characterization and Applications*, South Hadley, Massachusett, USA (15-20 June 2014).
7. **Talal F. Qahtan**, M.A. Gondal, M. A. Dastageer, Z. H. Yamani and D. H. Anjum, Preparation of CdSe Quantum Dots using nanosecond Laser, *3rd Saudi International Meeting on Frontiers of Physics,* Jazan, Saudi Arabia (Feb18-20, 2014).
8. M. A. Gondal, A.M. Ilyas, **T. F. Qahtan**, Synthesis of $ZnO-TiO_2$ Nano-composites using Pulsed Laser Ablation in Liquids (PLAL), *3rd Saudi International Meeting on Frontiers of Physics,* Jazan, Saudi Arabia (Feb18-20, 2014).
9. M.A.Gondal, **T. F. Qahtan**, M.A. Dastageer, T.A. Saleh and Y.W. Maganda, Synthesis and Characterization of Copper Oxides Nanoparticles Via Pulsed Laser Ablation in liquids, IEEE proceedings, *10th International Conference on High Capacity Optical Networks and Enabling Technologies*, HONET-CNS 2013, Article number 6729774, Pages 146-150.
10. M.A. Gondal, Y.W. Maganda, M.A. Dastageer, F.F Al-Adel, A.A Naqvi, **T.F Qahtan**, Development of a laser induced breakdown sensor for detection of carcinogenic chemicals in cosmetic products, IEEE proceedings, *10th International Confercne on High Capacity Optical Networks and Emerging/Enabling Technologies*, HONET-CNS 2013, Article number 6729762, Pages 84-88.
11. M.A. Gondal, **T.F. Qahtan** M.A. Dastageer, T.A. Saleh ,Generation of Copper Oxides Nanoparticles Using Pulsed Laser Ablation in Water, *The 9th International Conference and Exhibition on Chemistry in Industry*, Manama (Nov2 - 6, 2013) Bahrain.
12. Amani M. Alansi, **Talal F. Qahtan** , M. A. Gondal, Waed Z Alkayali, Maha Al-Qunaibit, Synthesis and Characterization of Layered Double Hydroxide Anionic Clays Intercalated via Sodium Dodecyl Sulfate Anion for Application of Polymer/LDH Nanocomposites, *The 9th International Conference and Exhibition on Chemistry in Industry,* Manama (Nov2 - 6, 2013) Bahrain.
13. M.A. Gondal, **T.F. Qahtan**, M.A. Dastageer, Synthesis and Characterization Of Metal Oxides (Al_2O_3, Cuo) Nanoparticles Using Pulsed Laser Ablation Technique, *The Saudi International Nanotechnologies Conference*, Riyadh , Saudi Arabia (Nov 11-13, 2012).